Atomic and electronic structure of the cleaved non-polar 6H-SiC($11\bar{2}0$) and GaN($1\bar{1}00$) surfaces

Dissertation
zur Erlangung des Doktorgrades
der Mathematisch-Naturwissenschaftlichen Fakultäten
der Georg-August-Universität zu Göttingen

vorgelegt von
Marco Bertelli
aus Modena

Göttingen, 2008

D7

Referent: Frau Prof. Dr. A. Rizzi

Korreferent: Herr Prof. Dr. F. Bechstedt

Tag der mündlichen Prüfung: 30. Januar 2009

Contents

Introduction **xi**

1 STM theory and experimental set-up **1**
- 1.1 Models for the tunneling current 2
  - 1.1.1 Bardeen approach 3
  - 1.1.2 Tersoff and Hamann approximation 5
  - 1.1.3 Hamers model 7
  - 1.1.4 Chen derivative rule 8
- 1.2 Experimental set-up 11
  - 1.2.1 The STM system 11
  - 1.2.2 Tip preparation 13
- 1.3 STM/STS methods and data analysis 14
  - 1.3.1 Single-bias constant current topographies 15
  - 1.3.2 Multi-bias constant current topographies 17
  - 1.3.3 Scanning Tunneling Spectroscopy 18
  - 1.3.4 Templates in periodic structures 26

2 Physical Properties of non-polar SiC and GaN surfaces **29**
- 2.1 Principles of surface reconstruction 29
  - 2.1.1 Atomic structure 30
  - 2.1.2 Electronic structure 32
- 2.2 Polarization of hexagonal compound semiconductors 35
- 2.3 Non-polar SiC surfaces 37
  - 2.3.1 SiC crystal growth and polytypism 38
  - 2.3.2 SiC properties and applications 41
  - 2.3.3 Atomic and electronic structure of non-polar SiC surfaces 44
- 2.4 Non-polar GaN surfaces 49
  - 2.4.1 GaN substrates grown by Hydride Vapor Phase Epitaxy 49
  - 2.4.2 GaN properties and applications 53

2.4.3 Atomic and electronic structure of non-polar GaN surfaces 57

3 Atomic and electronic structure of the cleaved 6H-SiC(11$\bar{2}$0) surface 63
3.1 Experimental details 64
3.2 STM results 69
3.3 Theoretical analysis 72
3.4 Discussion 78
3.5 Summary and outlook 80

4 Atomic and electronic structure of the cleaved GaN(1$\bar{1}$00) surface 83
4.1 Experimental details 84
4.2 STM results 91
4.3 Theoretical analysis 98
4.4 Discussion 104
4.5 Summary and outlook 108

Conclusions 111

Appendix - Computational details 113
.1 6H-SiC(11$\bar{2}$0) surface 113
.2 GaN(1$\bar{1}$00) surface 113

List of abbreviations 115

Bibliography 117

Acknowledgements 131

Curriculum vitae 133

Lebenslauf 135

"Non ho mai chiesto di occuparmi di mafia.
Ci sono entrato per caso.
E poi ci sono rimasto per un problema morale.
La gente mi moriva attorno".

"I never asked to work on mafia.
I got in by chance.
And then I stayed because of a moral issue.
People were dying around me".

Paolo Borsellino

Introduction

SiC and GaN are the most employed wide-bandgap semiconductors for high-power, high-temperature, and high-frequency applications. The polytypes 3C-, 4H-, and 6H-SiC are used to produce semiconductor devices such as blue and green *Light Emitting Diodes* (LEDs), *Schottky barrier diodes* and *Metal Oxide Semiconductor Field Effect Transistors* (MOSFETs). Furthermore they are used as substrates for AlN and GaN epitaxial growth. The development of SiC technology has been hindered for several years by the formation of macroscopic tubular voids (*micropipes*) in the bulk SiC material, but the recent introduction on the market of micropipe-free four inch *n*-type 4H-SiC substrates opens new horizons in the expansion of SiC-based devices.
The polytype 2H-GaN can be employed to cover a huge spectrum of semiconductors applications going from blue LEDs and *Laser Diodes* (LDs) to *High Electron Mobility Transistors* (HEMTs). GaN-based devices are the core of the so-called "*Blu-ray Disc*" technology that in the last five years has been massively applied for the production of high-storage-data media like *Digital Video Discs* (DVDs). Dual layer 12-cm DVDs with a storage capacity of 50 Gb are today available on the market.

We address our attention in this work to the study of the electronic properties of non-polar 6H-SiC and 2H-GaN surfaces. 6H-SiC is the preferable substrate for group III-nitride growth and 2H-GaN is the more stable allotropic modification of GaN suited for industrial applications.
Up to recent times 6H-SiC and 2H-GaN films were grown parallel to the [0001] direction (c-axis) due to enhanced crystalline quality. A relevant problem though hampers the full potential of these materials: along the polar c-axis strong internal electric fields are induced in heterostructures. As a consequence, electrons and holes tend to be separated and the radiative efficiency of their recombination probability is reduced. P. Waltereit and co-workers showed in 2000 [WBT+00] that this drawback is avoided if the semiconductor film is grown along a non-polar direction: GaN/AlGaN het-

erostructures grown on tetragonal $\gamma - \mathrm{LiAlO_2}$ along the non-polar $[1\bar{1}00]$ direction allows the fabrication of structures free of electrostatic fields, resulting in an improved quantum efficiency.
After this work many research groups in universities, public institutions and private companies focused their attention on the study of SiC and nitrides semiconductor films grown along the non-polar $[11\bar{2}0]$ and $[1\bar{1}00]$ directions. Many interesting results have been meanwhile reached. For example, it has been shown in 2000 that the problem of low bulk mobility along the c-axis in 6H-SiC MOSFETs fabricated on the conventional (0001) Si-face can be overcome employing the $(11\bar{2}0)$ surface (a-plane). Even the so called "green-gap" of nitride-based LDs could be closed in the next future: K. Okamoto and co-workers reported in june 2008 about continuous-wave operation of blue-green LDs with a lasing wavelength of 481 nm based on the non-polar GaN$(1\bar{1}00)$ surface (m-plane).
In view of these novel applications a complete understanding of the physical properties of non-polar 6H-SiC and 2H-GaN surfaces is of major importance. Until now several theoretical studies have been published on these surfaces but only few experimental investigations have been performed on them.

This work shows the results of an experimental *Cross-section Scanning Tunneling Microscopy and Spectroscopy* (X-STM/STS) study at room temperature on the cleaved non-polar 6H-SiC$(11\bar{2}0)$ and GaN$(1\bar{1}00)$ surfaces. The measurements were performed in the groups of Prof. A. Rizzi and Prof. R. G. Ulbrich at the *IV. Physikalisches Institut* of the Faculty of Physics at the Goettingen University (Germany). This experimental work was done in close collaboration with a theoretical group which carried out *ab-initio* simulations in the frame of first-principles *Density Functional Theory* (DFT). The calculations were performed by M. C. Righi *et al.* and A. Catellani at the *Dipartimento di fisica* of the Modena University and at the *Centro Nazionale delle Ricerche - Istituto dei Materiali per l'Elettronica ed il Magnetismo* (CNR-IMEM) in Parma (Italy), respectively.

In STM experiments a very sharp metallic tip is brought in close proximity (few Å) to the surface of a conductive sample and a current I in the range of some nA flows between the two electrodes if a voltage bias U of few mV is applied between tip and sample. The physical phenomenon at the base of this experiment is the so-called *tunnel effect* which is described in the frame of the quantum mechanics theory. This technique has been extensively applied in the study of semiconductor surfaces and has provided insight into their electronic properties with atomic scale resolution.

At the beginning of this project (2003), the aim was to adapt the cleavage technique developed for GaAs to GaN films grown on 6H-SiC substrates. The first step of our work consisted in optimizing the cleavage of 6H-SiC(0001) substrates in order to expose the clean 6H-SiC($11\bar{2}0$) surface and to study it by X-STM/STS measurements. Once collected the results on the non-polar SiC system, we could move to study the non-polar cleaved surface of GaN epilayers grown on SiC substrates. Only in 2005 free-standing *Hydride Vapor Phase Epitaxy* (HVPE) GaN *quasi*-substrates appeared on the market and we reacted by transferring the experience gained in X-STM/STS investigation of the cleaved non-polar 6H-SiC surfaces to the non-polar GaN ones by direct cleavage of the thick free-standing HVPE GaN(0001) samples.
Our experimental results are shown in the following chapters together with theoretical DFT calculations which have been included for the sake of comparison:

1. **Chapter 1** recalls briefly the main concepts and models of tunneling theory. Then the experimental set-up and methods that have been used in the measurements are presented together with a description of the techniques applied to analyse the data.

2. **Chapter 2** deals with the general principles ruling semiconductor surface reconstruction. Then a section is devoted to describe a peculiar property of hexagonal compound semiconductors, *i. e.* polarity and the spontaneous polarization. Finally an overview on theoretical and experimental data found in literature on non-polar SiC and GaN surfaces is given.

3. **Chapter 3** and **Chapter 4** present the experimental and theoretical results on the cleaved non-polar 6H-SiC($11\bar{2}0$) and GaN($1\bar{1}00$) surfaces, respectively. Their organization is the same: in Sec. I the experimental details of the work are introduced. In Sec. II the X-STM/STS data are displayed with particular attention to the spatial localization of empty and filled states in STM topographies, while in Sec. III the DFT calculations concerning the atomic and electronic structure of the cleaved surface are presented. Sec. IV deals with the comparison between experimental and theoretical results. Finally Sec. V gives a summary of the obtained results and an outlook on future perspectives.

Chapter 1

STM theory and experimental set-up

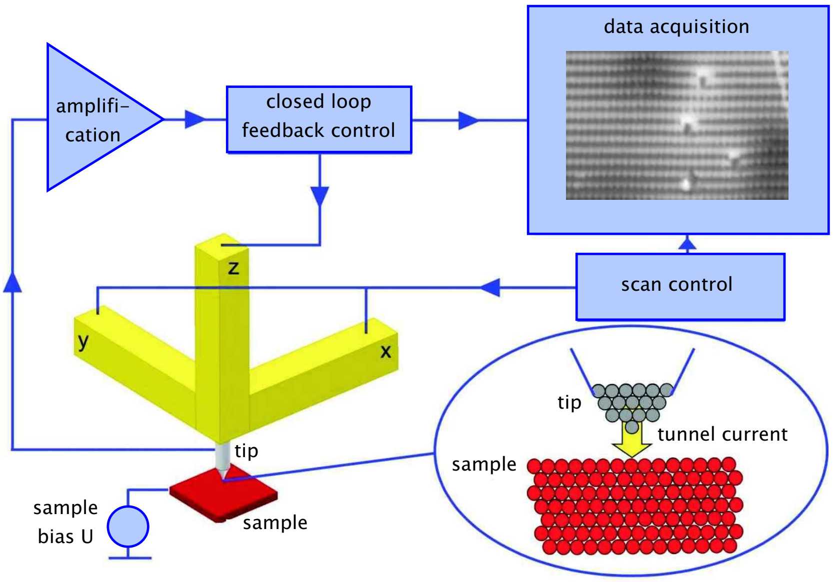

Figure 1.1: Principle of scanning tunnelling microscopy. For description see text (from [Lot07]).

After the first experiments of G. Binnig and H. Rohrer in 1979, the *Scanning Tunneling Microscopy* (STM) rapidly developed and is nowadays one of the most used techniques to characterize surfaces [BRGW82]. In STM a sharp conductive tip is brought to a distance d of few Å from a conductive sample surface whose electronic properties are the object of investigation (Fig. 1.1). If a bias U of few mV is applied between tip and sample, a tunneling current I from 10 pA to few nA flows between the two electrodes. With the help of piezoelements the tip is moved in the three space directions (x, y, z) with sub-Ångstrom precision and the tip displacement $z = z(x, y)$ on the sample surface is measured while a feedback loop keeps a reference parameter costant. In constant-current mode the height of the tip is adjusted so that the tunneling current stays constant during the scanning of the sample surface at set bias. The height signal is then acquired as topographic information and gives insight into the atomic and electronic properties of the sample surface.

This chapter is organized as follows: Sec. 1.1 introduces the models that have been developed during the last thirty years to understand and simulate the tunneling experiments. Sec. 1.2 describes the STM set-up that was used to collect the experimental data and the procedure to prepare STM tips. Finally Sec. 1.3 deals with the experimental methods and the techniques that we applied to collect and evaluate the STM data, respectively.

1.1 Models for the tunneling current

The STM metod is based on the so-called *tunnel effect*, which states that according to the laws of quantum mechanics it is possible for a particle with mass m and energy E to penetrate a potential barrier whose height and width are V_0 and d, respectively (Fig. 1.2). In a one-dimensional (1D) model the penetration of the particle into the barrier is characterized by the transmission coefficient T:

$$T = 16\frac{E}{V_0}\left(1 - \frac{E}{V_0}\right) e^{-2kd} \tag{1.1}$$

where $k = \frac{1}{\hbar}\sqrt{2m\left(V_0 - E\right)}$ denotes the inverse decay length of the wave function Ψ associated to the particle in the region of the potential barrier. Eq. 1.1 is valid for the case $kd \gg 1$. The transmission probability of the particle through the potential barrier depends exponentially on the width d of the potential barrier: if the amplitude d increases 1 Å, the tunneling transmission coefficient T diminishes around one order of magnitude.
In STM a tunneling current I flows between two polarized electrodes which are placed each other at a distance of few Å. The mathematical description of the real tunneling process of one electron through a barrier between a probing tip and a sample is much more complex that the 1D model described by Eq. 1.1. Only few theoretical STM principles will be introduced in this chapter, just the ones relevant for the evaluation of the experimental

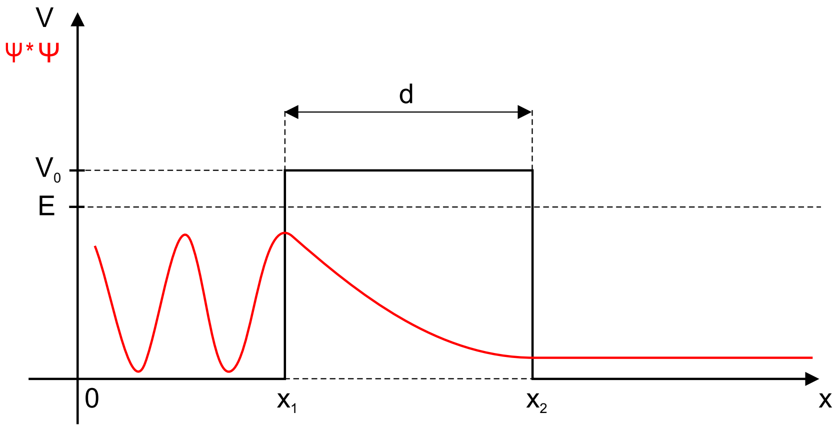

Figure 1.2: Schema of 1D tunneling of a particle of energy E through a rectangular potential barrier of height V_0 and width d in the case $E < V_0$. The probability density function $\Psi^*\Psi$ associated to the particle is displayed in red.

results. A more complete discussion of STM theory and methods can be found in references [Che93] and [Wie94].
STM is an experimental technique which shows two main advantages for the study of surfaces. On the one side it provides high vertical z resolution due to the exponential dependence of the tunneling current I on the tip-sample distance d. On the other side the tunneling current in STM flows through a region with a diameter $d \approx 5$ Å, so that spectroscopic information can be obtained on an atom-by-atom scale. Other spectroscopy techniques such as *Ultraviolet Photoemission Spectroscopy* (UPS) or *Inverse Photoemission Spectroscopy* (IPS) provide information averaged over a much larger region of surfaces and can not reach atomic resolution [Ham89].

1.1.1 Bardeen approach

In 1961 J. Bardeen developed a model in the framework of the first order pertubation theory to describe the tunneling current flowing between two metal plates separated by a thin oxide layer [Bar61]. The results can be extended to a point tunneling contact as in the case of STM where one electron is transferred from a state ψ_μ in the sample to a state χ_ν in the tip. According to Bardeen, the transmission probability between the two states is given by the transfer matrix element $M_{\mu\nu}$:

$$M_{\mu\nu} = -\frac{\hbar^2}{2m}\int_S \left(\chi_\nu^* \nabla \psi_\mu - \psi_\mu \nabla \chi_\nu^*\right) \overrightarrow{dS} \tag{1.2}$$

where the integral is calculated along any surface S lying entirely within the vacuum region separating sample and tip. If a voltage U is applied at the sample, the Fermi energy in the sample E_{FS} and in the tip E_{FT} lie at different height and a tunneling current I flows between the two electrodes:

$$I = \frac{2\pi e}{\hbar} \sum_{\mu\nu} \underbrace{\left[f\left(E_{\mu S} - E_{FS} + eU\right) - f\left(E_{\nu T} - E_{FT}\right)\right]}_{1} \underbrace{|M_{\mu\nu}|^2}_{2} \underbrace{\delta\left(E_{\mu S} - E_{\nu T}\right)}_{3} \tag{1.3}$$

where the indices S and T indicate sample and tip, while μ and ν the initial and the final state in the tunneling process, respectively. The tunnel current results from the sum of all possible tunnel events whose probabilty depends on three factors:

1. The first factor cointains the Fermi distribution function $f(E)$:

   $$f\left(E_{\mu S} - E_{FS} + eU\right) - f\left(E_{\nu T} - E_{FT}\right) = \begin{cases} 1 & \text{tunneling from the sample to the tip} \\ 0 & \text{no tunneling} \\ -1 & \text{tunneling from the tip to the sample} \end{cases}$$

   where $f(E) = (1 + exp(\frac{E}{k_B \Theta}))^{-1}$, k_B is the Boltzmann constant and Θ the temperature. The tunneling event can only take place between one filled and one empty state. When the two states are both filled or empty the tunneling process can not occur.

2. The second factor $|M_{\mu\nu}|^2$ represents the tunneling probability of one electron between the sample state ψ_μ and the tip state χ_ν.

3. The third factor ensures that during the tunneling process the energy of the transferred electron remains constant (elastic tunneling):

   $$\delta\left(E_{\mu S} - E_{\nu T}\right) = \begin{cases} 1 & \text{for } E_{\mu S} = E_{\nu T} \\ 0 & \text{for } E_{\mu S} \neq E_{\nu T} \end{cases}$$

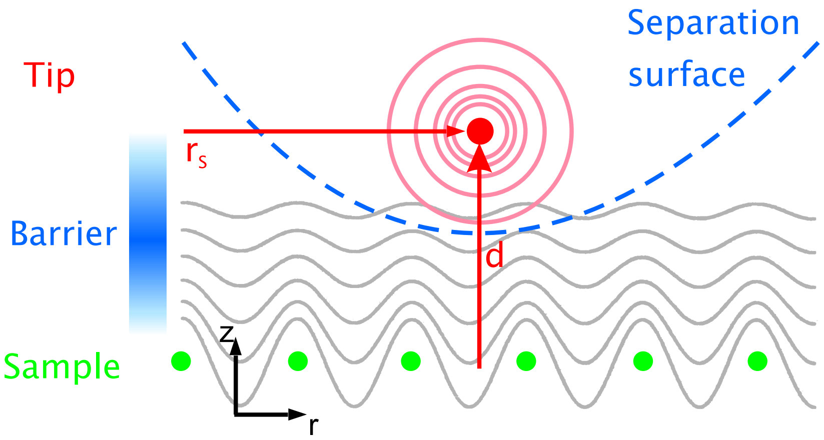

Figure 1.3: Scheme of the tunneling geometry in the Tersoff and Hamann model. In the image the sample atoms (green) and the last tip atom (red) are drawn. The grey and red lines represent contours of constant LDOS in the sample and tip, respectively. The tip is described with an s-wave state. The separation surface lies within the vacuum barrier between sample and tip (from [Lot04]).

1.1.2 Tersoff and Hamann approximation

To evaluate I according to Eq. 1.3 it is necessary to calculate the transfer matrix element $M_{\mu\nu}$ and to know the expression of the wave functions χ_ν of the tip which are generally unknown. To solve this problem, J. Tersoff and D. R. Hamann proposed in 1983 a model where the transfer matrix element $|M_{\mu\nu}|^2$ is evaluated for a s-like tip wave function χ_ν (Fig. 1.3, [TH83]). Expanding the tip s-wave function into a set of plane-waves in the case of small temperature ($\Theta \leq 273$ K) and small bias ($U \leq 10$ mV) it is possible to calculate explicitely the term $M_{\mu\nu}$:

$$I \propto eUD_T\left(E_F\right)\sum_\mu |\psi_\mu\left(\vec{r}_S\right)|^2\delta\left(E_{\mu S}-E_{FS}\right) \tag{1.4}$$

where $\vec{r}_S$ identifies the tip position and $D_T\left(E_{FT}\right)$ the tip *Density Of States* (DOS) at the Fermi energy E_{FT} which is assumed to be constant for small ranges ΔE close to E_{FT}.
According to Eq. 1.4 the tunneling current I is proportional to the *Local Density Of States* (LDOS) of the sample evaluated at the position of the tip $\vec{r}_S$ and at the Fermi energy E_{FS}:

$$I \propto LDOS\left(\vec{r}_S, E_{FS}\right) \equiv \sum_\mu |\psi_\mu\left(\vec{r}_S\right)|^2\delta\left(E_{\mu S}-E_{FS}\right) \tag{1.5}$$

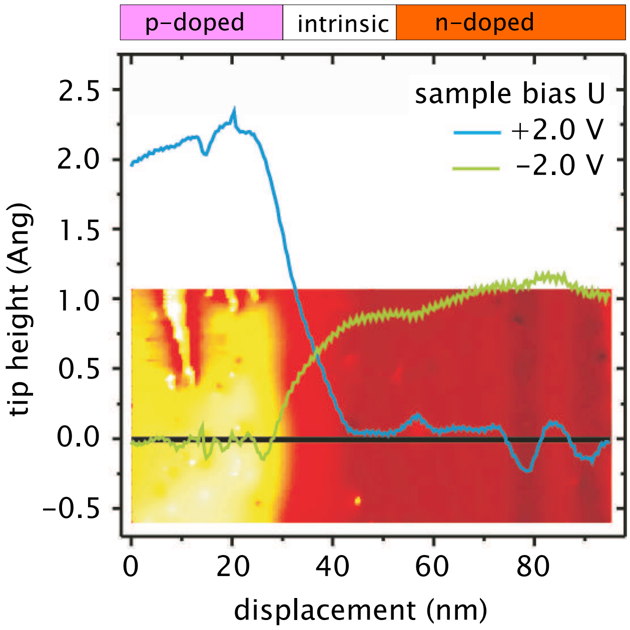

Figure 1.4: Two cross-section traces (blue and green profiles) along the same line (black) of a GaAs(110) surface running across a p-i-n interface: the blue line is recorded at positive sample bias ($U = +2.0$ V) and the green one at negative sample bias ($U = -2.0$ V). The empty states STM topography at $U = +2.0$ V is shown in the bottom half of the image (the tip height increases from red to yellow colour). The cleavage surface of this region is atomically flat. The massive height modulation of > 2 Å between blue and green line is of mere electronic origin due to the varying doping type (from [Lot07]).

In **constant current mode STM** the distance between sample and tip is changed by a feedback loop which compensates the lateral modulations of the tunneling current I while the tip is scanning the sample surface, so that the current I remains constant (**current set-point**) during the measurement. The vertical tip displacement as a function of the lateral tip position on the sample $z(x, y)$ at constant bias U is generally called **topography**. According to Eq. 1.5, the STM topographies follow contours of constant sample LDOS. The corrugation or contrast between maxima (z_{max}) and minima (z_{min}) in the topographies is affected by the choice of the current set-point: normally, the higher is the value of the current set-point, the stronger is the meausured corrugation. According to Eq. 1.5, the measured vertical tip displacement depends on the atomic and electronic structure of the scanned surface (Fig. 1.4).

1.1.3 Hamers model

A bias in the range of few mV is big enough to map metal surfaces by STM, but to understand the properties of semiconductors it is necessary to apply biases of some V because the energy bandgap of this class of materials does not provide electronic states which can support the tunneling current. In the latter case the Tersoff-Hamann (TH) model is no longer valid. R. J. Hamers extended in 1989 this model for tunneling at voltages $U \leq \Phi_{S,\,T}$ where Φ_S and Φ_T are the workfunctions of sample and tip, respectively [Ham89]. In the framework of the Jeffreys-Wentzel-Kramers-Brillouin (JWKB) approximation[1] Hamers suggested for the tunneling current I the following expression:

$$I = \int_0^{eU} D_S\left(r, E\right) D_T\left(r, E - eU\right) T\left(E, U, r\right) dE \tag{1.6}$$

where:

$$\begin{cases} T\left(E, U, d\right) = exp\left(-\dfrac{2d\sqrt{2m}}{\hbar}\sqrt{\dfrac{\phi_S + \phi_T}{2} + \dfrac{eU}{2} - \left(E - E_{||}\right)}\right) \\ \\ E_{||} = \dfrac{p_{||}^2}{2m} = \dfrac{\hbar^2 k_{||}^2}{2m} \end{cases}$$

In Eq. 1.6 $D_S\left(r, E\right)$ and $D_T\left(r, E\right)$ are the density of states of sample and tip at location r and total energy E of the tunneling electron, respectively. The reference for the energy $E = 0$ is chosen at the equilibrium point between sample and tip ($U = 0$). $E_{||}$ is the contribution of the electron energy parallel to the junction interface and $\vec{p}_{||} = \hbar \vec{k}_{||}$ is the corresponding crystal momentum. The tunneling probability T is a strong function of the component $\vec{k}_{||}$ of the total crystal momentum $\vec{k}$: for each value of the total energy E, the LDOS of the sample surface with a zero $\vec{k}_{||}$ component is heavily weighted by the tunneling probability T in Eq. 1.6.

In the framework of the Hamers model, STM topographies display a surface of constant LDOS(x,y) integrated from $E = 0$ to $E = eU$. Therefore it is not possible with biases in the range of few Volt to deduce directly the real sample LDOS from the STM topographies as in the case of small bias ($U \leq 10$ mV) where the TH model can be applied (Eq. 1.5).

---

[1] The JWKB method can be applied to give a direct solution of the one-dimensional Schroedinger equation $\frac{d^2\psi}{dx^2} + \frac{2m}{\hbar^2}[E - V(X)]\psi = 0$ in the case of slowly varying potentials $V(x)$ such that $|\frac{1}{k(x)}\frac{dk}{dx}| \ll k(x)$ where $k^2(x) = \frac{2m}{\hbar^2}[E - V(x)]$ [GL04].

Tip wave function χ_ν	Tunneling matrix element $M_{\mu\nu}\vert_{r=r_0} \propto$
s	ψ_μ
p_z	$\frac{\partial\psi_\mu}{\partial z}$
p_x	$\frac{\partial\psi_\mu}{\partial x}$
p_y	$\frac{\partial\psi_\mu}{\partial y}$

Table 1.1: Dependence of the tunneling matrix element $M_{\mu\nu}|_{r=r_0}$ on the tip (χ_ν) and sample (ψ_μ) wave function (from [Che88]).

1.1.4 Chen derivative rule

The TH model considers the tunneling state χ_ν of the tip as a s-wave function introducing a minimum feature-size L that STM can resolve [Che88]:

$$L_{min} = \frac{1}{\sqrt{2\pi\hbar\,(2m\phi_S)}} \approx 12.3\frac{1}{\sqrt{\phi_S}}\ (\text{Å}) \qquad (1.7)$$

Taking a typical value for the sample workfunction, $\phi_S \approx$ 3.5 eV, the maximum lateral resolution of STM would be $L_{min} \approx$ 6.6 Å. For large features on reconstructed surfaces, *i. e.* Au(110) 2×1 and 3×1, the typical feature size is 8-12 Å and the TH model can still account for the experimental data. On the other hand, early STM experiments in the late 80s showed that it was possible to get atomic resolution on close-packed metal surfaces and that the STM topographies were strongly dependent on tip modifications (*e. g.* [WWB$^+$89]). This implies that for atom-scale features with a typical lenght scale of 2-4 Å the TH model can not be used to explain the experimental data. Taking into account these results, C. J. Chen introduced in 1988 a new-three dimensional tunneling theory for interpreting *Scanning Tunneling Spectroscopy* (STS) measurements: the wave function χ_ν of the acting atom of the tip was expanded in terms of a complete set of eigenfunctions and it was found that the tunneling matrix element to or from an lth (or mth) component in the expansion is proportional to the lth (or mth) derivative of the sample wave function ψ_μ at the center of the acting atom r_0 [Che88]. We summarize this *derivative rule* in Table 1.1.

Tip wave function χ_ν	Sample wave function ψ_μ	Conductance distribution $g(r)$	Apparent radius ρ
s	s	e^{-2kr}	R
s	p	$\cos^2\theta e^{-2kr}$	$R/\left[1+1/kR\right]$
s	d	$\left(\cos^2\theta-\frac{1}{3}\right)^2 e^{-2kr}$	$R/\left[1+3/kR\right]$
p	s	$\cos^2\theta e^{-2kr}$	$R/\left[1+1/kR\right]$
s	d	$\left(\cos^2\theta-\frac{1}{3}\right)^2 e^{-2kr}$	$R/\left[1+3/kR\right]$

Table 1.2: Conductance distribution function $g\left(r\right)$ for different tip (χ_ν) and sample (ψ_μ) wave functions (as single localized surface states). The relations $\cos\theta = z/r$ and $k = \sqrt{2m\phi}/\hbar$ are implied (ϕ is the tunnel barrier height) (from [Che91]).

First principle calculations of the electronic states of W(001) clusters revealed in 1990 the existence of dangling-bond states near the Fermi level at the tip apex atom which could be ascribed to d_{z^2} states extending much further into the vacuum than atomic s states confirming the validity of the theory of Chen [OT90].

Using the *derivative rule* it is possible to calculate the tunneling matrix elements and the tunneling conductance $g\left(\vec{r}\right) \propto \left|M_{\mu\nu}\right|^2$ which allows us to define the apparent size of the atom or apparent radius ρ of the sample electronic state in the STM topography:

$$\rho = \frac{\partial g\left(\vec{r}\right)}{\partial z}\left(\frac{\partial^2 g\left(\vec{r}\right)}{\partial x^2}\right)^{-1} \tag{1.8}$$

where the xy-plane refers to the sample surface and the z-direction is orthogonal to this plane. As shown in Table 1.2, the apparent radius is reduced for p and d states in comparison with s state and the images of an atom looks much sharper as expected.

Not surprising, we observe the *reciprocity principle*: by interchanging the tip state and the sample state, the conductance distribution, and consequently, the apparent size of the image, is unchanged. Generally, for non-s-wave tip states, the tip apex follows a contour determined by the derivatives of the

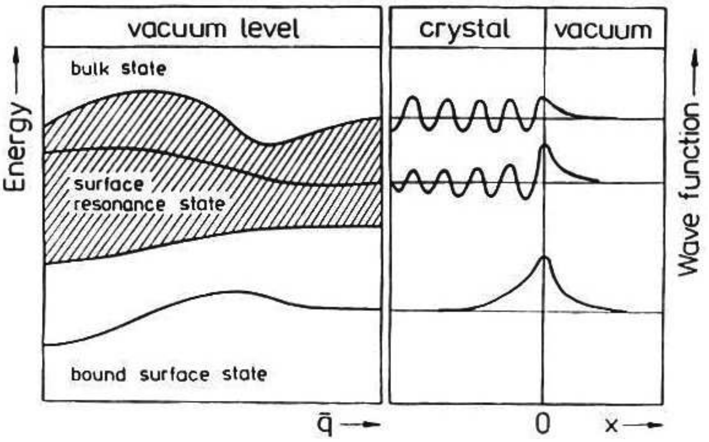

Figure 1.5: Scheme displaying (left) the surface band structure $E = E(\vec{q})$ of a semi-infinite crystal below the vacuum level and (right) the real part of the wave function for the three different types of electron energy states at the surface (from [End97]).

sample surface wave functions, which exibit much stronger atomic corrugation than the contour of the sample LDOS at E_{FS}.

In the case of semiconductors the charge distribution $e|\psi_\mu(\overrightarrow{r_S})|^2$ at the surface depends on three kinds of wave function ψ_μ associated to different types of electronic states (Fig. 1.5):

1. **bulk states**, which occur at energies in the allowed region of the projected bulk band structure, decay exponentially in vacuum and ehxibit undamped oscillations throughout the whole semi-crystal.
2. **bound surface states**, which occur at energies outside the allowed region of the projected bulk band structure and decay exponentially both in the bulk and in the vacuum.
3. **surface resonance states**, which occur at energies in the allowed region of the projected bulk band structure, decay exponentially in vacuum but decay less rapidly than bound surface states in the bulk.

STM can therefore provide information on electronic surfaces states or resonant bulk-like states up to some crystal-lattice planes below the surface, according to the decay-length of the electronic wave functions of the crystal surface in vacuum.

Surface states can be further classified in two groups:

- **intrinsic surface states** - these are the states associated to *dangling bonds (db)* and *back bonds (bb)* and are typical of clean and well-ordered surfaces. The *db* states appear at the surface of a semiconductor upon truncation of the bulk crystal and are the remaining lobes of the orbitals sticking out from the surface. The energy levels of such states are expected to be significantly shifted from the bulk values [LÖ1]. On the other side the *bb* states are related to surface-induced modifications of the chemical bonds between the topmost layers. The *bb* energy levels are usually shifted less than the *db* levels with respect to the bulk bands.

- **extrinsic surface states** - these are the states associated to imperfections of the semiconductor surface: missing atoms, line defects, surface steps, adsorbates. These states do not exhibit any 2D translational symmetry parallel to the surface and their wave functions are localized near the defects.

1.2 Experimental set-up

The experimental data presented in this work have been collected with a "beetle"-type scanning tunneling microscope which was built in our laboratory by T. Quast in 1995 [Qua95] following the construction proposed by K. Besocke in 1987 [Bes87]. Before starting the measurement, it is necessary to prepare the tungsten (W) tips that will be brought in tunnel contact with the semiconductor samples. The tips are chemically etched from a W wire, inserted in a shuttle chamber under vacuum conditions and then annealed to remove the oxide layer which covers them. Later the shuttle chamber is connected to the STM microscope where the samples and the tips are transferred through a load valve. Finally the STM measurement at room temperature takes place.

1.2.1 The STM system

The "beetle"-STM consists of two parts, the base and the top plate, which can be moved with respect to each other as shown in Fig. 1.6. The STM base contains the sample holder and three xy-scan-piezos, while the top plate contains the STM tip and the z-piezo. The vertical coarse and the lateral positioning of the tip on the sample takes place by rotating and by

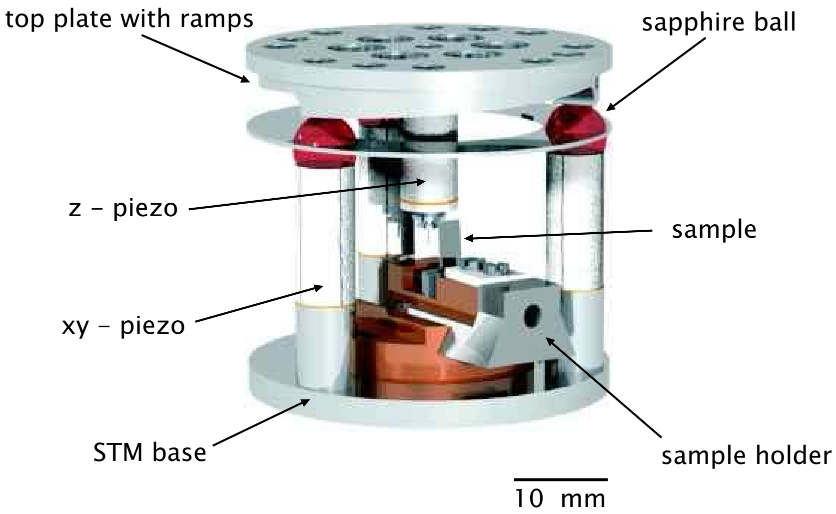

Figure 1.6: The “beetle”-type STM used in this this work and based on the design of Besocke (from [Hei98]).

moving laterally the top plate relative to the STM base respectively. Both diplacements are possible thanks to “slip-stick” movements of the STM top plate which is sliding on the three scan-piezos. The fine vertical positioning of the STM tip on the sample occurs via the z-piezo which brings the STM tip closer and closer to the sample until the set-point of the tunneling current I is reached.
In our STM system the total coarse vertical diplacement of the tip is around 1.5 mm, while the maximal z-piezo elongation is about $2\,\mu$m. The xy-piezos allow to scan a sample area with a diameter of few millimeter [Hei98].

The aim of this work is to characterize freshly cleaved semiconductor surfaces, therefore *Ultra High Vacuum* (UHV) conditions are necessary in the STM head. A combination of one ion pump, one sublimation titan pump and a liquid-nitrogen cooled vessel allows to reach in the STM chamber a pressure $p \leq 5\times10^{-11}$ mbar at room temperature. The STM head is placed in a small chamber and is accessible with an optical microscope through two CF 100 viewports (Fig. 1.7). On the top of the STM chamber a xyz-rotational manipulator allows to lift up the STM top plate from the scan piezos in order to allow the placement of tip and sample in the STM head without breaking the vacuum. In order to insulate the STM head from floor vibrations during the experiment, the STM-system can be suspended on three air damping supports. The construction is completed with a welded bellows manipulator to transfer the tip and sample into the STM head.

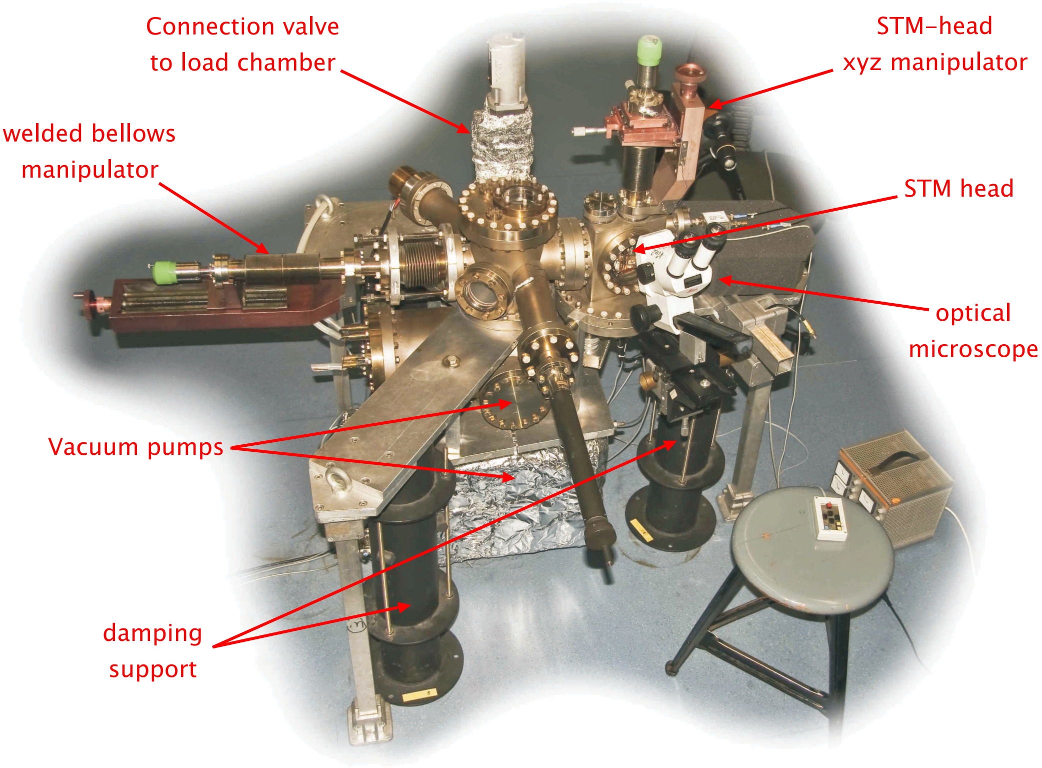

Figure 1.7: Top view of the STM system.

1.2.2 Tip preparation

The production of sharp STM tips is a key issue in order to get experimental STM data with atomic resolution. In our group we used a tip preparation technique developed at the University of Eindhoven [dR01]: a polycristalline tungsten wire of 250 μm diameter is electrochemically etched in a two molar (2M) KOH solution. The wire is etched at the separation surface between air and solution until it breaks in two pieces because of gravity pulling out a sharp apex with a typical curvature radius of less than 10 nm (Fig. 1.8(a)).

After the chemical etching the tip is covered with a thin insulating tungsten-oxide layer which has to be removed to get a conductive metal tip. Therefore a cleaning procedure is necessary: the tip is placed in a tip holder (Fig. 1.9), inserted in a transfer magazine and built in a UHV preparation chamber where three steps take place:

1. **annealing** - the tungsten-oxide layer is removed by heating the tip at about $\Theta = 800$ °C for $t = 20$ min. This treatment unfortunately

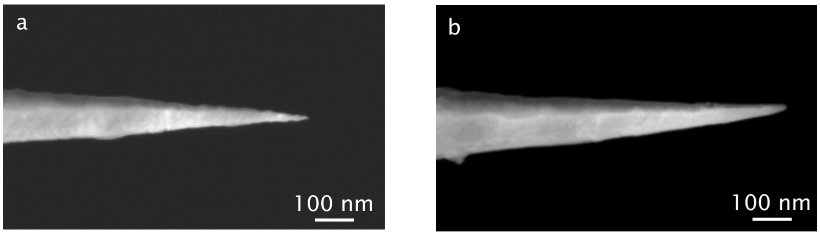

Figure 1.8: *Scanning Electron Microscope* (SEM) images of tungsten tips (a) after electrochemical etching and (b) after electrochemical etching, annealing, sputtering and characterization with field emission (from [Sch06]).

rounds the tip and increases the curvature radius at the tip apex.

2. **sputtering** - the tip apex is sharpened through argon ion sputtering with typical ion energy of 4 keV and ion current of 1 μA for t = 20 min. Different facets of tungsten react anisotropically to argon-ion bombardment and this process produces sharp tips.

3. **characterization with field emission** - high voltage is applied between the tip and a metal blade positioned few millimeters away from the tip ($0 < U < 1.5$ kV) and the emission current characteristic $i = i(U)$ is measured. Normally a current i of some μA flows between the two electrodes if U $\approx$ 100 V. The smaller one is the value of the applied voltage U at the onset of the current i, the sharper one is the tip [Luc04].

After the three-steps cleaning procedure the tungsten oxide layer covering the tip is removed. The tip apex radius is usually larger than just after electrochemical etching, but the emission current characteristic $i = i(U)$ of the tip becomes more stable. The stability of the tip is of capital importance during the STM experiment, because the tunneling current depends strongly on the electronic structure of the tip according to Eq. 1.6.

1.3 STM/STS methods and data analysis

The experimental STM methods we used to investigate our samples include the single-bias/multi-bias constant current topographies and the STS.
In **single-bias constant current topographies** the feedback loop of the

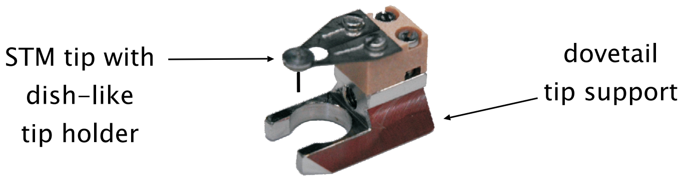

Figure 1.9: Tip holder with STM tip. The dovetail support fits into the STM-head base so that it is possible to change the tip without breaking the vacuum (from [Lot07]).

microscope keeps the value of the tunneling current constant while the tip scans the sample surface at set bias: the position of the tip on the sample surface (xy plane) is displayed as height information (z-direction) and the measured data show the atomic and electronic structure of the sample surface.

In **multi-bias constant current topographies** a set of STM topographies is simultaneously collected with different biases U_i (i=1, N). It is then possible to compare the tip height data (*z*) at a fixed position (*x, y*) on the sample surface as a function of the applied bias.

During a **STS measurement** a set of IU_i spectroscopies is collected for a discrete number i=(1, N) of points P_i on the sample surface as a function of the position ($x_i,\ y_i$) of the tip on the sample, of the applied bias and of the tip-sample distance. The IU spectra are collected while the tip follows a countour of constant surface LDOS. A normalization method is afterwards necessary to compare the IU spectra measured at different positions of the sample surface and two techniques, the topography normalization and the “Feenstra” technique, are introduced in the following pages.

The STM measurements and the evaluation of the data are performed through a software which has been written in our group by M. Wenderoth. By employing a noise reduction technique (“**template-method**”) developed by J. Garleff it is possible to extract out of the experimental data the contribution of the unperturbed surface and to set apart the effect of defects and adsorbates on the sample surface.

1.3.1 Single-bias constant current topographies

All the STM topographies presented in this work are collected applying a bias at the sample and keeping the tip grounded. This means that we investigate with $U < 0$ the filled states and with $U > 0$ the empty states of the sample surface (Fig. 1.10).

If the tip is brought at a distance of $5 - 10$ Å from a semiconductor surface,

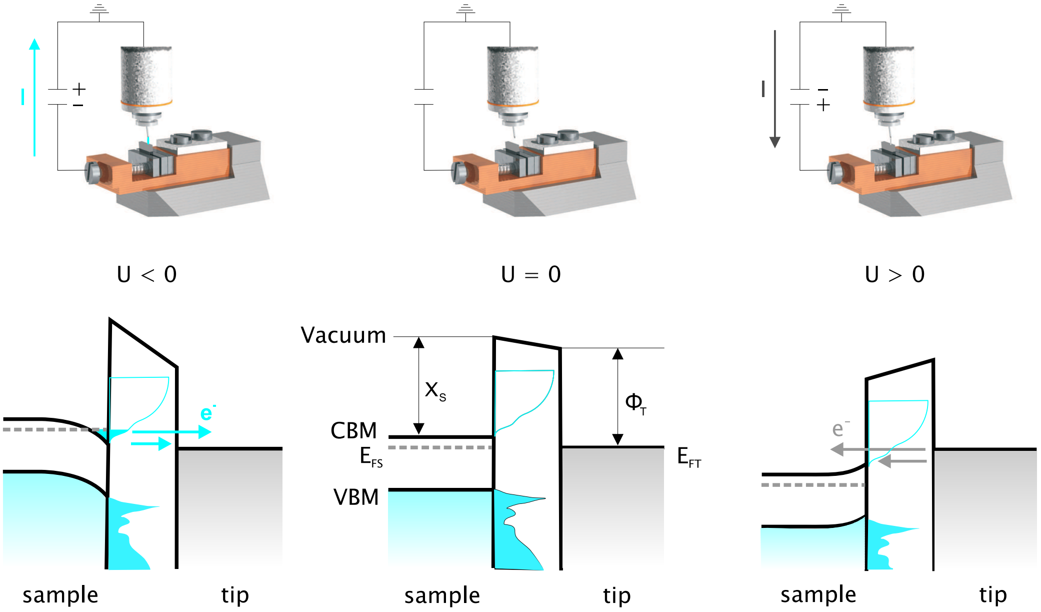

(a) (b) (c)

Figure 1.10: Voltage dependent STM measurement (top images) and corresponding energy levels schemes of a n-doped semiconductor sample in tunneling contact with tip (bottom images): (a) negative bias U applied to the sample ($U < 0$, tunneling of electrons out of sample filled states), (b) equilibrium between sample and tip ($U = 0$), (c) positive bias U applied to the sample ($U > 0$, tunneling of electrons into sample empty states). χ_S and ϕ_T are the electron affinity of the sample and the work-function of the tip, while E_{FS} and E_{FT} indicate the Fermi energies of sample and tip, respectively; the conduction band minimum of the sample is indicated with CBM and the valence band maximum with VBM.

typically a tunneling current $I \approx 10 - 500$ pA is measured applying a bias $|\mathrm{U}| \approx 1 - 3$ V. In the constant current mode, a feedback loop adjusts the vertical position of the tip during scanning so that the tunneling current I stays constant (current set-point). The tip scans the sample surface at a fixed position y_1 along the positive x direction (*trace*) and then along the negative x direction (*retrace*). Then a new point y_2 is set and the tip proceeds scanning along x as before. During scanning the vertical displacement $z = z(x,\ y)$ of the tip is measured in discrete points of each row and is represented as colour-scaled information as a function of the position of the tip on the sample surface.

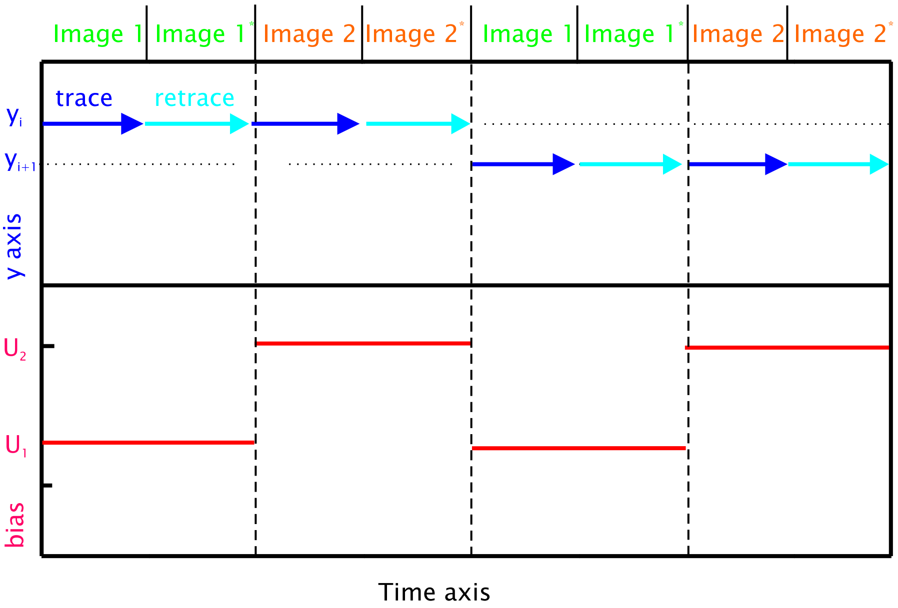

Figure 1.11: Schema of STM multi-bias measurement (U_j with j=1, 2) depending on time: the red line shows the applied bias U, the blue (cyan) line shows the trace (retrace) scan at different positions y_i of the STM topographies (i=1, N) (from [Tei07]).

1.3.2 Multi-bias constant current topographies

The comparison among STM topographies which have been measured with constant tunneling current and different bias shows the energy dependence of the LDOS for each position $P = P(x, y)$ of the sample surface. Unfortunately it is not possible to compare two different STM topographies measured one just after the other due to thermal drift of the STM system and non-linearity of the piezo elements.

In order to solve the problem it is necessary to collect *quasi*-simultaneously the two STM topographies (Fig. 1.11): the tip scans (*trace* and *retrace*) the sample surface at position y_i with applied bias U_1 keeping the tunneling current constant. Then the bias is switched to U_2 and the line-scan is repeated. Finally the tip moves to the next position y_{i+1} and the procedure is repeated. Each row of the STM topography is collected first with bias U_1 and directly after U_2: one can therefore compare the two data-sets on each point $P = P(x, y)$ of the sample surface. In this way it is also possible to eliminate the effect on the STM data of tip modifications which usually occur during scanning.

1.3.3 Scanning Tunneling Spectroscopy

The STS is a powerful method to get insight into the electronic properties of a surface. In our experimental set-up a STS measurement consists of four steps which are repeated for a discrete number i=(1, N) of points $P_i = P_i\,(x, y)$ of the sample surface as illustrated in Fig. 1.12:

I. **constant current topography** - the tip is brought in tunnel contact with the sample surface and the vertical displacement of the tip $z_i = z_i\,(x, y)$ is measured at the sample-tip distance $d_{i0} = d_{i0}(x, y)$ fixed by the current-bias set-point $SP_0 = SP_0\,(I_0, U_0)$.

II. **barrier height evaluation** - the feedback loop of the STM set-up is interrupted and the height of the tunnel barrier is derived: the tip is brought to vertical positions $d_{i1} = d_{i0} - \Delta d/2$ and $d_{i2} = d_{i0} + \Delta d/2$ and the corresponding tunneling currents I_{i1} and I_{i2} are measured. According to Eq. 1.1 we have:

$$\Delta ln I_i = ln \frac{I_{i2}}{I_{i1}} = ln \left(\frac{e^{-2k_i d_{i2}}}{e^{-2k_i d_{i1}}} \right) = -2k_i \Delta d \qquad (1.9)$$

where $k_i = \frac{1}{\hbar}\sqrt{2m\phi_i}$.
If we substitute the value of k_i in Eq. 1.9 we can derive the tunnel barrier height ϕ_i:

$$\phi_i = \frac{\hbar^2}{2m} \left(\frac{\Delta ln I_i}{\Delta d} \right) \qquad (1.10)$$

III. IU_i **spectrum measurement** - a bias U ramp is applied to the sample and the tunneling current $I_i = I_i\,(U)$ is measured. During this step the feedback loop is still open and the tip stays at constant distance d_{0i} from the sample.

IV. **reactivation of the feedback loop** - the tip moves to the next point $P_{i+1} = P_{i+1}\,(x, y)$ and the feedback loop is closed.

This procedure is repeated for each row at position y_j of the scanned STS map of the sample surface. At the end the STS data give a map of the $LDOS = LDOS(x, y, E, d_{0i})$ which means that we get insight into the sample surface LDOS as a function of the tip position on the sample surface $P_i = P_i\,(x, y, d_{0i})$ and of the energy E of the tunneling state.
It is difficult to compare directly the IU_i spectra measured at different positions $P_i = P_i\,(x, y)$ on the sample surface because the STS data are collected

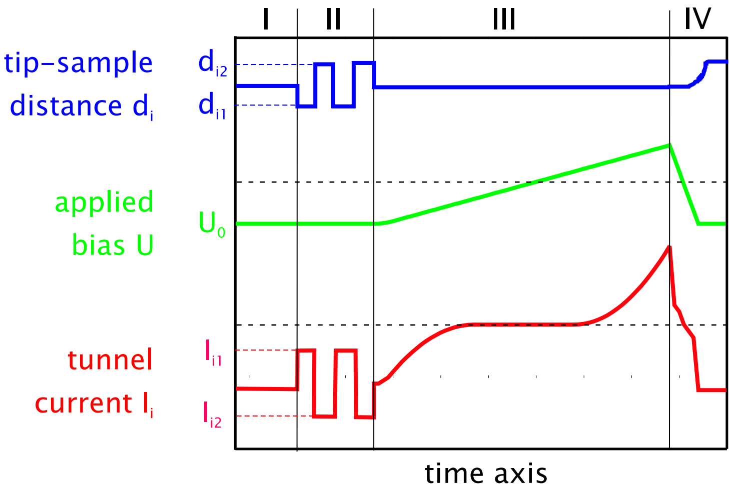

Figure 1.12: Schema of STS measurement as a function of time: constant current topography (step I), barrier height evaluation (step II), IU_i $(i = (1, N))$ spectrum measurement (step III) and reactivation of the feedback-loop (step IV). The black dot line represents the zero (from [Tei07]).

keeping constant the set-point $SP_0 = SP_0\,(I_0, U_0)$. This means that all spectra are measured on a surface of constant LDOS of the sample surface and not at the same distance between tip and sample (a sort of "eggs"-carton profile). To compare the spectra it is therefore necessary to apply a normalizing procedure. But before introducing these techniques for STS data analysis, we must point out that in the case of STS measurements at the edges of the energy bandgap of semiconductor surfaces it is usually necessary to increase the value of the tunneling current to highlight features of the spectra that could be covered by the noise of the STM set-up. To increase the current at constant applied bias it is necessary to reduce the distance d between tip and sample (if the distance d is reduced of 1 Å then the current increase of around a factor 10). Normally the vertical shift Δd of the tip is changed linearly on the applied bias and is of the order of 1 Å/V. For each point P_i of the STS image it is necessary to normalize the spectrum IU_i from $d_i = d_i(U)$ to the constant value $d_i = d_{i0}$ fixed by the STM set-up during the constant current topography measurement at set-point $SP_0 = SP_0\,(I_0, U_0)$ (**z-shift normalization**):

$$I_i(U)|_{d_i=d_{i0}} = I_i(U, d_i(U))e^{2k_i(d_i(U)-d_{i0})} \tag{1.11}$$

where $k_i = \frac{1}{\hbar}\sqrt{2m\phi_i}$. The inverse decay lenght k_i is calculated for each point P_i of the STS map once evaluated the barrier height ϕ_i (Eq. 1.10).

This normalization method is applied in the hypothesis that the shape of the vacuum barrier between tip and sample does not change during the shift Δd of the tip. In order to check the effect of this assumption on the STS data it would be always better to repeat the measurement without z-shift and then to compare the experimental results.

Once each IU_i spectrum at position P_i of the sample surface has been normalized at a constant distance d_{i0} between sample and tip, we can proceed to compare different spectra collected in the same STS map. Several methods have been introduced to perform the normalization of the experimental data and we will present two of them in this work, the topography normalization and the method suggested in 1987 by R. M. Feenstra and his co-workers:

1. **Topography normalization** - all the IU_i spectra measured at different distances d_{i0} between tip and sample are normalized to a medium distance d_M for all points P_i of the STS map:

   $$I_i(U)|_{d_i=d_M} = I_i(U, d_i(U))e^{2k(d_i(U)-d_M)} \tag{1.12}$$

   In this way all the spectra of the STS map are normalized to a plane of constant distance d_M from the sample surface.

2. **Normalization according to Feenstra *et al.*** - in 1987 R. M. Feenstra, J. A. Stroscio and A. P. Fein proposed a method to evaluate the LDOS of a semiconductor surface by calculating the ratio between the differential dI/dU and the total I/U conductivity [FSF87]. The authors showed that it is afterwards possible to remove the dependence of the $I = I(U)$ characteristic on the tip-sample distance.

   According to Eq. 1.6 the differential conductivity at a fixed position $r = r_0$ is given by

   $$\begin{aligned} \frac{dI}{dU} &= D_S(E)\,D_T(E-eU)\,T(E,U) + \\ &+ \int_0^{eU} D_S(E)\,D_T(E-eU)\,\frac{dT(E,U)}{dU}\,dE + \\ &+ \int_0^{eU} T(E,U)D_S(E)\frac{dD_T(E-eU)}{dU}\,dE \end{aligned} \tag{1.13}$$

If we suppose as a first rough approximation that the LDOS of the tip is constant ($D_T(E - eU) = D_{T0}$), the third term in Eq. 2 disappears and the differential conductivity dI/dU is given by the sum of two terms: the first term is proportional to the LDOS of the sample $D_S(E)$ evaluated at energy E while the second term depends on the variation of the transmission coefficient T with energy E and applied bias U. Within the JWKB approximation the coefficient T results to be a monoton increasing function of the applied bias U for any fixed energy $E = E_0$ so that the second term in Eq. 2 contributes a smoothly varying "background" on which the spectroscopic information in the first term is superimposed. In order to extract these pure STS data from the measurement Feenstra suggested to consider the ratio between the differential dI/dU and the total I/U conductivity:

$$\frac{dI/dU}{I/U} = \frac{D_S(E) + A(U)}{B(U)} \tag{1.14}$$

where:

$$\begin{cases} A(U) = \displaystyle\int_0^{eU} \frac{D_S(E)}{eT(eU,U)} \frac{dT(E,U)}{dU} dE \\[2ex] B(U) = \displaystyle\frac{1}{eU} \int_0^{eU} D_S(E) \frac{T(E,U)}{T(eU,U)} dE \end{cases}$$

Feenstra has deduced that, since $T(E,U)$ and $T(eU,U)$ appear as ratios in both terms $A(U)$ and $B(U)$, their exponential dependences on the tip-sample distance d and applied bias U tend to cancel. So the ratio between the differential dI/dU and the total I/U conductivity gives a measure of the sample surface LDOS:

$$\frac{dI/dU}{I/U} = D_S(E) \equiv LDOS_S(E) \tag{1.15}$$

J. A. Stroscio *et al.* checked experimentally the validity of the normalization method suggested by Feenstra measuring the tunneling current as a function of applied bias, lateral position, and vertical separation between a tungsten probe tip and a Si(111) 2×1 surface [SFF86]. They showed that most of the dependence of the tunneling

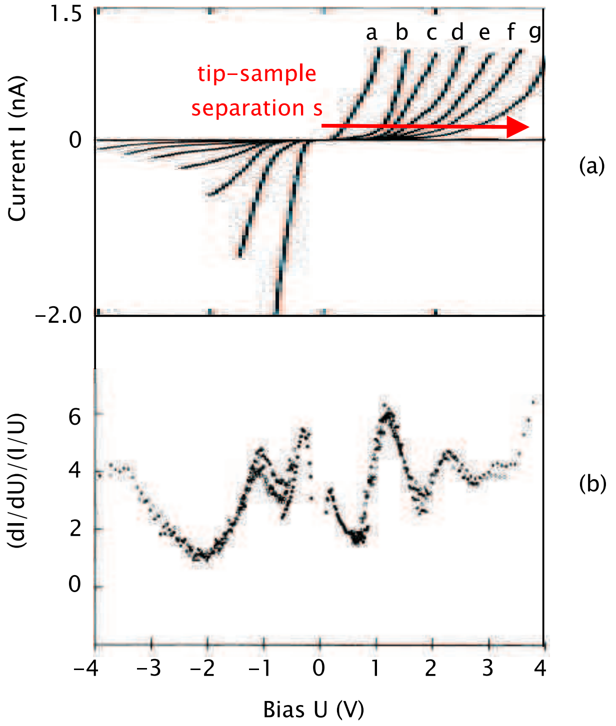

Figure 1.13: (a) Tunneling current versus voltage IU for a tungsten probe tip and Si(111) 2×1 sample, at tip-sample separations s of 7.8, 8.7, 9.3, 9.9, 10.3, 10.8 and 11.3 Å for the curves labeled a-g, respectively. (b) Ratio of differential to total conductivity: the circles, open squares, filled triangles, open triangles, filled squares, open lozenges and filled lozenges refer to the curves a-g respectively from image (a) (from [SFF86]).

current I on both tip-sample separation and applied bias can be removed by computation of the ratio of differential to total conductivity $(dI/dU)/(I/U)$ (Fig. 1.13).

Two relevant topics concerning the normalization method suggested by Feenstra must be considered: the comparison of the normalized IU data with the true densitiy of states of the sample and the effect of the tip density of states in STS measurements.

- **Comparison of the normalized IU data with the true density of states of the sample**
  For large bandgap semiconductor surfaces the ratio of the differential dI/dU to the total I/U conductivity diverges at the band edges, simply because the current I approaches zero faster than the differential

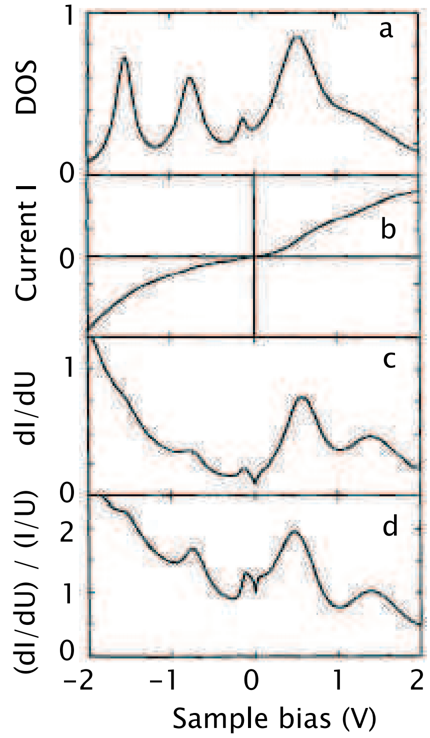

Figure 1.14: Numerical simulations of tunneling spectrum IU and normalized results: (a) Original density of states function (DOS), (b) tunneling curve IU calculated by numerical integration of tunneling equations, (c) first derivative spectrum, (d) normalized derivative spectrum $(dI/dU)/(I/U)$ (from [Ham89]).

conductivity dI/dU. P. Mårtensson and Feenstra solved this problem by broadening the total conductivity I/U. The broadening is done with a one-pole Fourier low-pass filter, with the pole frequency given by ΔU^{-1} ($\Delta U \approx$1 V) [rF89]. Finally when the current I goes below the noise level of the STM set-up it is necessary to choose a suitable current cutoff value.

Hamers has shown in 1989 with a theoretical calculation that the method suggested by Feenstra gives a correct evaluation of the position of the relevant LDOS features in the case of semiconductor surfaces: an artificial density of states was created (Fig. 1.14(a)) and then numerically integrated to obtain the IU curve predicted from standard tunneling theory (Fig. 1.14(b)). This was then differentiated to give the plot of the partial conductivity dI/dU (Fig. 1.14(c)) and normalized to the total conductivity I/U to produce the LDOS spectrum (Fig. 1.14(d)) [Ham89]. Comparing the starting DOS function (Fig. 1.14(a)) with the normalized spectrum (Fig. 1.14(d)) we observe that the two plots show peaks at nearly the same positions but the intensities of the peaks are quite different. Empty states of the sample ($U > 0$) are observed much more clearly and with higher intensity in the normalized tunneling spectra than filled states. On the other hand the normalized differential conductivity (Fig. 1.14(d)) reproduces better the peaks at small negative bias U than the mere differential conductivity (Fig. 1.14(c)).

The STM/STS experiments of Mårtensson and Feenstra confirmed the theoretical conclusions of Hamers about the correcteness of the normalizing method for the determination of the positions of relevant peaks in the LDOS plot: the two authors found that for the Sb/p-GaAs(110) system the choice of the broadening width ΔU affects the amplitude of the peaks observed in the LDOS spectra but not the positions of the peaks themselves [rF89].

- **Effect of the tip density of states in STS measurements**
  In the expression of the tunneling current I according to Hamers (Eq. 2) appears the density of states of the tip $D_T(E - eU)$. The rough approximation of considering the tip density as constant is correct only for small applied bias. In the case of STS experiments on semiconductors where $|U| \approx 1-$ 5 V we must consider the effect of the tip DOS on the measured spectra. In fact the transmission probability is strongly peaked for states near the Fermi level of the negatively-biased electrode [FSF87]. Thus, it should be difficult to observe low-lying occupied surface states with tunneling spectroscopy. This prediction has been confirmed theoretically in 1990 by J. E. Griffith and G. P. Kochanski who made a simulation of a tunneling spectroscopy experiment assuming a uniform tip and sample DOS with a 10% ripple added [GK90]. The $(dI/dU)/(I/U)$ versus U plot reflects clearly the slow wiggles of the sample DOS only for positive bias U whereas, at negative bias U, the curve shows the fast wiggles characteristic of the tip DOS (Fig. 1.15).

  In 1996 V. A. Ukraintsev made a systematic study of LDOS deconvolution from tip-surface spectra and proposed a new technique to recover the sample LDOS: the differential conductivity dI/dU is normalized to its fit to the tunneling probability function T [Ukr96]. This study confirmed the difficulties encountered by STM in probing deep occupied states of surfaces: if the input tip and sample DOS are sine functions, the deconvoluted DOS resembles the tip DOS at negative

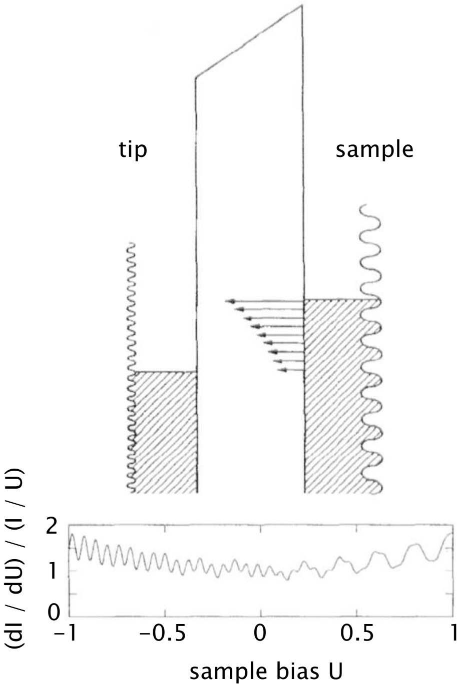

Figure 1.15: Upper image: energy levels schema of a tunneling junction where tip (left) and sample (right) DOS are characterized by fast and slow wiggles, respectively. Hatched areas correspond to filled states below the Fermi energy E_F. The lenght of the arrows is proportional to the tunneling transmission factor T at a given energy E. Lower image: computed spectroscopic characteristic of the system (displayed as $(dI/dU)/(I/U)$): the curve contains information about both tip and sample DOS (from [GK90]).

and the sample DOS at positive bias U, respectively, as in the simulation of Griffith (Fig. 1.16(a)). Even if the tip DOS is constant, recovery by any known method would not correctly present the density of sample occupied states (Fig. 1.16(b)). In the case of a typical semiconductor sample DOS the deconvolution of the spectra gives a good matching to the input data for states lying close to the valence band maximum (VBM), while the influence of the tip DOS remains significant for deeper occupied states (Fig. 1.16(c)).

In 1998 A. L. Vazquez de Parga showed in a combined theoretical and experimental STS study on Cu(111) the marked impact of the tip DOS on the tunneling conductance: the data depend strongly on the crystalline structure and morphology of the tip apex [dPHM$^+$98].

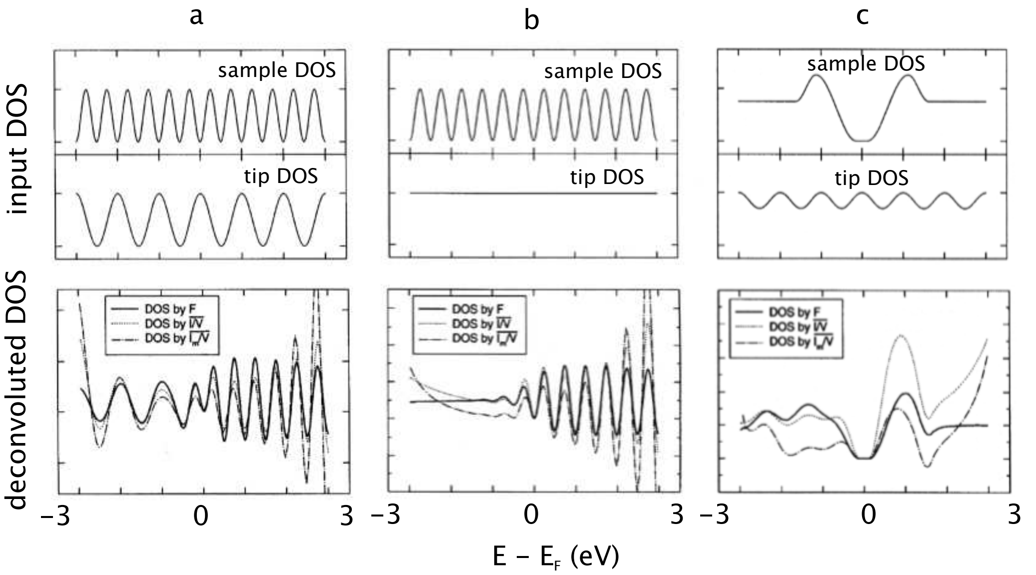

Figure 1.16: Top graphs: input sample (upper) and tip (lower) DOS: (a) sample and tip DOS as sine funtions, (b) sample DOS as sine function and tip DOS as constant, (c) sample DOS semiconductor-like and tip DOS as sine function. Bottom graphs: the differential conductivity dI/dU normalized to asymmetric tunneling probability F (solid line), the differential conductivity dI/dU normalized to total conductivity $\overline{I/U}$ at constant tip-sample separation (dot line), and the differential conductivity dI/dU normalized to total conductivity $\overline{I_m/U}$ at variablet tip-sample separation (dash-dot line) are displayed (from [Ukr96]).

Because of the influence of tip DOS in STS experiments, the only way to extract reliable data about the sample LDOS is to repeat the measurements with different tips and samples and to choose only the LDOS features that systematically appear independently from tip and sample.

1.3.4 Templates in periodic structures

In STM topographies the periodic structure of the surface is broken by defects (*i. e.* buried donors) or disturbed by backgound noise in the tunneling current I. In order to extract from the experimental data the contribution in the STM topographies of the periodic undisturbed semicondutor surface we used the so-called “template” method which was developed in 2005 in our group [Gar05]. The method is illustrated in Fig. 1.17. First of all a

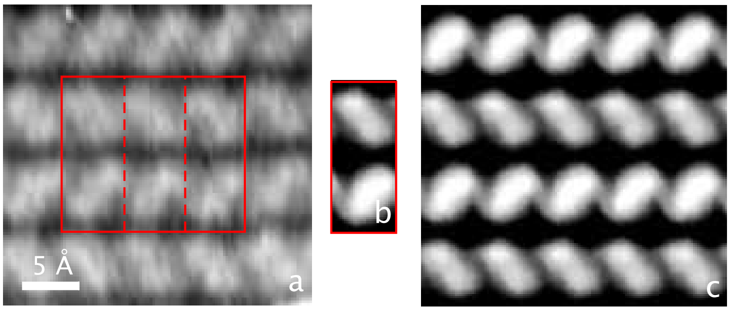

Figure 1.17: "Template" method: (a) the 2D-lattice is superimposed on the raw STM data, (b) the "template" unit-cell is derived by adding the raw data at equivalent positions and dividing the result for the number of unit-cells contained in the 2D-lattice, (c) the "template" is periodically repeated to emphasize the electronic structure of the undisturbed sample surface.

2D lattice consisting of an integer number N of surface unit cells is superimposed to the identifiable periodic structure of the STM topography (Fig. 1.17(a)). Then the raw data at equivalent positions of the unit cells are added and the result is divided for N. This procedure generates the so called "template" or "undisturbed" surface unit cell which shows the atomic and electronic structure of the ideal surface (Fig. 1.17(b)). Finally this template is periodically repeated in order to get an overview on the structure of the undisturbed surface (Fig. 1.17(c)). The background noise can be reduced of a factor $\sqrt{N}/N$. Thanks to the noise reduction, it is usually possible to recognize weak effects in the template image which in the raw data are covered by background noise.

Chapter 2

Physical Properties of non-polar SiC and GaN surfaces

This chapter introduces the principles used to describe the atomic and electronic properties of semiconductor surfaces (Sec. 2.1). Then we briefly discuss an important property of hexagonal compound semiconductors, the polarization (Sec. 2.2). These semiconductors are in fact *spontaneously polarized* due to the lack of inversion symmetry along the c-axis and are *piezoelectrically polarized* if they are under mechanical stress. Finally in Sec. 2.3 and Sec. 2.4 we focus our attention on the two semiconductor polytypes 6H-SiC and 2H-GaN which are the object of investigation in this work.

2.1 Principles of surface reconstruction

An ideal semiconductor crystal is a 3D arrangement of atoms whose structure is defined in terms of its *Bravais lattice* which is an infinite regular array of *points* that fills all space [Une96]. Upon cleavage, a surface is created and the regular periodicity of the crystal is interrupted: part of the chemical bonds which build up the bulk-crystal are broken and the atomic and electronic structure near the surface is markedly different from the bulk one.

If the atomic structure of a clean semiconductor surface exhibits the same symmetry as the truncated bulk solid, we use the Wood notation and refer to it as "(1×1)" structure. However, the atomic positions of the surface atoms can differ from those of their bulk counterparts by as much as 1 Å and this kind of surface is called *relaxed* relative to the truncated bulk one. The movement of the top-layer atoms along the direction ortogonal to the truncated bulk surface is called *buckling*.

In many cases, the instability of the surface layers associated with the tendency to saturate dangling bonds causes the surface layer to exhibit a lower symmetry parallel to the surface than the truncated bulk solid. In this case the surface is said to be *reconstructed* [Duk96].
The driving force in relaxations and reconstructions of semiconductor surfaces is the lowering in energy of electronic surface states associated with the rehybridization of the dangling bonds characteristic of a truncated bulk surface.

2.1.1 Atomic structure

The atomic geometry of the uppermost atomic layers of semiconductor surfaces is determined by chemical forces which tend to saturate the valences of the atomic species in these layers. If chemical bonds are formed in this process, the energy gain is substantial in the order of 1 eV per atom per bond [Cha89]. These bonds form a new surface compound which places the substrate under elastic stress. The substrate atoms relax to new equilibrium positions. The energy gain in this relaxation is about 0.01 eV per surface atom [Duk93].
C. B. Duke gives an overview on the principles ruling surface reconstruction in the case of tetrahedrally coordinated semiconductors, where the atomic and electronic properties of the freshly cleaved surface are determined by the need of saturating the dangling bonds appearing at the top-layer upon truncation [Duk96]:

1. Reconstructions tend to either saturate surface dangling bonds via rehybridization or to convert them into non-bonding electronic states. For example on the (100) faces of both elemental and compound semiconductors, dimers form to saturate the valences of the surface atoms.

2. In many cases (and all quasi one-dimensional ones) surfaces can lower their energies by atomic relaxations leading to semiconducting surface state spectra as opposed to metallic ones.

3. The surface structure observed will be the lowest energy structure kinetically accessible under the preparation conditions.

4. Surfaces tend to be autocompensated. This principle plays a key role during the cleavage of compound semiconductors where charge transfer from the cation to the anion takes place: typically cation dangling bond orbitals at surfaces occur at higher energies than the

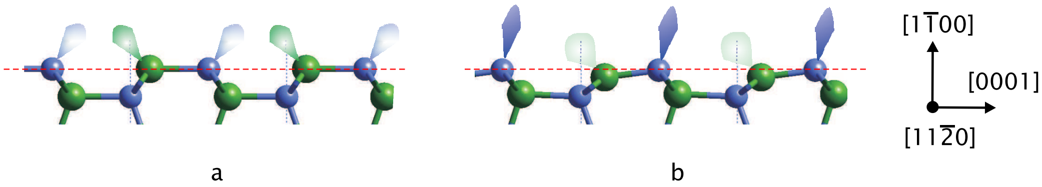

Figure 2.1: Side view of the (a) truncated and (b) relaxed GaN(1$\bar{1}$00) surface. Ga (N) atoms are indicated with green (blue) spheres. The red dotted line indicates the truncated (1$\bar{1}$00) plane.

corresponding anion dangling bond orbitals. If the surface has to remain uncharged, the anion-derived (cation-derived) orbitals must be partially or completely occupied (empty). The amount of electronic charge which is transferred from the cation dangling bond to the anion dangling bond depends on the ionicity of the cation-anion pair. Such a surface is said to be “autocompensated”.

5. For a given surface stoichiometry, the surface atomic geometry is determined mainly by a rehybridization-induced lowering of the surface state bands associated with the filled anion dangling bond orbitals.

Tetrahedrally coordinated compound semiconductors occur in two crystallographic allotropes: zincblende and wurtzite. Zincblende materials exhibit a single cleavage face, the (110) surface, which constists of equal numbers of anions and cations which form zig-zag chains along $< 110 >$ directions on the surface. Wurtzite materials exibit two cleavage faces, both consisting of equal numbers of anion and cation species: the (1$\bar{1}$00) surface consists of isolated anion-cation dimers back-bonded to the layer underneath, whereas the (11$\bar{2}$0) surface consists of anion-cation chains, analogous to those on zincblende (110) but with four rather than two inequivalent atoms per surface unit cell (ref. Fig. 2.18). All three surfaces exibit relaxations which do not alter the symmetry of the surface unit cell but which lead to large ($\approx$ 1 Å) deviations from the bulk atomic positions in the uppermost layer along the direction ortogonal to the surface [Duk96].
As an example of this behavior Fig. 2.1 shows a comparison between the truncated and the relaxed GaN(1$\bar{1}$00) surface: upon truncation the Ga-atoms relax moving inward by about 0.29 Å while N-atoms are almost unchanged.

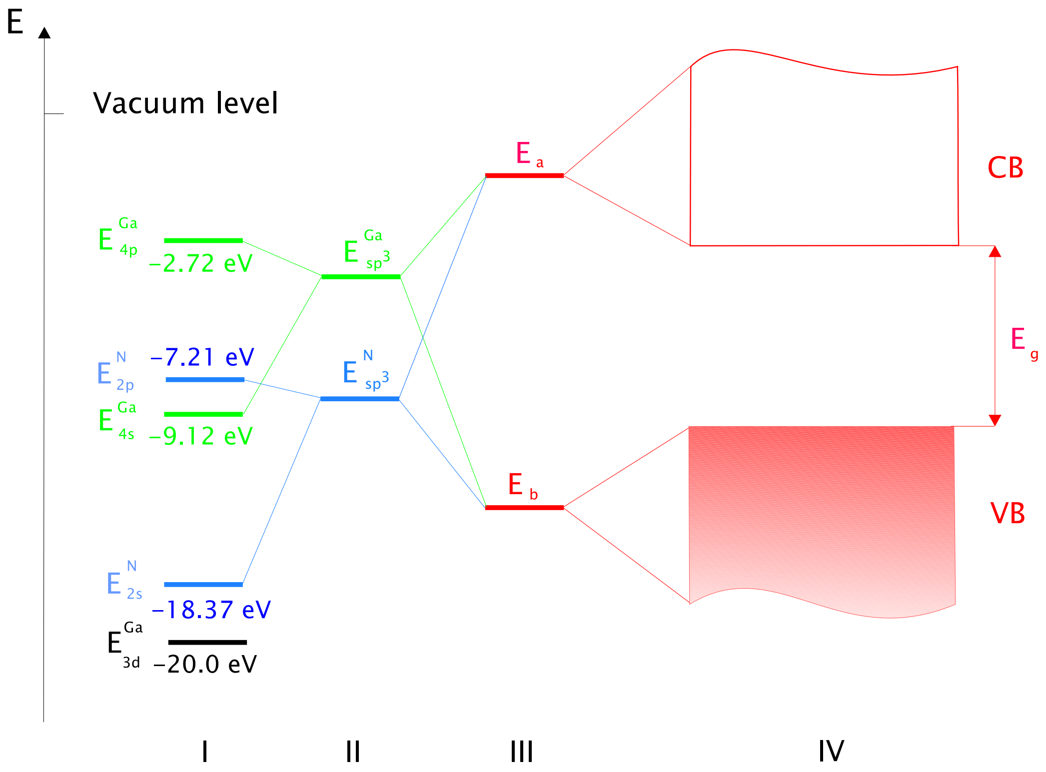

Figure 2.2: Energy level scheme for the generation of the GaN crystal: (I) higher free-atom E_s, E_p and E_d energy levels for Ga and N [FMS93], (II) formation of $E_{sp^3} = (E_s + 3E_p)/4$ hybrids, (III) bonding E_b and antibonding E_a combination between two hybrids, (IV) broadening of bonding and antibonding states into the valence band (VB) and conduction band (CB), respectively.

2.1.2 Electronic structure

Fig. 2.2 shows on an energy scale the steps that lead from the single atoms to the formation of a tetrahedrally coordinated compound semiconductor, taking as an example the GaN crystal. Starting from atomic levels on each atom (Fig. 2.2(I)), sp^3 hybrids are generated and oriented towards their nearest neighbors to build up the rising bond (Fig. 2.2(II)). Then the linear combination of two sp^3 hybrids generates two new states, the bonding E_b and the antibonding E_a orbital (Fig. 2.2(III)). Finally the overlap of an infinite number of bonding and antibonding orbitals gives rise to the valence and conduction band, respectively (Fig. 2.2(IV)). The two bands are separated by the so-called energy gap E_g.
Upon truncation of a crystal, a part of the chemical bonds which constitute the bulk-structure are broken and therefore the electronic properties at the

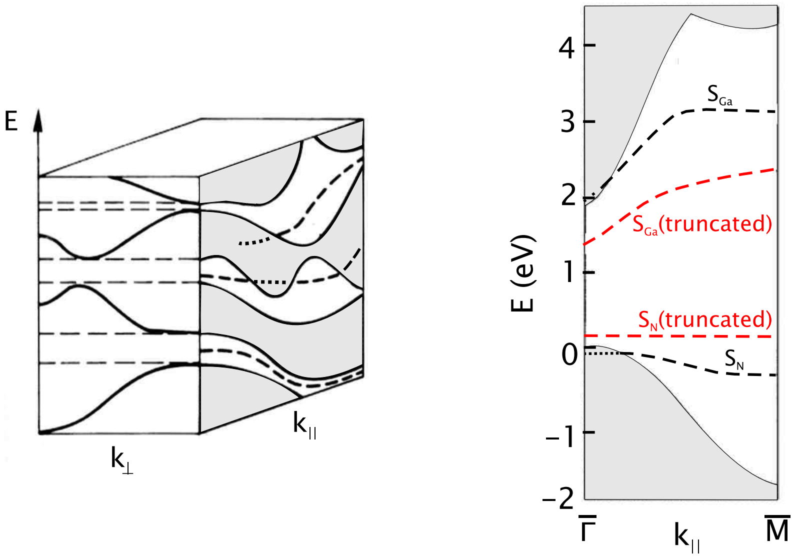

(a)

(b)

Figure 2.3: (a) Hypothetical band structure of a crystal. The shaded areas in the $E(k_{||})$ plane describe the projected bulk band structure (along $k_\perp$). Dashed lines in the $E(k_{||})$ plane indicate surface state bands in the gap of the projected bulk band structure, and dotted lines show surface resonances with bulk states (from [LÖ01]). (b) Band structure calculated for the GaN(1$\bar{1}$00) surface within the *Local Density Approximation* (LDA): surface state bands S_N and S_{Ga} are indicated with red (black) dotted lines for the truncated (relaxed) surface. The shaded region corresponds to the projected bulk band structure (from [NN96]).

surface are markedly different compared to the bulk ones. Even a truncated surface with its atoms at bulk-like positions displays new electronic levels. In the ideal case of a semi-infinite crystal, the most general one-electron wavefunction ϕ_{SS} for states localized near an ideal surface has plane-wave (Bloch) character for coordinates parallel to the surface $\vec{r}_{||} = (x, y)$:

$$\phi_{SS}(\vec{r}_{||}, z) = u_{\vec{k}_{||}}(\vec{r}_{||}, z)e^{i\vec{k}_{||}\cdot\vec{r}_{||}} \tag{2.1}$$

where $\vec{k}_{||} = (k_x, k_y)$ is a wave vector parallel to the surface [LÖ01]. The modulation function $u_{\vec{k}_{||}}$ has the periodicity of the surface and is labelled according to the wave vector $\vec{k}_{||}$. Each surface state is then described by its wave vector $\vec{k}_{||}$ and its energy level E_{SS}. For bulk states both $\vec{k}_{||}$ and $\vec{k}_\perp$

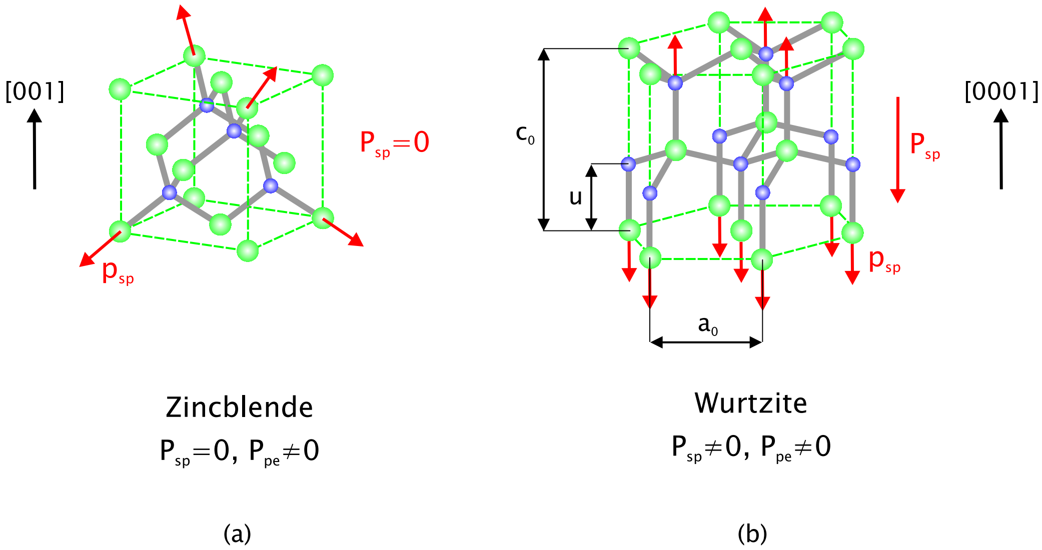

Figure 2.4: (a) Metastable zincblende and (b) stable wurzite phase of GaN: the sum of the microscopic dipoles $\vec{p}_{sp}$ results in zero and non-zero spontaneous polarization $\vec{P}_{sp}$ in the zincblende and wurtzite phase, respectively. Ga(N) atoms are indicated with green(blue) spheres.

components are allowed. For each value of $k_{||}$ therefore, a rod of $k_{\perp}$ values extends back into the bulk 3D Brillouin zone; bulk energy bands being cut by this rod yield a bulk state in the $E(k_{||})$ plane.

Fig. 2.3(a) shows a scheme of surface state bands (broken lines) plotted together with the projection of all bulk states (shaded areas) on a particular $E(k_{||})$ plane. True surface state bands are characterized by energy levels E_{SS} that are not degenerate with bulk bands and they lie in the gap of the projected bulk-band structure (dashed lines). Surface state bands, however, can penetrate into a part of the surface Brillouin zone, where propagating bulk states exist. They are then degenerate with bulk states and can mix with them. These states are known as surface resonances (dotted lines) (see also Fig. 1.5).

Fig. 2.3(b) shows as an example the calculated electronic band structure for the truncated and relaxed GaN($1\bar{1}00$) surface: the main relaxation mechanism consists of a slight buckling rehybridization, with N atoms tending to adopt p^3 coordination and Ga atoms adopting an sp^2 configuration. The effect of atomic relaxation is to increase the gap between the surface state S_N and S_{Ga} bands by more than 1 eV [NN96].

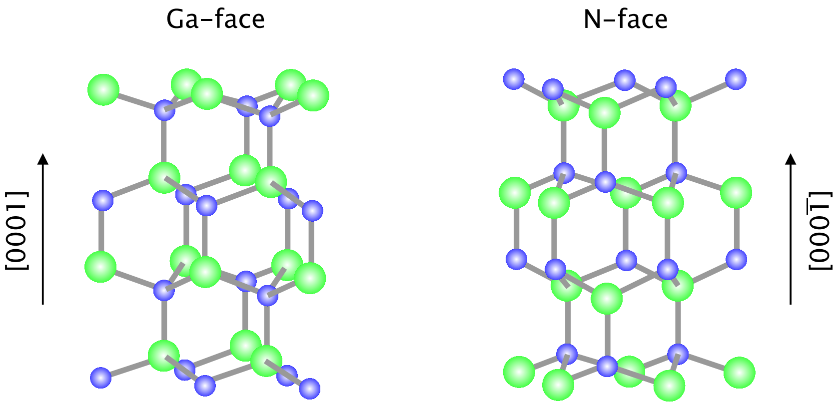

Figure 2.5: Different polarities (Ga- and N-faced) of wurtzite GaN. Ga(N) atoms are indicated with green(blue) spheres.

2.2 Polarization of hexagonal compound semiconductors

Tetrahedrally coordinated compound semiconductors which have hexagonal crystal structure can be described by the edge length a_0 of the basal hexagon and the height c_0 of the hexagonal prism. Usually an internal parameter u defined as the anion-cation bond lenght along the c-axis is given too (Fig. 2.4(b)). These crystals are composed by a stacking sequence of atomic bilayers consisting of two closely spaced hexagonal layers ortogonal to the c-axis, one with cations and the other with anions. Crystal surfaces which are perpendicular to the c-axis have either a cation polarity (designated (0001)) or an anion polarity (designated (000$\bar{1}$)) due to the lack of an inversion plane ortogonal to the c-direction. In the case of wurtzitic GaN a basal surface should be either Ga- or N-face: Ga(N)-face conventionally means Ga(N) on the top position of the bilayer, corresponding to [0001]([000$\bar{1}$]) polarity (Fig. 2.5) [Amb98]. The polarity of the semiconductor film depends on the choice of the substrate used for the growth.

Hexagonal compound semiconductors belong to the family of *pyroelectric* crystals because they exhibit at equilibrium a bulk electrical polarization called **spontaneous polarization** which is described by the vector $\vec{P}_{sp}$ ([C/m^2]) [Nye57]. The spontaneous polarization $\vec{P}_{sp}$ has to be distinguished from the **induced polarization** $\vec{P}_{in}$ and the **piezoelectric polarization** $\vec{P}_{pe}$, which arise in a dielectric material if an external electric field $\vec{E}$ or a stress defined by a second-rank tensor $\overline{\overline{\sigma}} = \sigma_{ij}$ (i, j = x, y, z) is

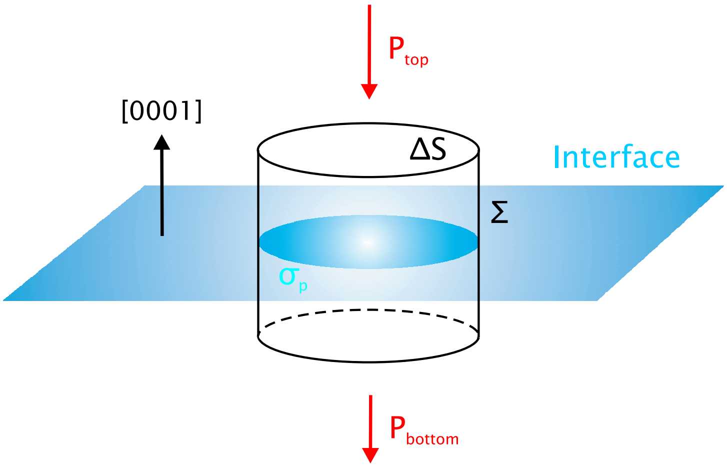

Figure 2.6: Scheme for the evaluation of the fixed polarization charge σ_P at the interface of a pyroelectric semiconductor heterostructure.

applied, respectively. In the absence of induced polarization $\vec{P}_{in}$, the **total polarization** $\vec{P}$ of a dielectric material is given by the sum of the spontaneous $\vec{P}_{sp}$ and piezoelectric $\vec{P}_{pe}$ polarization:

$$\vec{P} = \vec{P}_{sp} + \vec{P}_{pe} \tag{2.2}$$

The direction of the spontaneous polarization $\vec{P}_{sp}$ is determined by the polarity of the material. The direction of the piezoelectric polarization $\vec{P}_{pe}$ depends on the polarity and on wheter the material is under compressive or tensile stress.
In zincblende compound semiconductors the sum of the microscopic dipoles results in zero spontaneous polarization, while in wurtzite compound semiconductors the crystal symmetry is the highest compatible with the existence of spontaneous polarization (Fig. 2.4).

A bulk polarization charge density ρ_P is associated with the divergence of the total polarization $\vec{P}$:

$$\rho_p = -\nabla \cdot \vec{P} \tag{2.3}$$

In the case of pyroelectric semiconductor heterostructures grown along the c-direction the discontinuity of the total polarization $\vec{P}$ at the interface generates a fixed surface polarization charge density σ_P which can be calculated through the divergence theorem from the bulk polarization charge density ρ_P:

$$\begin{aligned}\int_V \rho_P dv &= -\int_V \nabla \cdot \vec{P} dv = -\int_\Sigma \vec{P} \cdot d\sigma \hat{n} = \\ &= \left(-P_{top} + P_{bottom}\right) \Delta S = \sigma_P \Delta S \end{aligned} \tag{2.4}$$

where the integration cylindrical volume V is enclosed by the lateral surface Σ and the bottom/top surfaces ΔS below and above the interface between the two different materials (Fig. 2.6).

The surface polarization charge σ_P plays a key-role for the physical properties of hexagonal-SiC and nitride heterostructures. To give an example of the possible influence of polarization on the properties of nitride-based devices, we consider the *Quantum Well* (QW) heterostructure of Fig. 2.7: $(20\text{ nm})\ \mathrm{Al_{0.15}Ga_{0.85}N}/(10\text{ nm})\ \mathrm{GaN}/(20\text{ nm})\ \mathrm{Al_{0.15}Ga_{0.85}N}$. The spontaneous $\vec{P}_{sp}$ and the piezoelectric $\vec{P}_{pe}$ polarization amount to -0.029 and 0.0025 C/m^2, respectively, and the interface polarization charge density σ_P at the GaN QW walls is ± 0.0025 C/m^2 [Amb98]. The electric field $\vec{E}$ in the GaN embedded film can reach a strength of 3×10^6 V cm^{-1}. The modification of the band edges due to spontaneous and piezoelectric electric fields inside the GaN QW has a significant influence on the optical properties. Due to the *Stark effect*[1], the effective band gap energy of GaN QW will be red-shifted and the recombination probability of electron-hole pairs will be decreased because of the spatial separation of electron and hole wave functions.

2.3 Non-polar SiC surfaces

In this section the SiC *polytypism* is introduced and the presentation is focused on the 6H-SiC polytype because it is used as a substrate for GaN growth, due to low lattice and thermal mismatch between the two materials and the excellent electrical properties of the substrate. 6H-SiC is a wide indirect bandgap semiconductor suited for high temperature and high-power/high-frequency electronic devices. The non-polar $(11\bar{2}0)$ (a-plane) and $(1\bar{1}00)$ (m-plane) 6H-SiC surfaces are nowadays particularly

---

[1] The *Stark effect* is the shifting and splitting of energy levels of atoms and molecules due to the presence of an external static electric field. The amount of splitting and or shifting is called the Stark splitting or Stark shift [Sta14].

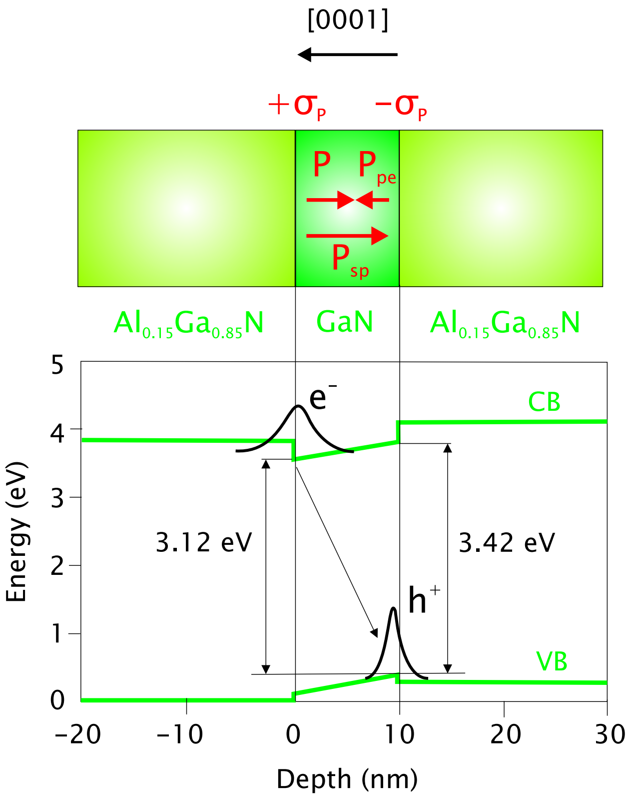

Figure 2.7: Conduction and valence band edges of a pseudomorphic grown $\mathrm{Al_xGa_{1-x}N/GaN/Al_xGa_{1-x}N}$ (x=0.15) heterostructure. The arrow indicates schematically the radiative recombination of an electron and a hole, which is red shifted in comparison to the bandgap energy due to the *Stark effect* (from [Amb98]).

attractive in view of novel microelectronic applications. Improved performances are demonstrated when compared with traditional SiC(0001)-based devices [YHKM00].

2.3.1 SiC crystal growth and polytypism

SiC is the only compound of Si and C existing in nature in the solid state at normal conditions. It is difficult to find this compound in natural reposits and SiC fractions are present only in stellar outflows. H. Moissan was the first scientist to observe SiC crystals in 1893 in fragments of a meteorite found in Meteor Crater near Diablo Canyon in Arizona (USA). In 1905, this mineral was named *Moissanite*, in his honor. In the same years E. Ache-

son developed an industrial process to sinter polycrystalline SiC: pure silica sand and finely divided carbon (coke) were reacted in an electric furnace at temperatures in the range of 2200-2480 °C and the product of reaction was named *carborundum*, a hard compound (9 in the Mohs scale) which showed superior abrasive properties.
The biggest problem to overcome for the production of SiC monocrystals is that a melt of SiC exists only at high temperature (T>3200 °C) and pressure (p>10^5 bar). The first breakthrough was done in 1955 by J. A. Lely who developed a method in which synthesized SiC powder was evaporated at high temperature (T=2500 °C) in Ar atmosphere (p=100 mbar) inside a graphite crucible under highest-purity conditions (**Physical Vapor Transport** or PVT method). The powder sublimed on a porous graphite wall inside the crucible forming hexagonal SiC monocrystal platelets characterized by low defect and *micropipe*[2] densities and random size of few mm. The biggest drawback of this method is that the nucleation of the material is difficult to control [Lel55].
In 1978 Y. M. Tairov and V. F. Tsvetkov improved the method of Lely by introducing at one side of the graphite crucible a SiC seed on which the growth of the SiC monocrystal took place (so called **modified Lely method**). The growth proceeded at similar Ar flow (p=100 Torr) and lower temperature (T=1500-2600 °C) in comparison with the original PVT method and SiC ingots with size of some mm were produced. The micropipe density was in the range of 10^2-10^3 cm^{-2} [TT78].
In the following years the scientific and industrial research focused on the production of cm-large SiC monocrystals trying to reduce the micropipe density of the material. Since 2007 four inch n-type 4H-SiC substrates with *Zero Micropipe Density* (ZMD-SiC substrates, CREE Inc.) are available on the market and new perspectives have arised for industrial applications of SiC in micro-electronic devices.

SiC crystallizes in numerous (over 200) slightly different crystalline phases that exhibit a one-dimensional polymorphism called **polytypism**: in all polytypes the tetrahedral bonding is preserved; what distinguishes one polytype from another is the stacking sequence of Si-C bilayers along a direction (Fig. 2.8). The two basic ways to create a close-paked stacking of Si-C bilayers are the cubic zincblende (β) and hexagonal wurtzite (α) crystal: the zincblende stacking sequence (ABCABC...) results if the Si-C

---

[2] Micropipes are small tubular voids that run parallel to the growth direction of the SiC crystal and can reach a radius-size of some μm. Their presence has for a long time hindered the massive use of SiC as base material for micro-electronic applications.

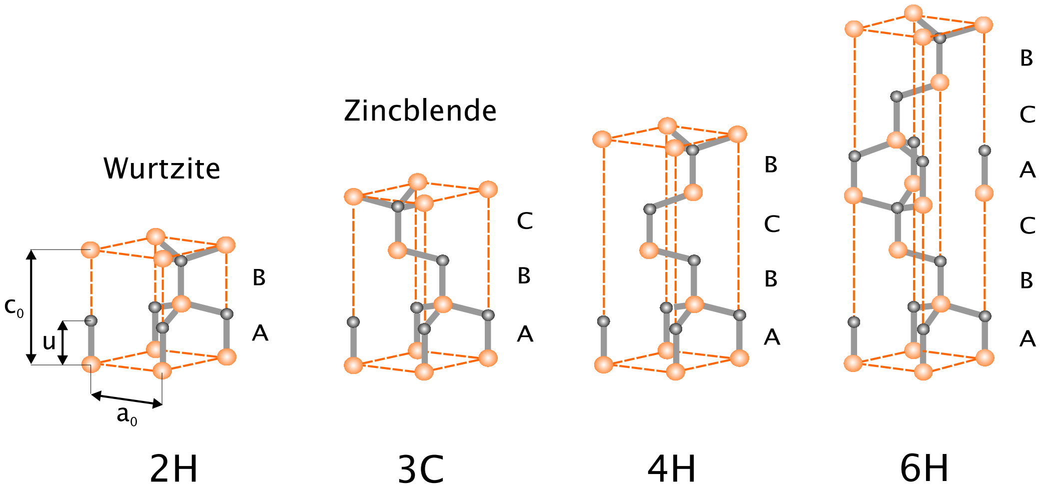

Figure 2.8: Bulk unit cells for the most common SiC polytypes. Si (C) atoms are indicated with yellow (black) spheres. The values of the lattice constants a_0 and c_0 for different polytypes are listed in Table 2.1.

bonds in every bilayer are rotated of 60° around the c-axis compared to the Si-C bonds of the previous bilayer (Fig. 2.9(a)) and the corresponding bulk unit-cell spans 3 bilayers (3C-SiC). The wurtzite stacking (ABAB...), instead, arises if the Si-C bonds in each bilayer are mirror images to the (0001) plane of the Si-C bonds in the previous bilayer (Fig. 2.9(b)) and the related bulk unit-cell spans 2 bilayers (2H-SiC).

Many other polytypes are some mixture of the fundamental zincblende and wurtzite lattice structures. The bulk unit-cell of the 4H-SiC polytype spans 4 bilayers, 2 of which are “quasi-hexagonal”, that means with opposite stacking orientation with respect to the previous bilayer (50% hexagonality). In the 6H-SiC case, the corresponding bulk unit cell spans 6 bilayers, 2 of which are “quasi-hexagonal” (30% hexagonality). In summary to the 3C, 6H, 4H and 2H-SiC polytypes can be associated an increasing “hexagonality” of 0%, 30%, 50% and 100%, respectively, and some physical properties of SiC depend strongly on the hexagonal character of the polytype. For example, the greater the wurtzite component, the larger the bandgap, ranging at room temperature from 2.4 eV, 3.0 eV, 3.2 eV to 3.3 eV for 3C-SiC, 6H-SiC, 4H-SiC and 2H-SiC, respectively [Iof].

Further more complex structures showing long periodicity with rhombohedral symmentry are known for SiC, such as 15R and 21R, but the only interesting polytypes for industrial applications are the 3C-, 4H- and 6H-SiC.

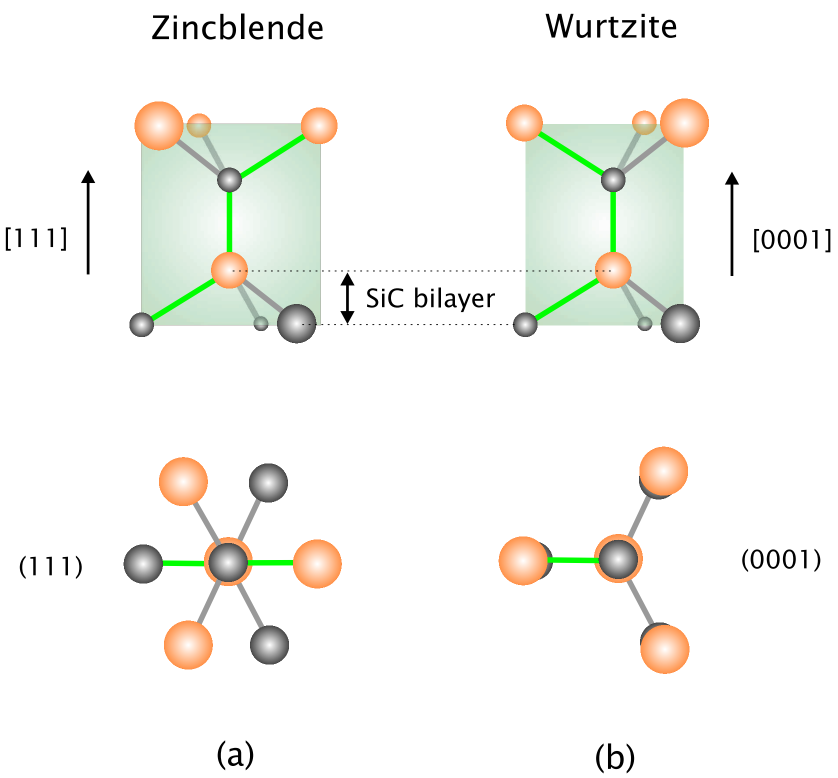

Figure 2.9: Upper image (Lower image): Side (Top) view of (a) zincblende and (b) wurtzite bonding between Si and C atoms in adjacent planes. The three tetrahedral bonds are $60°$ rotated along the [111] direction in the zincblende case and mirror images to the (0001) plane in the wurtzite case. Si (C) atoms are indicated with yellow (black) spheres.

2.3.2 SiC properties and applications

The Si-C bond has a length of 1.87 Å [Rig03] and a formation energy of 2.7 eV per formula unit [CGGP98] (Table 2.1). Both C- and Si-atoms belong to the fourth group of the periodic table, but the Si-C bond is strongly ionic due to the high difference in covalent radius (r_C=0.76 Å, r_{Si}=1.11 Å [Cen]) and electronegativity (X_C=2.55 and X_{Si}=1.90 in the Pauling scale [Pau32]). In the Garcia-Cohen ionicity scale [GC93] the antysimmetric coefficient g for 3C-SiC is g=0.475 (the scale goes from g=0 for the fully covalent Si-Si bond to g=0.986 for the completely ionic KCl bond). Therefore, Si-atoms act as cations while C-atoms act as anions in SiC. The core-size difference between C- and Si-atoms results in an asymmetric electronic charge distribution about the midpoint of the Si-C bond: for the 3C-

	AlN	**GaN**	**InN**	**6H-SiC**	**GaAs**	**Si**
lattice constant a_0 [Å]	3.112	3.189	3.54	3.044^a	5.65	5.43
lattice constant c_0 [Å]	4.982	5.186	5.705	14.95^a	-	-
internal parameter u	0.380	0.376	0.377	$1.865\ ^a$	-	-
energy gap E_g [eV]	6.2	3.39	0.7^b	3.1	1.43	1.1
dielectric constant ϵ_r	8.5	8.9	15.3	9.6	12.5	11.8
electron mobility (cm^2/Vs)	300	440	70-250	<400	8500^c	1350
breakdown field (MV/cm)	1.2-1.8	5^c	2.4^c	0.4^c	0.3^c	
saturation electron drift velocity (10^7cm/s)	14^d	27^c	25^e	20^c	20^c	10^c
thermal conductivity (W/cm)	2.8	1.3	1.8	4.9	0.5	1.3
spontaneous polarization (C/m^2)	-0.081^f	-0.029^f	-0.032^f	-0.015^g		
Knoop hardness (kg/mm^2)	800	1200-1700		2900-3100	750	1150
bond energy per formula unit (eV)	2.88^h	2.17^h	1.93^h	2.70^i		

Table 2.1: Material parameters at RT for group-III nitrides, 6H-SiC and other semiconductors of interest. All the data are from [Iof]. References (a), (b), (c), (d), (e), (f), (g), (h) and (i) are [RPB$^+$02], [DKE$^+$02], [MSG$^+$94], [OFS$^+$98b], [OFS$^+$98a], [BFV97], [BCB$^+$07], [NN96] and [CGGP98], respectively.

SiC polytype the bond charge maximum between anion and cation is only 20% of the bond length away from the anion (C-atom) [SKP95].

SiC is a chemically inert material and of high hardness. While all SiC modifications have quite the same mechanical and thermal properties, their electrical and optical properties differ greatly from polytype to polytype.
In this work we focus our attention on the 6H-SiC polytype which is one of the most used substrates for GaN growth due to the low lattice mismatch (3.5%) and the outstanding electrical properties of the two materials. Most of the 6H-SiC crystals are optically transparent and show a high refractive index. Doped crystals are colored because of specific optical absorption caused by the dopants (Fig. 2.10). Normally n-type (p-type) 6H-SiC is prepared by doping with nitrogen (aluminum) while vanadium can be used to

Figure 2.10: 6H-SiC two inches wafers with different dopings (from [Bic]).

prepare crystals with semi-insulating properties.

The **wide bandgap energy** allows 6H-SiC based devices to operate at extremely high temperatures. Semiconductor devices work in the temperature range where the intrinsic carrier concentration is neglibile and the transport properties are determined by the dopant impurities. Since the number of intrinsic carriers increases exponentially with the temperature, Si-based devices can not operate at temperature higher than T=300 °C, while 6H-SiC-based devices are theoretically predicted to withstand temperaures over 800 °C. 6H-SiC-based *Junction Field Effect Transistors* (JFETs) operating at T=500 °C have been demonstrated in 2008 [NSC$^+$08]. SiC electronics and sensors that could operate in hot engines and environments could be useful for the aircraft industry where reduction of the weight of cooling systems for IC devices plays a key role.

The strong Si-C bond yields high-frequency lattice vibrations and high-energy phonons (>100 meV [Iof]). This property is responsible for the **high thermal conductivity** and the **high breakdown electric field** that allow SiC devices to reach high power densities. The high thermal conductivity, which at room temperature is higher than that of any metal, enables 6H-SiC devices to easily dissipate the heat generated during operation and the cooling hardware typically needed to keep high-power devices from

overheating can be made much smaller or can even be eliminated.
The high breakdown electric field allows the fabrication of high-voltage Schottky rectifiers and *Metal Oxide Semiconductor Field Effect Transistors* (MOSFETs) with low specific on-resistance.
Finally 6H-SiC is widely used as a substrate for nitride growth to produce blue-green *Light Emitting Diodes* (LEDs) and *Laser Diodes* (LDs). The high thermal conductivity of the SiC substrates allows an efficient dissipation of the electrical power during device operation and therefore increases the device lifetime.

2.3.3 Atomic and electronic structure of non-polar SiC surfaces

The interest in non-polar SiC surfaces has grown in the last ten years because of improved physical properties in comparison with the polar surface (0001) of the same SiC polytypes. For instance, it has been shown that the problem of low channel mobility along the c-axis in 6H-SiC MOSFETs fabricated on the conventional (0001) Si-face can be overcome employing the $(11\bar{2}0)$ plane [YHKM00]. Moreover, as discussed in Sec. 2.2, electrons and holes tend to be separated and the *Quantum Efficiency*[3] (QE) of their radiative recombination probability is reduced. This drawback is avoided if the nitride film is grown on a non-polar surface: in fact *Quantum Dots* (QDs) embedded in AlN grown on 6H-SiC$(11\bar{2}0)$ show a larger *Photoluminescence* (PL) intensity, a much smaller polarization induced energy shift with $(11\bar{2}0)$ QDs size and a reduced PL linewidth than QDs grown along the (0001) direction [FRBA+05]. In view of these novel applications the detailed description of the atomic and electronic structure of non-polar SiC surfaces plays a key role.
In the following, the main published experimental and theoretical results on non-polar SiC surfaces are reviewed. Upon truncation of SiC bulk material, generally the Si-atoms move inward and the C-atoms move outward from the exposed surface. The reason is a charge transfer: the Si dangling bond, which has a high energy, emits charge to the lower lying C dangling bond. The surface cation which has lost an electron favours a more planar sp^2-like hybridization, while the surface anion moves outward in a p^3 configuration [RDH01].

---

[3] The *Quantum Efficiency* of a QW heterostructure is defined as the fraction of electron-hole pairs which give rise to radioactive recombination on the total number of electron-hole pairs generated in the QW.

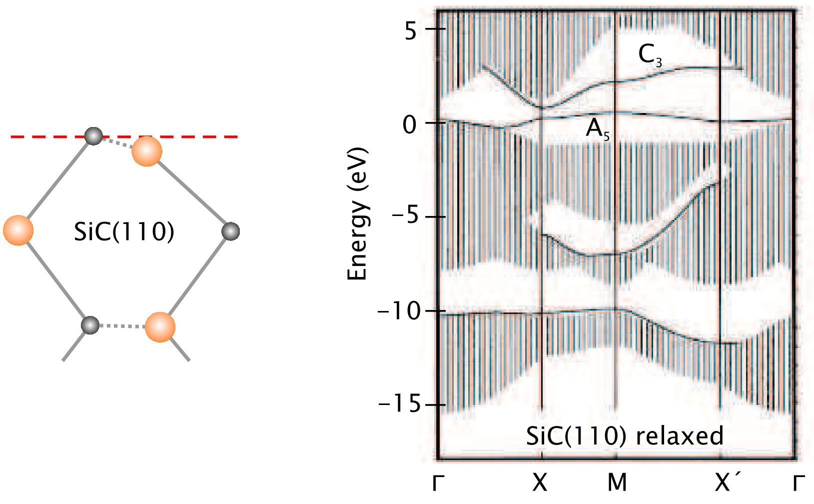

(a)

(b)

Figure 2.11: (a) Side view of the relaxed SiC(110) surface. The ideal surface plane is indicated by a dashed red line. Bonds that form an angle with the drawing plane are shown by dotted lines. Bonds that lie in or are parallel to the drawing plane are shown by full lines. Yellow(black) spheres show Si(C) atoms. (b) Bands of localized surface states of the relaxed SiC(110) surface together with the projected bulk band structure (from [SKP95]).

The **3C-SiC(110) surface** has been the first non-polar SiC surface to be theoretically investigated and compared with the non-polar GaAs(110) surface which is the cleavage plane of GaAs. The *ab-initio* calculated SiC(110) surface structure shows a relaxation in which the C-atoms only move parallel to the surface while the Si-atoms relax parallel and perpendicular to the surface. The latter move down by 0.25 Å towards the substrate (Fig. 2.11(a), [SKP95]). The relaxation of the atoms in the underlying lattice layers is very small. The less electronegative cations reside closer to the substrate than the more electronegative anions because the kinetic energy of the valence electrons and their Coulomb repulsion energy is minimized when the more strongly charged surface layer ion resides as high as possible above all other atoms. The more electronegative surface ions (C) are thus positioned above the plane of the less electronegative surface ions (Si).

As far as the surface electronic structure is concerned, the *ab-initio* calculations show a number of salient bands of localized surface states inside the projection of the bulk energy gap both at the ideal and relaxed surfaces:

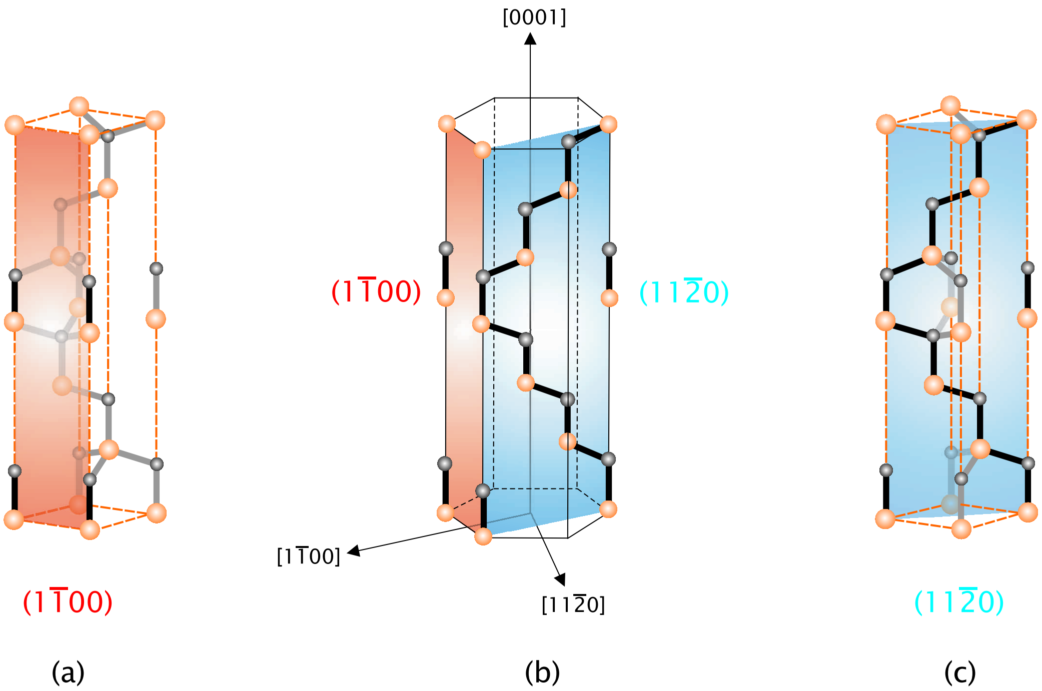

Figure 2.12: (a) Bulk unit cell of 6H-SiC with the non-polar 6H-SiC$(1\bar{1}00)$ surface (m-plane) highlighted in red. (b) Hexagonal crystal cell of the 6H-SiC polytype with with the non-polar 6H-SiC$(1\bar{1}00)$ (6H-SiC$(11\bar{2}0)$) surface highlighted in red (blue). (c) Bulk unit cell of 6H-SiC with the non-polar 6H-SiC$(11\bar{2}0)$ surface (a-plane) highlighted in blue. Yellow (black) spheres indicate Si (C) atoms. The Si-C bonds which lie on the non-polar surfaces are indicated with brighter color.

the relaxed surface is semiconducting and the surface energy gap is delimited by an occupied C-like surface band (A_5) arising above the *Valence Band Maximum* (VBM) and an empty Si-like surface band (C_3) arising below the *Conduction Band Minimum* (CBM) at the border of the *Brillouin Zone* (BZ) (Fig. 2.11(b)).

In 2001 E. Rauls *et al.* published results of theoretical calculations on non-polar surfaces of the 4H-SiC and 6H-SiC polytypes [RDH01]. Defining a surface roughness r as $\Delta r = z_{max} - z_{min}$, where z is the position of the surface atoms along the surface normal, the authors found that the relaxed **4H-SiC(1$\bar{1}$00)** surface shows a much higher corrugation ($\Delta r = 1.67$ Å) than the relaxed **4H-SiC(11$\bar{2}$0)** one ($\Delta r = 0.36$ Å). In the first case the clean surface results to be metallic, while in the second case semicon-

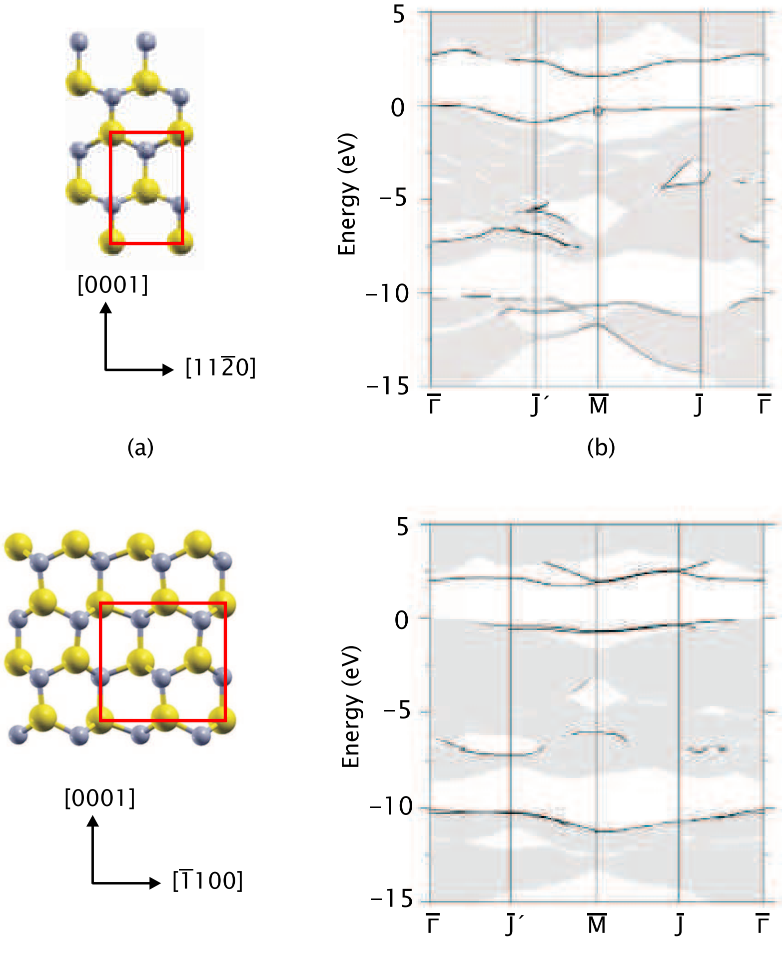

(a) (b)

(c) (d)

Figure 2.13: (a) Top view of the relaxed 2H-SiC(1$\bar{1}$00) and (c) 2H-SiC(11$\bar{2}$0) surface. Yellow (black) spheres show Si (C) atoms. The rectangular zone sketched in red color identifies the surface unit cell. Surface band structure of the relaxed (b) 2H-SiC($1\bar{1}00$) and (d) 2H-SiC($11\bar{2}0$) surface. The shaded area shows the projected bulk band structure, and the solid line are the surface states (from [BCB$^+$07]).

ducting. The **6H-SiC(1$\bar{1}$00)** surface relaxation is characterized by a surface roughness of $\Delta r = 2.57$ Å and displays metallic properties. The **6H-SiC(11$\bar{2}$0)** surface is significantly smoother ($\Delta r = 0.35$ Å) and semiconducting. The non-polar 6H-SiC(1$\bar{1}$00) and the 6H-SiC(11$\bar{2}$0) surfaces are shown in Fig. 2.12. The latter one is object of investigation in this work.

In 2007 G. P. Brandino *et al.* published first-principles density functional calculations on non-polar low-index surfaces of hexagonal SiC and in particular of 2H-SiC [BCB$^+$07]. The authors showed that the **2H-SiC(1$\bar{1}$00)** surface (m-plane) simply relaxes with Si-C surface bonds tilted by $\approx 5.2^\circ$ and the Si (C) surface-atoms moving inward by -0.26 Å (-0.10 Å). The lateral positions of the surface atoms in the top-layer (1$\bar{1}$00) plane are almost unchanged (Fig. 2.13(a)). Regarding the electronic structure two surface states in the band gap are present, one occupied and another empty (Fig. 2.13(b)). The charge density at the surface is mainly localized on the surface Si-C bond, with charge transfer from Si to C, which strengthens the surface bond. This behavior is consistent with the observed relaxation mechanism where the “depleted” Si moves inside the surface, leaving C as the outermost atom.
Also in the case of the **2H-SiC(11$\bar{2}$0)** surface (a-plane) the relaxation involves mainly the outermost layer, with the outermost Si-C bonds tilted by $\approx 5.9^\circ$ and contracted by $-7.9\,\%$. The lateral positions of the surface atoms in the top-layer (11$\bar{2}$0) plane are almost unchanged (Fig. 2.13(c)). The band structure shows the presence of four states, two fully occupied and two empty, each twice degenerate in energy, localized on surface C- and Si-atoms, respectively. (Fig. 2.13 (d)).

J. Pollmann *et al.* presented in 1997 a review about experimental results on non-polar SiC surfaces, but a complete experimental characterization of these surfaces is still missing [PKS97]. In the last ten years a big effort has been done to understand the properties of non-polar SiC surfaces, but to our knowledge until the publication in 2007 of the results presented in this work [BHW$^+$07], no experimental data on the clean 6H-SiC(11$\bar{2}$0) surface were available. For the H-terminated 4H-SiC(1$\bar{1}$00) and 4H-SiC(11$\bar{2}$0) surfaces *X-ray Photoelectron Spectroscopy* (XPS), *Synchrotron X-ray Photoelectron Spectroscopy* (SXPS), *Low-Energy Electron Diffraction* (LEED) data were already to hand [SGS$^+$05].

2.4 Non-polar GaN surfaces

This section presents the *Hydride Vapor Phase Epitaxy* (HVPE) method that is nowadays used to grow thick free-standing GaN layers along the [0001] direction. Cleavage of GaN films under UHV conditions results in the exposure either of $(1\bar{1}00)$ or $(11\bar{2}0)$ clean surfaces which can be investigated by X-STM/STS. As already mentioned, the non-polar GaN surfaces are most relevant in view of improved emission efficiency of blue LEDs and LDs. An introduction to the atomic and electronic structure of non-polar GaN surfaces is given below.

2.4.1 GaN substrates grown by Hydride Vapor Phase Epitaxy

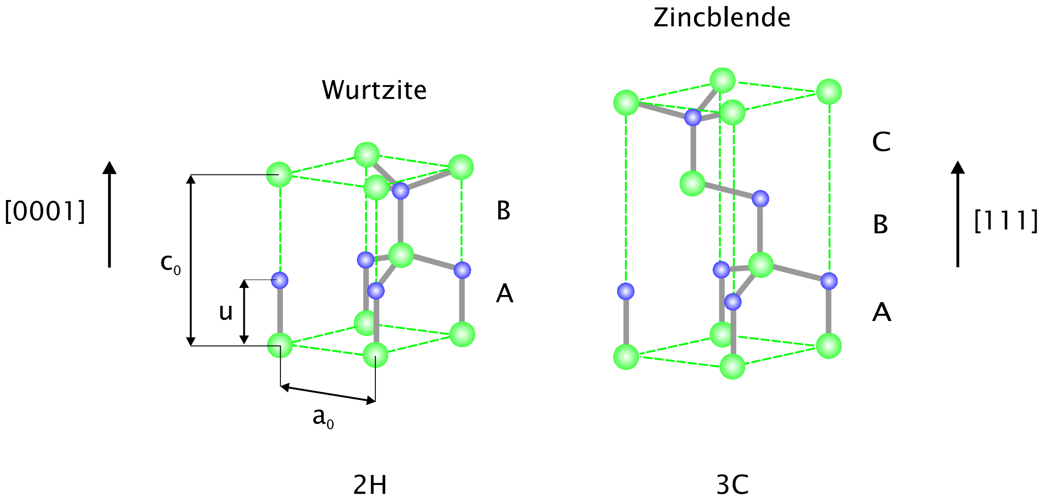

Figure 2.14: Bulk unit cell for the wurtzite (left) and zincblende (right) GaN polytype. Ga (N) atoms are indicated with green (blue) spheres. The values of the lattice constants a_0 and c_0 of the wurtzite polytype are given in Table 2.3.

GaN crystals exist in the wurtzite (α) or zincblende (β) allotropic modification (Fig. 2.14). The transformation of one GaN polytype into the other depends on the stacking sequence of the atomic GaN bilayers along the [111] direction:

$$(\alpha)\ \text{ABAB...} \leftrightarrow (\beta)\ \text{ABCABC...}$$

The two structures differ only in the position of the third near neighbors and further ones. The thermodinamically stable modification of GaN is

	SiC	**Al_2O_3**	**Si**
Advantages of the substrate	-low lattice mismatch to GaN -conductive -high thermal conductivity	-widely available -high stability at high temperatures -easy to clean -quite cheap	-cheap -widely available -possibility of integration with Si microelectronics -available in conductive and insulating forms
Disadvantages of the substrate	-expensive	-high lattice mismatch to GaN -insulating -low thermal conductivity	-high lattice mismatch to GaN -high thermal mismatch to GaN

Table 2.2: Road-map for the choice of substrate for nitride growth.

the wurtzite phase. The calculated wurtzite-zincblende structural energy difference per atom is $\Delta E_{\alpha\rightarrow\beta} = E_\alpha - E_\beta = -9.9\ \mathrm{meV}$ at T=0 K [YLFZ92]. We will therefore address our attention to the stable wurzite modification of GaN which is the one employed to fabricate microelectronic devices.

GaN crystals do not exist in nature because of the high melting point of the material (T=2791 K [Edg94]). Artificial GaN samples can be synthesized only under very high nitrogen pressure (p=20 kbar) and high temperature (T=1500-1800 K) in the form of platelets or rod-like crystals. The GaN platelets have the shape of elongated hexagons and crystallize with a wurtzite structure [Por96].
Until recent years the difficulties in bulk GaN growth have addressed the scientific and industrial research to the growth of GaN films on substrates of different materials (*heteroepitaxy*). To be suited for the growth of GaN epilayers, a substrate should generally satisfy the following requirements:
1) be available in a minimum size of two inch, in large quantities and at an acceptable price.
2) have physical properties similar to the GaN epilayer in order to reduce the density of defects propagating from the interface between the substrate and the epilayer towards the top of the structure.
3) exhibit atomic flat surfaces.
4) be stable under the influence of nitrogen radicals in the temperature-range T=800-1100 °C in which GaN films are usually grown.

The more common substrates for GaN growth are 6H-SiC and Al_2O_3 (sapphire), but also Si(111) is getting more and more important everyday in view of a possible integration between nitride and silicon technologies. The

	GaN	**6H-SiC**	**Al_2O_3**	**Si**
lattice parameter $a_0(100)$ (Å)	3.189	3.08	4.73	5.43
lattice parameter $a_0(111)$ (Å)			2.679	3.84
lattice parameter c_0 (Å)	5.186	15.12	12.99	
thermal conductivity λ (W/cmK)	1.3	3.0-3.8	0.5	1-1.5
thermal expansion coeff. $\alpha_{\|\|}(10^{-6}K^{-1})$	5.59	4.2	7.5	2.59
lattice mismatch GaN/substrate $(a_0^{GaN}(100)$- $a_0^{sub})/a_0^{sub}$	-	+3.5%	+16%	-20%
thermal mismatch GaN/substrate $(\alpha_{\|\|}^{GaN}(100)$- $\alpha_{\|\|}^{sub})/\alpha_{\|\|}^{sub}$	-	+25%	-34%	+54%

Table 2.3: Lattice and thermal mismatch of GaN with 6H-SiC, Al_2O_3 and Si(111) (from [KD02]).

choice of the substrate depends on some criteria which are schematically illustrated in Table 2.2. One key point for the growth of good crystal quality GaN epilayers is the lattice and thermal mismatch between GaN and substrate (Table 2.3).

Several techniques are used to grow GaN films and we will present here a brief overview on the most common of them. For a more detailed description see *e. g.* ref. [LE02].
In *Molecular Beam Epitaxy* (MBE), thin films crystallize via reactions between thermal-energy molecular or atomic beams of the constituent elements and a heated substrate surface (T≈800 °C) which is mantained at the required temperature in UHV. The composition of the grown epilayer and its doping level depend on the relative arrival rates of the constituent elements and dopants, which in turn depend on the evaporation rates of the appropriate sources. The typical growth rate of 4-5 nm/min is low enough that surface migration of the impinging species on the growing surface is ensured, consequently the surface of the grown film is very smooth. A peculiar property which distinguishes MBE from other deposition techniques is its significantly more precise control of the beam fluxes and growth conditions. Because of vacuum deposition, MBE growth is carried out under conditions far from thermodynamic equilibrium and is governed mainly by the kinetics of the surface process occurring when the impinging beams react with the outermost atomic layers of the substrate crystal. Being realized in UHV environment, MBE may be controlled in situ by surface sensitive diagnostic methods such as *Reflection High Energy Electron Diffraction* (RHEED), *Auger Electron Spectroscopy* (AES) or ellipsometry, which is an important issue *e. g.* for the development of new processes.

In *Metal Organic Chemical Vapor Deposition* (MOCVD) organometallic precursors, hydrides for the nitrogen source (N_xH_y) and transport gases are mixed together and react with a heated substrate surface ($T \approx 1100\ ^\circ$) on which the precursors are pyrolyzed and the nitride film is deposited. The underlying chemical mechanism is complex, involving a combination of gas phase and surface reactions and still remain poorly characterized. This technique has the advantage of large area growth capability, good conformal step coverage and precise control of epitaxial deposition.

Hydride Vapor Phase Epitaxy (HVPE) is a techique which meets both the requirements of high growth rate and good crystal quality. It is was applied for the first time to GaN growth in 1969 by H. P. Maruska and J. J. Titien [MT69]. In this process, gallium monochloride is synthesized upstream in a reactor by mixing HCl gas with liquid Ga metal at T=800-900 °C:

$$2\mathrm{Ga(l)}+2\mathrm{HCl(g)}\leftrightarrow 2\mathrm{GaCl(g)}+\mathrm{H_2(g)}$$

The GaCl is transported to the substrate where it reacts at T=1000-1100 °C with NH_3 to form GaN, via the reaction:

$$\mathrm{GaCl(g)}+\mathrm{NH_3(g)}\leftrightarrow \mathrm{GaN(s)}+\mathrm{HCl(g)}+\mathrm{H_2(g)}$$

Sapphire is the substrate normally used for HVPE GaN growth with a typical growth rate of 100 μm/h. In this way it is possible to produce thick GaN layers (300-400 μm) with a diameter of 2-3 inches. The grown GaN layer is usually under stress because of the thermal and lattice mismatch between GaN and the substrate, but it possible to get a **free-standing GaN** wafer by removing the substrate with the *Laser Lift Off* (LLO) technique: the separation of the GaN layer is achieved by irradiation of the substrate-film-interface through the substrate with high power laser pulses at a wavelength which is transmitted by the substrate, but is strongly absorbed in the GaN layer. The absorption of such high intensity laser pulses causes a rapid thermal decomposition of the irradiated GaN interfacial layer into metallic Ga and gaseous N_2 and the substrate is removed [MKAS03].
The free-standing c-plane GaN wafers are known as *quasi*-substrates and can be used for subsequent *homoepitaxy* of GaN films. MOCVD GaN epilayers show improved crystal quality in PL measurements when grown on free-standing HVPE GaN substrates than on GaN templates on sapphire [MKAS99].

Due to novel applications of non-polar nitrides (see following section) scientists have focused their attention in the last five years to the growth of non-polar free-standing GaN substrates. B. A. Haskell *et al.* reported in 2005 on the growth of GaN($1\bar{1}00$) films on $(100)\gamma - \mathrm{LiAlO_2}$: the morphology achieved was smooth enough to allow the fabrication of m-plane GaN templates and free-standing substrates for non-polar device growth [HCW$^+$05]. Another possibility to get free standing m-plane GaN substrates is to grow c-plane GaN substrates and prepare the m-surface using a wire saw and slicing the thick GaN bulk crystal along the [0001] direction. This technique has recently been applied and the obtained free-standing m-plane GaN substrates show high crystalline quality and low defect density [FKM$^+$08].

2.4.2 GaN properties and applications

The Ga-N bond has a length of 1.94 Å and a binding energy of 2.17 eV per formula unit [NN96] (Table 2.1). The Ga-atom belongs to the third group and the N-atom to the fifth group of the periodic table. The Ga-N bond is strongly ionic due to the high difference in covalent radius ($\mathrm{r_N} = 0.71$ Å, $\mathrm{r_{Ga}} = 1.22$ Å [Cen]) and electronegativity ($X_N = 3.04$ and $X_{Ga} = 1.81$ in the Pauling scale [Pau32]). In the Garcia-Cohen ionicity scale the antysimmetric coefficient *g* for zincblende GaN is *g*=0.78 (the scale goes from *g*=0 for the fully covalent Si-Si bond to *g*=0.986 for the completely ionic KCl bond [GC93]). Therefore, Ga-atoms act as cations while N-atoms act as anions in GaN.

GaN is a **direct wide bandgap semiconductor** (E_g = 3.4 eV) which can be used for several microelectronic applications. Due to the wide bandgap, the high breakdown voltage and saturation velocity GaN can be used as a base material for high frequency/high power devices which are employed in communication systems, as *e. g. High Electron Mobility Transistors* (HEMTs). But the field in which GaN is massively used is solid state lighting: the mixture of GaN with In (InGaN) or Al (AlGaN) with an energy bandgap dependent on the In/Ga or Al/Ga ratios allows to fabricate LEDs with colors that go from the orange to the blue (Fig. 2.15). The large mismatch between GaN and InN (-10%) limits the applicability towards the red/IR part of the spectrum. Nowadays (2008) the time is almost reached when LED-lighting will start to replace the traditional bulb lighting thanks to the luminous efficiency of GaN blue LEDs. The advantages of LED lighting in comparison with traditional bulb lighting go from longer lifetimes (10^5 hours for LEDs compared to 10^3 hours for tungsten bulbs) and much higher energy

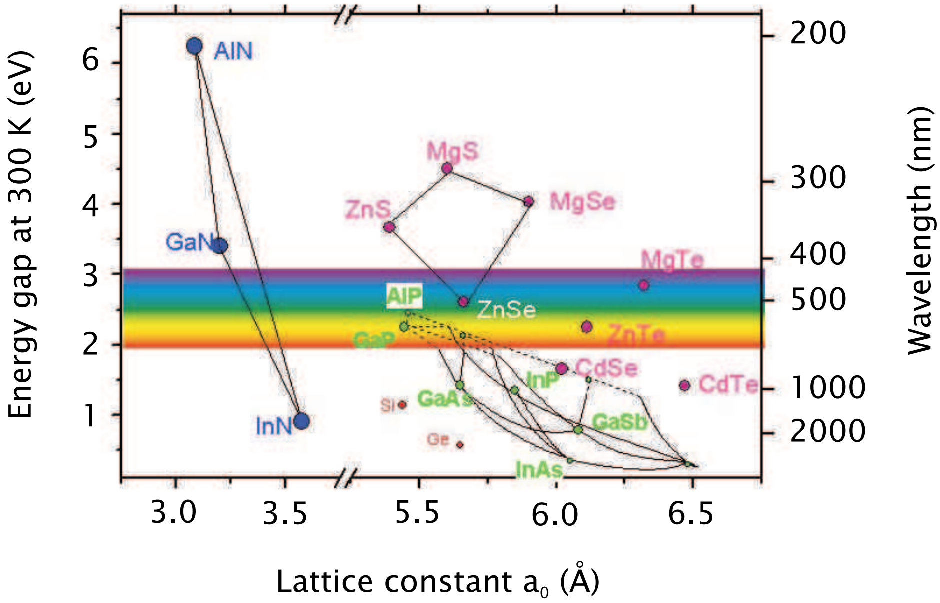

Figure 2.15: Bandgaps of the most important elementary and binary semiconductors versus their lattice parameter. For group III-nitrides the values for hexagonal polytypes are reported (from [fO]).

efficiency (a white LED can reach the same light brightness of a 60 W incandescent lamp with 90% less energy consumption [The]).
Furthermore blue GaN-based LDs started recently to be applied in the so called *Blu-ray disc* technology [VV] in which a “blue” (technically violet) laser operating at a wavelength of 405 nm is used to read and write data. Conventional *Digital Video Discs* (DVDs) and *Compact Discs* (CDs) operate with red and near infrared lasers at 650 nm and 780 nm, respectively. With the storage capacity being inversely proportional to the square of the laser wavelength used to store the data, a 12-cm diameter double side *Blu-ray* DVD can store 50 GB data while a traditional red laser DVD which can store only 8.5 GB.

The performance of conventional blue GaN LEDs and LDs grown along the c-axis has so far been limited by polarization fields parallel to the c-direction. The active region of nitride LEDs or LDs typically comprises InGaN QWs. Due to the presence of the internal electric fields, electrons and holes are pulled to opposite interfaces of the InGaN QWs and the spatial separation of their wave functions causes a decrease of the transition matrix element and suppresses radiative recombination with respect to nonradiative recombination, diminishing drastically the QE of the device (Stark

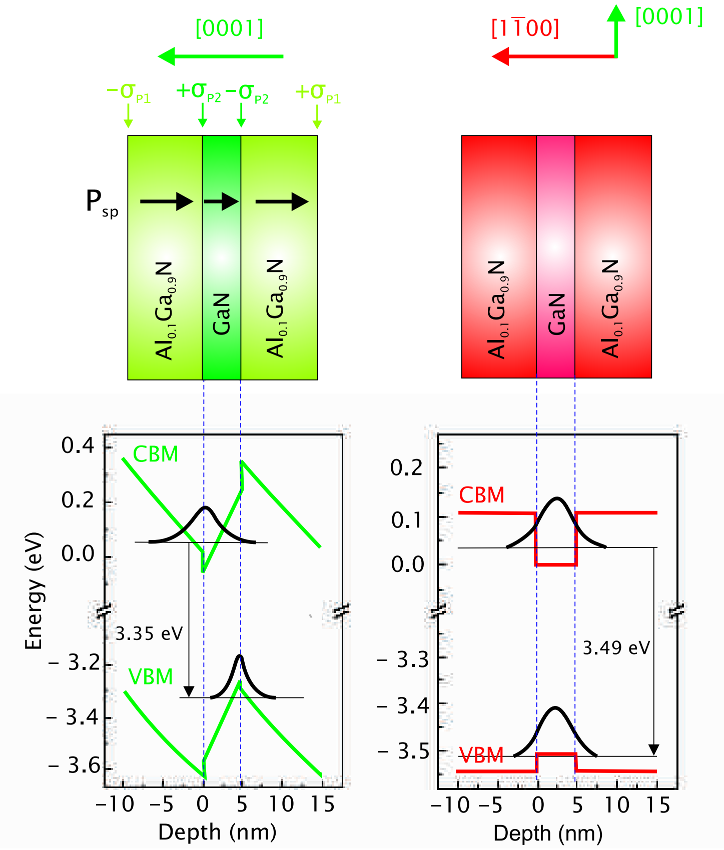

Figure 2.16: Calculated band profiles in 10 nm $Al_xGa_{1-x}N$/5 nm GaN/10 nm $Al_xGa_{1-x}N$ (x=0.1) QWs. (a) The very large electrostatic fields in the [0001] orientation result in a quantum confined Stark effect and poor electron–hole overlap. The surface polarization charge density on the *c*-plane at the heterostructure top/bottom surfaces and QW walls is indicated with σ_{P1} and σ_{P2}, respectively. (b) The [1$\bar{1}$00] orientation is free of electrostatic fields, thus true flat-band conditions are established (from [WBT+00]).

effect). Therefore the operation of conventional InGaN/GaN LDs is limited to wavelengths shorter than 482 nm and an undesired current-dependent red-shift in the emission is observed [SK07]. This is the reason for the so-called “green-gap” of nitride based LDs: blue-green and green LDs, which would be suitable for laser color displays, portable projectors, and as replacements for solid state and gas lasers, have not yet been realized. In InGaN QWs LDs working at 470 nm, the Stark effect reduces the optical transition probability down to 30% of its value without internal electrical

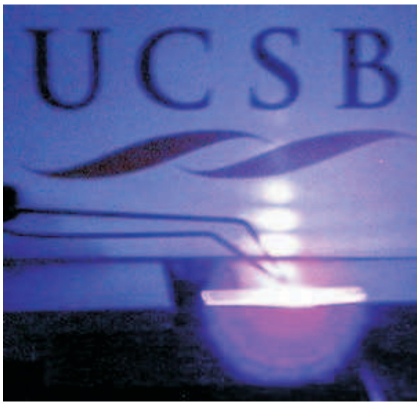

Figure 2.17: Far-field pattern of the world's first non-polar GaN blue-violet laser diode. The bright spots illustrate clear lasing modes (from UCSB Solid State Lighting and Display Center).

fields [KFK+08].

The QE of radiative recombination of electrons and holes in InGaN/GaN LEDs can be improved by growing the heterostructure parallel to a direction which is free from polarization fields. P. Waltereit *et al.* showed in 2000 that the growth of GaN/AlGaN multi QWs along a non-polar direction allows the fabrication of heterostructures free of electrostatic fields, resulting in an improved QE (Fig. 2.16, [WBT+00]). The authors succeded in growing non-polar $(1\bar{1}00)$ (5 nm)GaN/(10 nm)AlGaN multi QWs structures on tetragonal γ-LiAlO$_2$ and compared them to conventional (0001) GaN/AlGaN multi QWs structures grown on 6H-SiC(0001). *Cathodoluminescence* (CL) spectra at T=5 K show that the transition energy for the c-plane wells is 3.36 eV, whereas the m-plane wells emit at 3.48 eV, and time-resolved PL measurements at T=5 K reveal a much longer decay time for the c-plane ($\geq$ 6 ns) than for the m-plane (450 ps) wells. Both measurements are a clear demonstration of improvement by going from c-plane to m-plane grown heterostructures as far as optical emission is concerned.

Following the first experimental results by Waltereit *et al.* on non-polar GaN, the scientific research focused on non-polar nitride films with the aim of improving the efficiency of light emission.
In 2002 the group of M. D. Craven and co-workers at the University of Santa Barbara (California) succeded in growing the first planar high crystalline quality *Metal Organic Vapor Phase Epitaxy* (MOVPE) a-plane GaN layer on r-plane sapphire and a-plane SiC: the threading dislocation den-

sity present in these films was determined by plan-view *Transmission Electron Microscopy* (TEM) to be σ_d=2.6×10^{10} cm^{-2} [CLW$^+$02].
One year later (2003) the first planar non-polar Schottky diode based on a-plane GaN and r-plane sapphire was produced by MOVPE at the University of South Carolina [ACY$^+$03]. This opened up the possibility for fabricating non-polar electronic devices.
In april 2007 the group coordinated by S. Nakamura at the University of Santa Barbara presented an improved non-polar m-plane LED (Fig. 2.17) with a thick InGaN multi QWs structure grown by MOCVD on low extended defect bulk m-plane GaN substrate. The peak wavelength of the electroluminescence emission from the packaged LEDs was 402 nm, which is in the blue-violet region. The output power increased almost linearly and hardly showed a tendency of saturation, in contrast to conventional polar c-plane LEDs [KSS$^+$07].
In june 2008 K. Okamoto and co-workers reported on continuous-wave operation of blue-green LDs with a lasing wavelength of 481 nm based on nonpolar m-plane GaN [OTK08].
Therefore non-polar nitride heterostructures seem to be really promising and their applications are nowadays limited only by the small size of non-polar free standing GaN substrates [SK07]. As soon as two inch non-polar free standing GaN substrates will be available on the market, it is reasonable to believe that all the technology for green and blue LEDs/LDs will switch to non-polar films. In view of these applications the understanding of surface properties of non-polar III-N semiconductors plays a key role.

2.4.3 Atomic and electronic structure of non-polar GaN surfaces

Theoretical calculations of atomic and electronic properties of GaN are quite difficult to perform due to the presence of semicore d states which interact with the valence states: in fact the N($2s$)-derived bands are almost degenerate with the Ga($3d$)-derived bands [FMS93]. This implies that DFT calculations of GaN must also consider the contribution of the Ga($3d$)-states to get a correct picture of the valence band states. Different theoretical predictions on the electronic structure of GaN surfaces have been obtained depending on how this Ga($3d$)-state contribution to the electronic GaN band structure is taken into account in the applied model.
The first publications of theoretical studies on non-polar GaN surfaces were done in 1996 but the difficulties in growth of high crystalline quality non-polar GaN films at that time prevented that experimental measurements

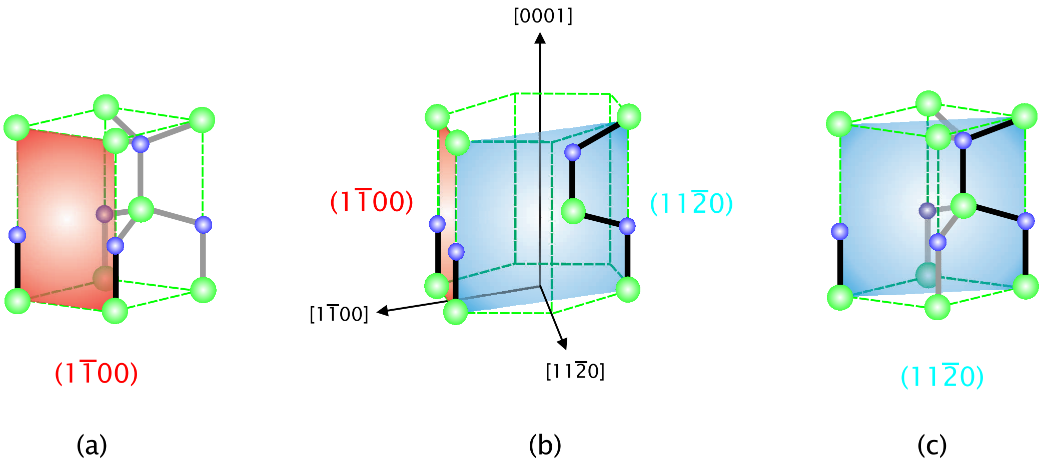

Figure 2.18: (a) Bulk unit cell of 2H-SiC with the non-polar 2H-GaN(1$\bar{1}$00) surface (m-plane) highlighted in red. (b) Hexagonal crystal cell of the 2H-GaN polytype with the non-polar 2H-GaN(1$\bar{1}$00) (2H-GaN(11$\bar{2}$0)) surface highlighted in red (blue). (c) Bulk unit cell of 2H-GaN with the non-polar 2H-GaN(11$\bar{2}$0) surface (a-plane) highlighted in blue. Green (blue) spheres indicate Ga (N) atoms. The Ga-N bonds which lie on the non-polar surfaces are indicated with brighter color.

could confirm or contradict the theoretical predictions. On each non-polar GaN surface there is an equal number of threefold-coordinated Ga- and N-atoms, thus charge neutrality is expected to be obtained without changes in stoichiometry or reconstruction. Fig. 2.18 shows the atomic structure of the non-polar (1$\bar{1}$00) (m-plane) and (11$\bar{2}$0) (a-plane) surfaces of wurtzitic GaN.

In 1996 J. E. Jaffe and co-workers presented the first results of a theoretical study on the surface relaxation of GaN in the framework of the *ab initio* Hartree-Fock method [JPZ96]. They performed total-energy calculations using a two-dimensionally periodic slab model for the most stable non-polar cleavage faces, namely, the **GaN(1$\bar{1}$00)** and **GaN(110)** surfaces of the wurtzite and zinc-blende phase, respectively. For both surfaces, when the energy is minimized the Ga-N surface bonds showed a very small rotation angle of about $6°$ accompanied by a reduction in surface bond length of about 7%. This result differs from the well-accepted model of the GaP (110) and GaAs (110) surfaces, where there is a large rotational angle in the range of 27°-31° and little change in surface bond length. The structure dependence of the calculated density of states for GaN suggested that

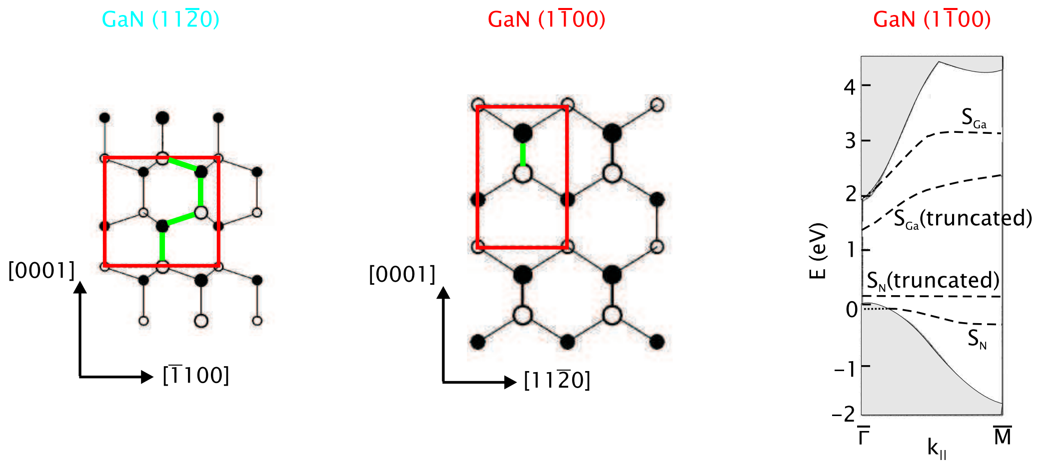

(a) (b) (c)

Figure 2.19: Schematic top view of the (a) GaN(11$\bar{2}$0) and (b) GaN(1$\bar{1}$00) surface. The red lines outline the surface unit cell. The green Ga-N bonds lie in the top-layer surface. Open and filled circles indicate Ga- and N-atoms, respectively. Big and small circles indicate top and first subsurface layer atoms, respectively. (c) Band structure calculated within the LDA for the ideal and relaxed GaN(1$\bar{1}$00) surface. The shaded region corresponds to the bulk projected band structure.

this difference is partly due to interaction between the Ga($3d$)- and N($2s$)-derived states in GaN.

J. E. Northrup and J. Neugebauer published in the same year LDA calculations on the non-polar GaN(1$\bar{1}$00) and **GaN(11$\bar{2}$0)** surfaces [NN96]. They explained the relaxation mechanism of the two GaN surfaces with a contraction of the Ga-N bond in the surface layer and a slight buckling rehybridization with N-atoms tending to adopt p^3 coordination and Ga-atoms adopting an sp^2 configuration.
The structure of the GaN(11$\bar{2}$0) surface corresponds to a chain of threefold-coordinated Ga- and N-atoms, as indicated in Fig.2.19(a). In each unit cell there are four surface atoms: two Ga- and two N-atoms. The vertical separation between the N- and Ga-atoms in the surface layer is 0.22 Å.
At the GaN(1$\bar{1}$00) surface, the unit cell contains two atoms, one Ga- and one N-atom, as indicated in Fig. 2.19(b). The vertical displacement between N- and Ga-atoms in the surface dimer is 0.22 Å and corresponds to a buckling angle of 7°.
The calculated surface energy is 3.50 eV/cell (123 meV/Å^2) and 1.95 eV/cell

(118 meV/Å^2) for the GaN(11$\bar{2}$0) and GaN(1$\bar{1}$00) surface, respectively. The cleavage of GaN should therefore be energetically favored on the $m-$plane. The calculated electronic structure for the ideal and relaxed GaN(1$\bar{1}$00) surface is shown in Fig. 2.19(c). The occupied surface state S_N is p-like and localized on the N-atoms while the empty surface state S_{Ga} is a dangling bond localized on the Ga-atoms. The effect of atomic relaxation is to increase the gap between the S_N and S_{Ga} bands by more than 1 eV. For the fully relaxed structure, the N-derived band lies just below the VBM, while the Ga-derived band lies just above the CBM, leaving the bandgap free of surface state bands at the center of the BZ.

In 2000 C. Noguez published tight-binding semiempirical calculations of the non-polar GaN(110) and GaN(1$\bar{1}$00) surfaces [Nog00]. The calculated atomic structure of the relaxed GaN(1$\bar{1}$00) surface is similar to the one obtained by Northrup and Neugebauer, with a bond rotation of the surface atoms of about ω=6° and a contraction of the surface Ga-N bond length of Δd=6$\%$ with respect to the bulk bond length.
On the other hand the calculated band structure is quite different compared to the one calculated by Northrup and Neugebauer: inside the projection of the bulk bandgap two electronic surface bands appear, one empty band (C_3) associated to Ga-like dangling bonds and one filled band (A_5) associated to N-like dangling bonds. At the $\bar{\Gamma}$-point of the surface BZ the empty C_3 band is located about 2.5 eV above the VBM and gives rise to a large contribution to the DOS within the projected bulk gap. The A_5 band is located at an energy of about 1.5 eV below the top of the bulk valence band between the $\bar{\mathrm{X}}$ and $\bar{\mathrm{M}}$ points.

In 2006 D. Segev and C. G. Van De Walle published theoretical results about wurzitic non-polar GaN surfaces [SW06]. The calculated atomic structure is in agreement with previous results: over a large range of chemical potentials the Ga–N dimer structure is the most stable and in the dimer the N-atom relaxes outward (towards an s^2p^3 configuration) while the Ga-atom relaxes inward (towards sp^2).
The surface relaxation is accompanied by a charge transfer from the Ga-dangling bond to the N-dangling bond and the GaN(11$\bar{2}$0) and GaN(1$\bar{1}$00) surfaces show similar electronic properties (Fig. 2.20). The filled surface state bands are associated with N-dangling bonds and overlap with the VBM at the $\bar{\Gamma}$-point of the surface BZ. The empty surface state bands are associated with Ga-dangling bonds and are located inside the projection of the bulk energy bandgap both at the center and at the borders of the BZ.

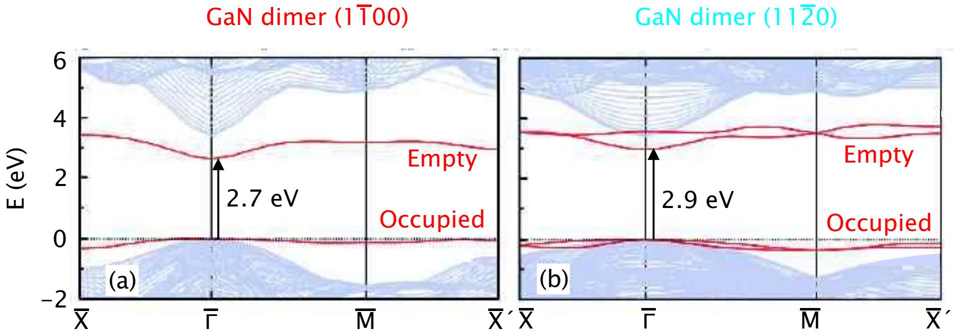

Figure 2.20: Electronic band structures of the (a) GaN dimer (1$\bar{1}$00) and (b) GaN dimer (11$\bar{2}$0) surface. Grey lines indicate the projected bulk band structure. The zero of the energy is set at the bulk VBM. Relevant energy differences between the VBM and empty Ga-like surface states are indicated by arrows (from [SW06]).

The discussion about the existence of surface states inside the energy bandgap of non-polar GaN surfaces at the center of the BZ is still today an open question which has great impact on the properties of non-polar GaN-based devices, *e. g.* nanocolumns where a pinning of the Fermi level at the lateral surface of the column would drastically affect the transport properties [CM07]. This work is aimed to give a contribution to this open discussion because, as far as our knowledge is concerned, it presents the first experimental data on the fresh cleaved GaN(1$\bar{1}$00) surface.

Chapter 3

Atomic and electronic structure of the cleaved 6H-SiC(11$\bar{2}$0) surface

We developed in 2003 a procedure to cleave 6H-SiC substrates, with the aim of cleaving GaN/6H-SiC heterostructures at a later time. In fact once we could optimize a technique to prepare and investigate by STM the freshly cleaved 6H-SiC(11$\bar{2}$0) and 6H-SiC(1$\bar{1}$00) surfaces, we planned to proceed with the cleavage of GaN films grown on 6H-SiC substrates. At the same time *free-standing* HVPE GaN substrates were introduced on the market (2004). Therefore, after concluding the study of the 6H-SiC(11$\bar{2}$0) surface, we applied the method and the experience acquired in the cleavage of a mechanical hard substrate (6H-SiC) to the cleavage of *free-standing* HVPE GaN substrates.

The attention of scientists is currently focused on the non-polar (1$\bar{1}$00) (m-plane) and (11$\bar{2}$0) (a-plane) surfaces of 4H-SiC and 6H-SiC because of improved physical properties in comparison with the polar surface (0001) of the same polytypes (Sec. 2.3). In this chapter we compare the results of experimental room-temperature X-STM/STS measurements on the cleaved non-polar 6H-SiC(11$\bar{2}$0) surface with *ab initio* simulations performed in the framework of first-principles DFT.
The chapter is structured as follows: Sec. 3.1 describes the experimental details of the work. In Sec. 3.2 the experimental X-STM/STS results are displayed with particular attention to the spatial localization of filled and empty states in the STM topographies and in Sec. 3.3 the theoretical analysis concerning the atomic and electronic structure of the cleaved 6H-SiC(11$\bar{2}$0) surface is presented. Finally Sec. 3.4 deals with the compar-

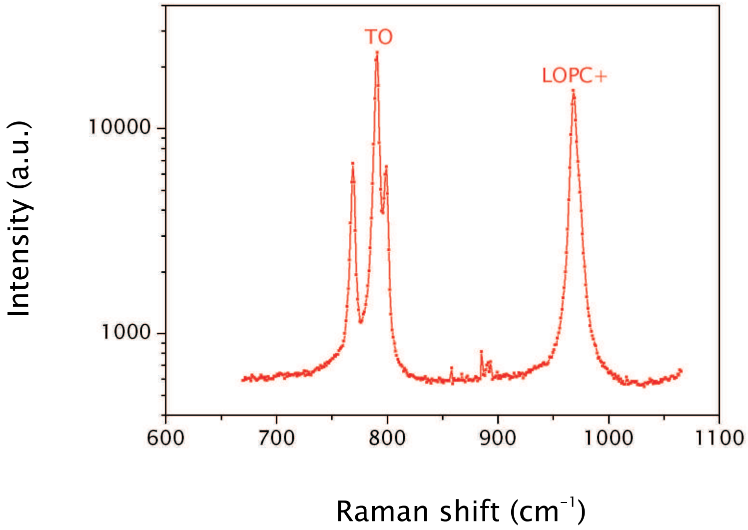

Figure 3.1: Raman profile spectrum of the TO and LO-phonon-plasmon-coupled (LOPC+) modes for the n-doped 6H-SiC substrate (Cree Inc.) [Zen].

ison between experimental and theoretical results: we propose an interpretation of the STS measurements assuming a pinning of the Fermi-energy at the freshly cleaved 6H-SiC(11$\bar{2}$0) surface of n-doped bulk material. These results have been published in 2007 [BHW$^+$07].

3.1 Experimental details

The 6H-SiC polytype is known to cleave along the non-polar (1$\bar{1}$00) and (11$\bar{2}$0) planes [SYJ00] and we decided to prepare standard c-plane 6H-SiC samples and to cleave them under UHV conditions in order to investigate the freshly cleaved non-polar 6H-SiC(11$\bar{2}$0) surface with STM. The substrates used are two inch n-type (nitrogen dopants) Si-face 6H-SiC(0001) wafers with thickness t=350 μm (Cree Inc.). The claimed specified resistivity of the wafers extends from ρ=0.04 Ω cm to ρ=0.09 Ω cm corresponding to doping concentration $N_d = 4 \times 10^{18}$cm^{-3} down to $N_d = 1 \times 10^{18}$cm^{-3}, respectively. Since the surface electronic properties as measured by STM are strongly affected by the band bending close to the surface region, it is important to know the free carrier concentration of the samples. To this aim J. Zenneck performed Raman spectroscopy at room temperature with He-Cd laser (wavelength λ=515.4 nm) [Zen]. In a polar semiconductor

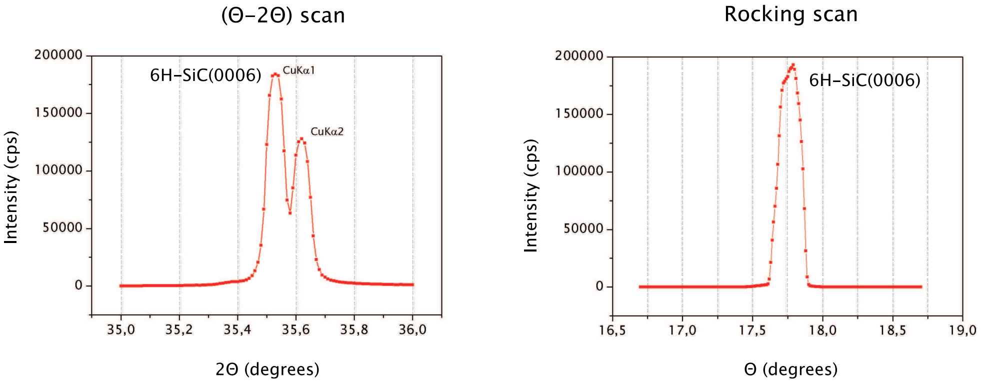

(a) (b)

Figure 3.2: XRD (a) $(\theta - 2\theta)$ scan and (b) rocking scan of the 6H-SiC(0006) peak of the n-doped substrates (Cree Inc.) [Zen].

like 6H-SiC collective excitation of free carriers (plasmon) interacts with the *Longitudinal Optical* (LO) phonon via their macroscopic electric fields, to form the *LO phonon-Plasmon Coupled* (LOPC) mode. The LOPC mode has two branches (L^+ and L^-). Three mechanisms generally contribute to the Raman scattering by the LOPC mode: *Deformation Potential* (DP), *Electro-Optical* (EO) mechanisms and *Charge-Density Fluctuation* (CDF). In semiconductors such as 6H-SiC which have large bandgap and low carrier mobility, the EO and DP mechanisms dominate the scattering process and the lower-energy branch (L_-) is not observed in the Raman spectra because of the strong damping (overdamping) [NH97]. In this case, only the L^+ mode is clearly observed. The Raman lineshape and the energy position of the LOPC+ mode changes sensitively with the free carrier density n: the LOPC+ band broadens and its peak is shifted to higher frequency with increasing n [HNU95]. The free carrier concentration at T=273 K in the n-type 6H-SiC wafers was determined to be $n = 4 \times 10^{17}$ cm^{-3} according to the position of the Raman LOPC+ peak (Fig. 3.1, Raman shift=968.57 cm^{-1}, *Full Width at Half Maximum* (FWHM)=6.11 cm^{-1}).

It is then possible to determine the donor concentration N_d and the position of the Fermi Energy E_F under the approximation of a non-degenerate semiconductor [Smi78]:

$$\begin{cases} n = N_c \; exp(E_F/K_B T) \\ N_d - n = \dfrac{N_d}{1 + \frac{1}{2} \; exp[(-E_d - E_F)/K_B T]} \end{cases}$$

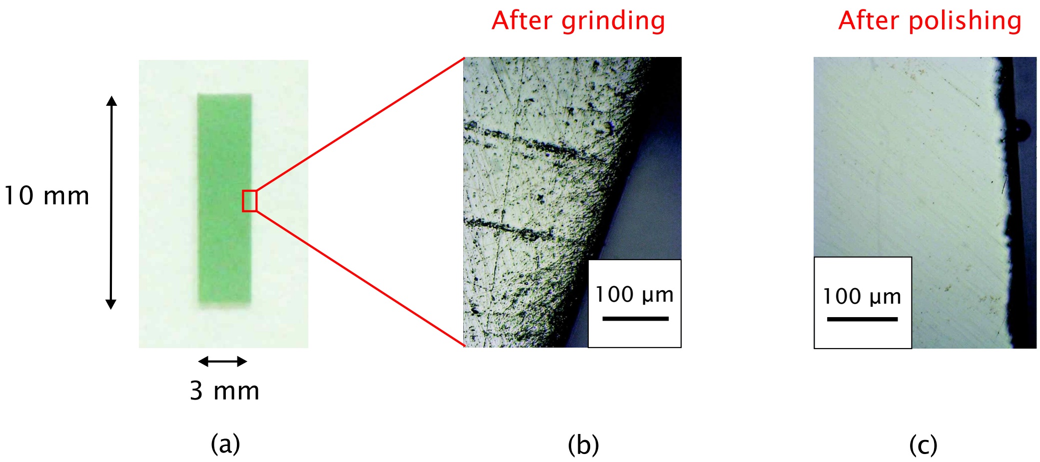

Figure 3.3: Optical images of a 6H-SiC(0001) sample during the thinning process: (a) (3×10 mm^2) sample before grinding, (b) C-side after grinding and (c) C-side after polishing.

where $N_c = 8.9 \times 10^{19}$ cm^{-3} is the effective conduction band density of states [Iof], K$_B$ is the Boltzmann constant and E_d=120 meV is the donor energy of the nitrogen dopant in 6H-SiC [SPC92]. By substituting these values in the above system we got:

$$\begin{cases} E_F = -0.092 \text{ eV from CBM} \\ N_d = 2 \times 10^{18} \text{ cm}^{-3} \end{cases}$$

Hence the Fermi energy in the bulk 6H-SiC samples at T=273 K lies just below the CBM and the derived donor concentration $N_d = 2 \times 10^{18}$ cm^{-3} falls in the claimed specification range ($N_d = 1 - 4 \times 10^{18}$ cm^{-3}).

X-Ray Diffraction (XRD) measurements were performed to get information about the crystal quality of the 6H-SiC substrates [Zen]. The experiment was done with a commercial Siemens D5000 diffractometer with a copper anode (x-ray wavelength λ=1.54056 Å of the Cu-$K_{\alpha 1}$ line). The measured FWHM of the 6H-SiC(0006) peak was 201 arcsec (θ=17.765°) and 525 arcsec (θ=17.766°) for the ($\theta - 2\theta$) and ω scan, respectively. Both values mark a good crystal quality of the material (Fig. 3.2).

The 6H-SiC wafers were cut in rectangular samples (Fig. 3.3(a)) and were thinned from 350 down to ~100 μm. The back side (C-side) of the samples was grinded and polished to get a mirror-like surface. We thinned the SiC samples by manually pushing them against a spinning plate on which diamond pastes with different grain sizes (*gs*) were applied (from

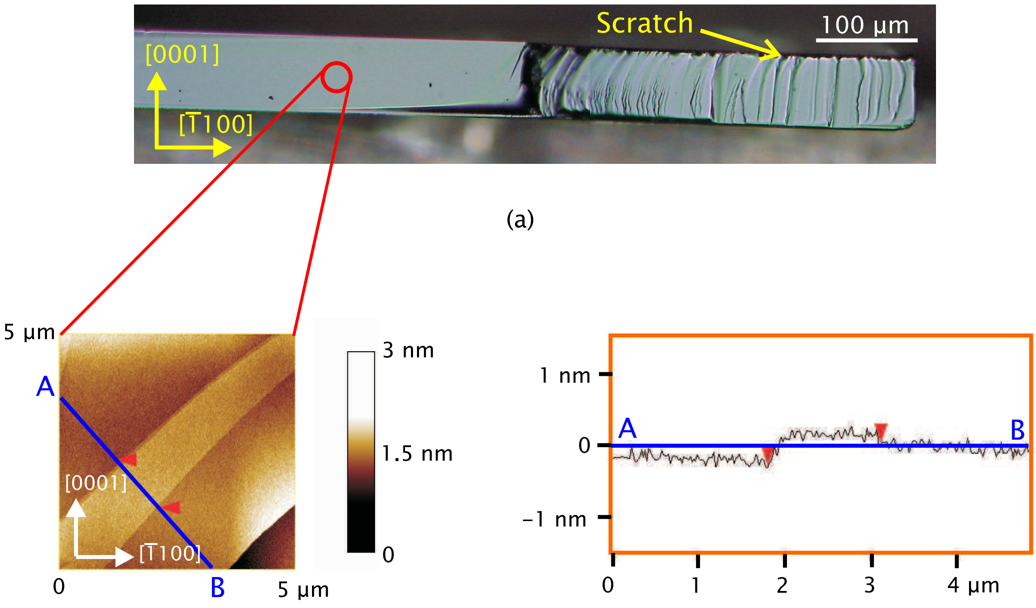

(a)

(b)

(c)

Figure 3.4: (a) Optical image of the cleaved 6H-SiC(11$\bar{2}$0) surface: the cleavage started at the scratch on the top right corner. (b) AFM image of the cleaved 6H-SiC(11$\bar{2}$0) surface: μm-large terraces are visible. (c) Cross-section profile AB of AFM image b.

gs=54 μm down to gs=1 μm). The grinding stage (gs=54−25 μm, t=3 h) leaves on the C-side of the samples long and deep scratches (Fig. 3.3(b)) which can be partly removed during the polishing stage (gs=15→7→1 μm, t=1−2 h). The final appearance of the C-side surface is almost mirror-like (Fig. 3.3(c)). Then a scratch parallel to the [1$\bar{1}$00] direction is produced with a diamond needle on the front side (Si-face) of the samples in order to induce the cleavage on the 6H-SiC(11$\bar{2}$0) plane.

We optimized the cleavage process in air and we found that a thickness $t \leq 100$ μm is needed to get cleaved surfaces which could be smooth enough for inspection with STM. In Fig. 3.4(a) we see an optical image of a cleaved 6H-SiC(11$\bar{2}$0) surface: the area close to the scratch is rough and shows several μm-high steps, while the area opposite to the scratch appears flat and mirror-like. An *Atomic Force Microscope* (AFM) image taken on the mirror-like surface shows μm-large terraces (Fig. 3.4(b)) which are smooth enough (Fig. 3.4(c)) for STM measurements.

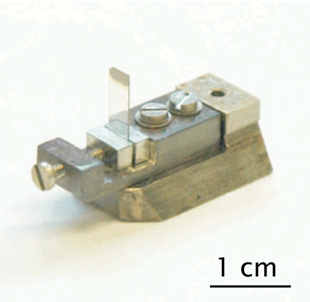

Figure 3.5: STM sample-holder with a 6H-SiC sample before insertion in the STM chamber and cleavage.

Gallium-aluminum ohmic contacts were applied at the two sides of the thinned 6H-SiC substrates just impinging an Al-rod in a Ga-droplet and rubbing the Al-rod on the sample. Then a small amount of indium was dropped on one of the two ohmic contacts and the samples were inserted between two steel chunks in the STM sample-holder (Fig. 3.5). The In droplet helps to get a good ohmic contact between the 6H-SiC sample and the STM sample-holder.

The thinned 6H-SiC substrates were then inserted in a load-chamber together with the tungsten tips for the STM experiments. Further preparation of the tungsten tips was done in UHV ($p_0 \leq 5 \times 10^{-10}$ mbar) by glowing and sputtering. The tips were characterized by field emission before transferring them into the STM (see Sec. 1.2). Finally clean 6H-SiC(11$\bar{2}$0) surfaces were obtained by *in situ* cleavage at room temperature in UHV and the STM measurements were done in the Besocke-type scanning tunneling microscope which has been previously described (Sec. 1.2). Due to the high sensitivity of the freshly cleaved 6H-SiC(11$\bar{2}$0) surface to contaminations, we had a maximum time-window of 3-4 hours to run a set of measurements on one sample even though the base pressure was better than 5×10^{-11} mbar. The origin of the contaminations on the surface is still not clear, but could be related to outgassing from the micropipes present in the substrate (micropipe density $\rho_p \sim 60 \div 80$ cm^{-2}).

3.2 STM results

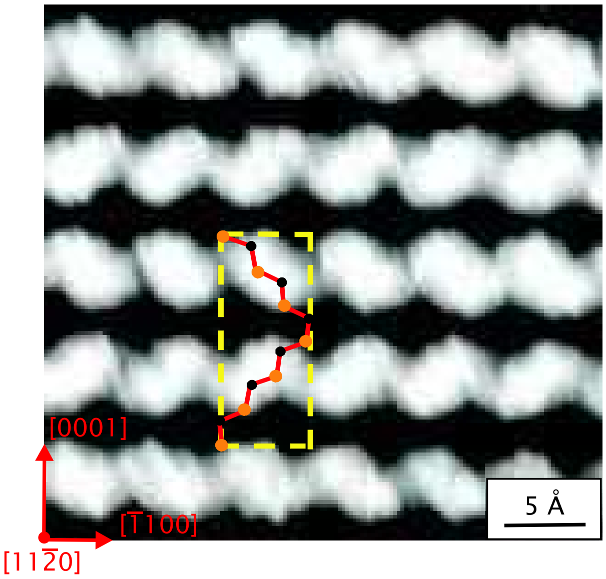

Figure 3.6: Experimental filled states STM topography ($I = 0.1$ nA) of a (35 Å × 35 Å) area on the 6H-SiC($11\bar{2}0$) surface at $U = -2.2$ V. The z-range varies between -7.5 and 7.5 pm. The surface unit cell and the 6H-SiC atomic stacking sequence (hereafter defined as zig-zag chain) are also shown: C (Si) atoms are indicated with black (orange) dots.

The cleavage of 6H-SiC on the ($11\bar{2}0$) plane along the [$1\bar{1}00$] direction generates surfaces characterized by terraces (mainly up to ∼100 nm large) separated by steps parallell to the [0001] direction. Each atom on the terrace has one bond to a second-layer atom, two bonds within the surface atomic chain and one dangling bond (ref. Fig. 3.11). The surface atomic density is $\sigma_{at} = 15.6 \times 10^{14}$ cm^{-2}. All STM measurements were performed in constant current mode. The STM topographies acquired with negative and positive bias U show the filled and the empty electronic states of the sample surface, respectively. Fig. 3.6 shows a representative filled states topography: the 6H-SiC($11\bar{2}0$) surface unit cell and atomic stacking sequence are clearly recognizable. The choice of the unit cell position is justified by the theoretical analysis presented later in this chapter (ref. Fig. 3.13). All the experimental and theoretical STM topographies reported in this chapter are shown according to the lattice directions given in Fig. 3.6. The experimental STM topographies have been elaborated with the "template-method" (Sec. 1.2) in order to improve the signal-to-noise ratio.

Fig. 3.7 shows filled states topographies at negative bias U: with decreasing bias (from right to the left), the topographies appear as more defined "bean-shaped" bright spots and the intensity corrugation along the [0001] and the [1$\bar{1}$00] directions increases. The surface unit cell is still consistent with the (1 × 1) periodicity, as if no reconstruction occured. A similar surface relaxation has been already observed in STM images of cleaved (11$\bar{2}$0) planes of II-VI compound semiconductors [SDEU97].
For low positive bias a quite uniform intensity is measured along the zig-zag chain (Fig. 3.8(a)). At higher bias the topographies show well defined maxima at peculiar locations of the 6H-SiC atomic stacking (Figs. 3.8(b), (c)). In multi-bias topographies the images obtained at negative bias, *i.e.* sampling filled states (Fig. 3.9(a)), look at first sight complementary to the ones obtained at positive bias, *i.e.* sampling empty states (Fig. 3.9(b)): the maxima in the filled states images are clearly shifted along the [1$\bar{1}$00] as well as along the [0001] direction relative to the maxima of the empty states ones (Fig. 3.9(c)).

The $I = I(U)$ spectra were acquired in the bias range from -3.0 V to +3.0 V with steps of 65 mV at constant set-point $SP_0 = SP_0\,(I_0, U_0)$ between sample and tip (see Sec 1.2). In Fig. 3.10 we show the current versus voltage $I(U)$ (Fig. 3.10(a)) characteristic measured on a (1 nm × 20 nm) area of the fresh cleaved 6H-SiC(11$\bar{2}$0) surface, the associated differential conductivity dI/dU (Fig. 3.10(b)) and the ratio of differential to total conductivity $(dI/dU)/(I/U)$ (Fig. 3.10(c)), which yields a measure of the surface DOS (normalization method according to Feenstra [FSF87]). The spectra obtained in tunneling experiments depend on the convolution between the tip and sample LDOS (Eq. 1.6). In order to remove the effects due to the electronic structure of the tip, the STM images and the STS spectra were acquired with different tips and we present in this work only the reproducible features of the repeated various experiments. In order to avoid the problem of divergence of the normalized differential conductivity $(dI/dU)/(I/U)$ at the edges of the surface bandgap, we smoothed the $I(U)$ data in the gap: this mathematical procedure does not affect the positions of the relevant features of the normalized conductivity outside the gap [rF89].
The current $I(U)$ vanishes at -0.1 V $< U <$ $+0.7$ V (Fig. 3.10(b)) and we distinguish in the DOS plot a broadened peak at U ~ -0.8 V from the position of the Fermi level at the surface (Fig. 3.10(c)).

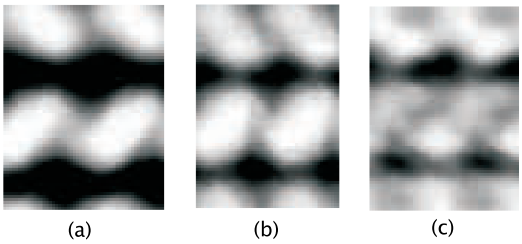

Figure 3.7: Experimental filled states STM topographies (10 Å × 15 Å) at $I = 0.1$ nA: (a) $U = -2.2$ V, (b) $U = -2.0$ V and (c) $U = -1.8$ V. Gray scale with black denoting minima and white denoting maxima tip height (the z-range is different in the images).

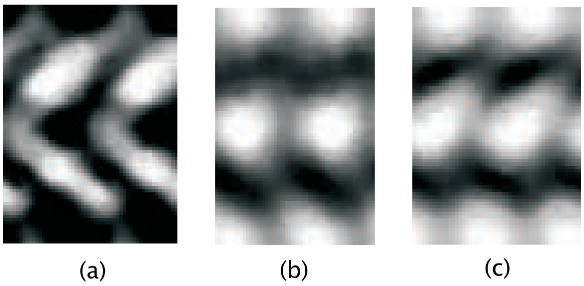

Figure 3.8: Experimental empty states STM topographies (10 Å × 15 Å) at $I = 0.1$ nA: (a) $U = +1.9$ V, (b) $U = +2.1$ V and (c) $U = +2.5$ V. Gray scale with black denoting minima and white denoting maxima tip height (the z-range is different in the images).

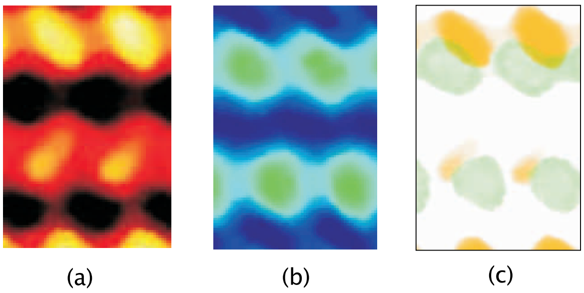

Figure 3.9: Experimental STM (I =0.1 nA) (a) filled and (b) empty states topographies (10 Å × 15 Å) in multibias mode, *i.e.* quasi-simultaneous measure of the filled and empty states at $U = -2.2$ V and $U = +2.2$ V, respectively. (c) Superposition of filled and empty states STM topographies.

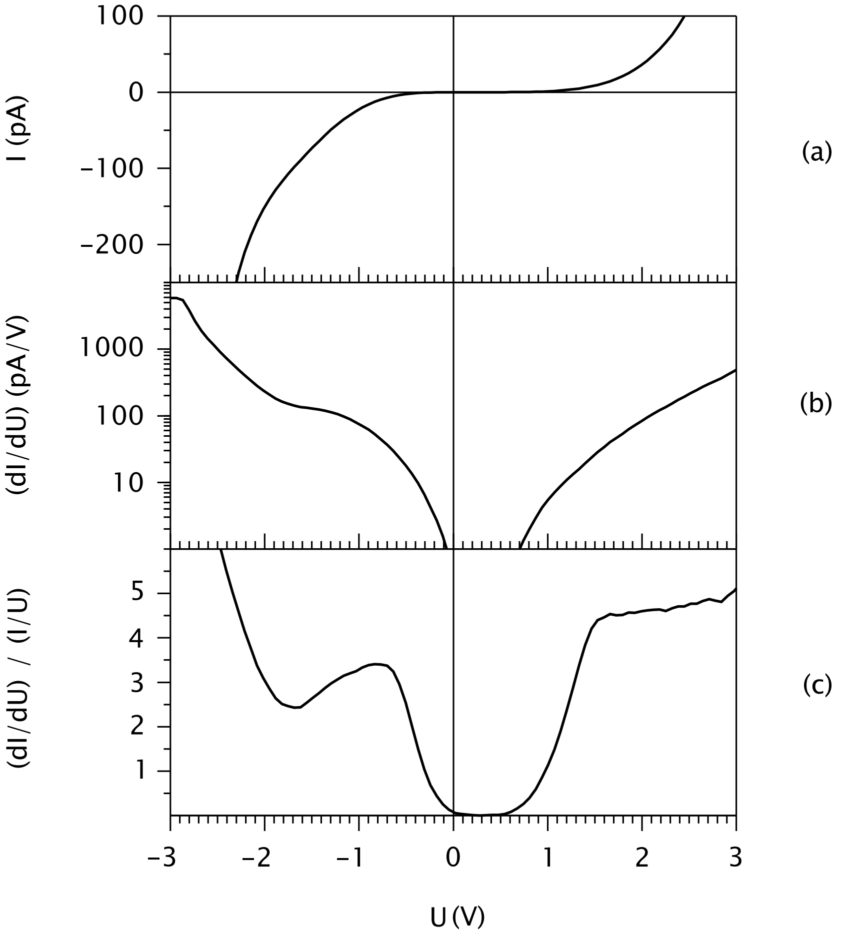

Figure 3.10: Experimental STS spectra on the fresh cleaved 6H-SiC(11$\bar{2}$0) surface averaged over an area of (1 nm × 20 nm): (a) characteristic $I = I(U)$, (b) differential conductivity dI/dU and (c) normalized differential to total conductivity $(dI/dU)/(I/U)$ or DOS.

3.3 Theoretical analysis

This is not a study of formation energy and stability of different possible surface reconstructions: indeed, although the final structure has been confirmed to depend on preparation conditions and on the availability of adatoms at the surface [SGS$^+$05, VJ03, RDH01, Rig03], the one is studied that mantains the stoichiometry of the clean surface after the cleavage. In a Cartesian coordinate system the surface plane is referred to as (xy) plane where x and y correspond to the [$\bar{1}$100] and [0001] directions, respectively (Fig. 3.11). In agreement with the experimental data presented before, the

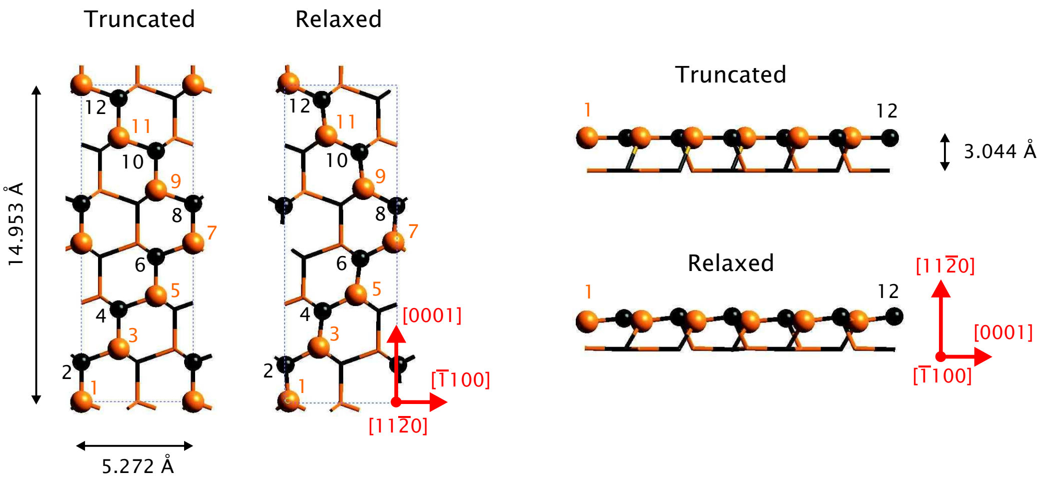

(a) (b)

Figure 3.11: (a) Top view of the hexagonal truncated (left) and relaxed (right) supercell considered. The different planes sketched are the first surface layer, and the second layer in the slab. (b) Side view of the hexagonal truncated (top) and relaxed (bottom) supercell considered. The different planes sketched are the first surface layer, and the second layer in the slab. Outermost C (Si) atoms are indicated with black (orange) dots, while atoms in the underlayer are represented with sticks of the same colors. The values for the lattice parameters are taken from [RPB$^+$02].

results of the first principles simulations indicate that the 6H-SiC(11$\bar{2}$0) surface undergoes a simple relaxation, where the (yz) glide plane symmetry of the $6H$ structure is preserved. This symmetry operation is responsible for the degeneracy of surface states along the $\bar{\mathrm{M}} - \bar{\mathrm{X}}'$ line observed in Fig. 3.12 and discussed below.

With respect to the ideal (truncated) surface, a strong distortion, towards the inversion point of the 6H-SiC zig-zag chain (C-atoms 2,8 in Fig. 3.11) can be observed, which is denoted by a deviation from the tetrahedral angle ranging from 2.6% (at inversion) up to $\simeq$ 11% (at the next neighbors of the inversion point). Correspondingly, bond lengths change along the stacking sequence for the outermost layer, with Si-atoms moving inward of $\simeq$ 0.22 Å; C-atoms are almost unchanged, but for a depression of 0.07 Å at inversion. The shortest bond is the one along [0001] at inversion which becomes 1.73 Å, with respect to the ideal 1.87 Å - 8% reduction in bond length - to minimize the tetrahedral distortion. In the (*xy*) surface plane, an in-plane displacement can be observed: with reference to the set of

Atom	*bond* (Å)	*angle* (deg.)	Δ x (Å)	Δ y (Å)	Δ z (Å)
Si(1)	1.73	112.3	0.18	0.08	-0.23
C(2)	1.75	122.7	0.04	-0.07	-0.07
Si(3)	1.74	120.7	-0.17	0.11	-0.21
C(4)	1.74	121.2	0.02	-0.04	0.00
Si(5)	1.74	121.2	-0.18	0.10	-0.21
C(6)	1.75	119.6	0.03	-0.05	0.02
Si(7)	1.73	112.3	-0.18	0.08	-0.23
C(8)	1.75	122.7	-0.04	-0.07	-0.07
Si(9)	1.74	120.7	0.17	0.11	-0.21
C(10)	1.74	121.2	-0.02	-0.04	0.00
Si(11)	1.74	121.1	0.18	0.10	-0.21
C(12)	1.75	119.6	-0.03	-0.05	0.02

Table 3.1: Structural details of the relaxation for the cleaved 6H-SiC(11$\bar{2}$0) surface, as obtained form first principles calculations: the first column labels the surface atoms, in agreement with Fig. 3.11; in the second column the bond length between atom *i* and atom *i+1* is shown, while the third column reports the angle centered on atom *i (i-1, i, i+1)*; in the remaining columns, the displacements (Δx, Δy, Δz) of each surface atom from the ideal position are indicated. The coordinate system is oriented as for Fig. 3.11 and as specified in the text.

Cartesian axes described before, Si-atoms move alternatively of ± 0.17 Å along *x* from the inversion, and C-atoms move in the opposite direction of ∓ 0.2 Å in average; the *y* coordinate changes of $\simeq -0.1$ Å for Si- and $\simeq$ 0.05 Å for C-atoms. The structural details of the relaxation are summarized in Table 3.1. These results are consistent with previously published theoretical [BCB$^+$07, PKR$^+$96, CCG06] and experimental [SGS$^+$05] results on non-polar low index surfaces of other SiC polytypes and are furthermore confirmed by different sets of calculations performed with the same accuracy using supercells with doubled periodicity along the surface plane, and no imposed symmetry: these tests rule out the spontaneous formation of reconstructions with more extended periodicity in the absence of adatoms.

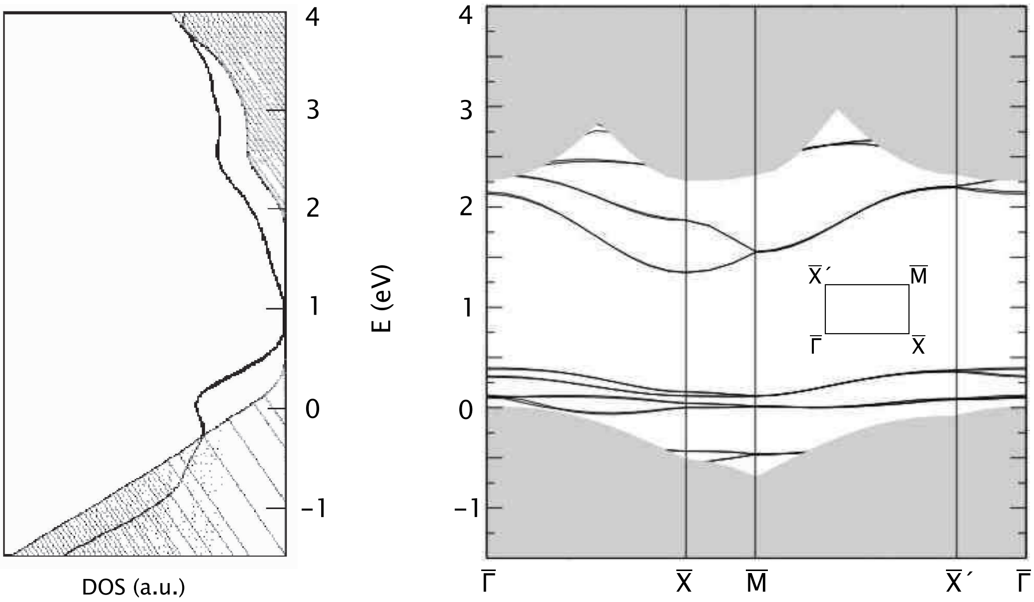

Figure 3.12: Surface DOS (left) and band structure (right) of the relaxed 6H-SiC$(11\bar{2}0)$ surface. The shaded areas show the projected bulk band structure. In the inset of the surface band structure the projected 2D Brillouin zone is shown. The DOS is obtained through a convolution with a 0.8 eV wide gaussian.

The calculated electronic structure of the relaxed 6H-SiC(11$\bar{2}$0) surface shows that a depletion of the Si-dangling bonds with formation of an empty p^* orbital and a filling of C-dangling bonds take place upon truncation. The surface band structure along high-symmetry lines in the two-dimensional Brillouin Zone is shown in Fig. 3.12. Bulk and surface calculations have been aligned upon averaging over the self-consistent potential. This operation is equivalent to the alignment of the valence band bottom for the two different calculations.[1] As usual, the energy gap is underestimated because of DFT. Associated to the (slightly different) outermost C-sites, a group of filled surface states occurs immediately above the VBM, while the three inequivalent Si-sites (for $6H$) give rise to empty surface states in the gap, below the CBM. We can distinguish only two C-derived branches in the filled surface states at the $\bar{\Gamma}$-point because the third one is resonant with bulk valence states, in correspondence with a much lower distortion

---

[1] The error bar of 0.15 eV has been estimated by comparing the average of the self-consistent potential, the deviations in potential profile from bulk and slab calculations, and the different width of the valence band in infinite (bulk) and confined (slab) calculations.

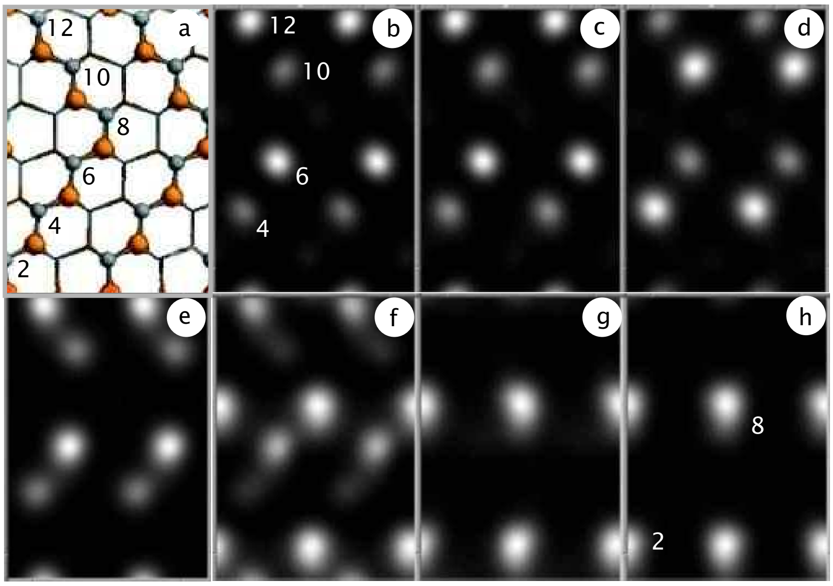

Figure 3.13: (a) Relaxed 6H-SiC(11$\bar{2}$0) plane and corresponding STS simulated images at $\simeq 1.5$ Å above the ideal truncated plane with decreasing bias from (b) U_{th} = 0 down to (h) $U_{th} = -1.2$ V in steps of 0.2 V (U_{th} = 0 is the surface *Highest Occupied* HO electronic state, at E = 0.4 eV in Fig. 3.12). The calculations have been carried out using the Tersoff-Hamann approximation [TH83].

of tetrahedral bonds at inversion: this last state is a true surface state only along the $\bar{\mathrm{X}} - \bar{\mathrm{M}}$ line. This result is confirmed by inspection of the theoretical contour plots as derived from the differential images ($\partial I/\partial U_{th}$). In Fig. 3.13 we clearly see that the spatial localization of the filled states on different surface atoms depends on the applied bias U_{th}: the highest energy states are localized on the *cubic* C-sites (atoms 4, 6, 10, 12 in Fig. 3.13(b)), while the most bound ones are localized on the *hexagonal* C-sites at inversion and present bulk-like features (atoms 2, 8 in Fig. 3.13(h)). This knowledge has been referred to by the choice of the unit cell position in Fig. 3.6.

In order to draw a direct comparison with the experiment, the tunneling current $I(x, y, z; U_{th})$ with respect to the applied bias U_{th} has been computed at the $\bar{\Gamma}$-point of the Brillouin zone. In agreement with the above discussion, the STM simulated filled states images as a function of sample bias U_{th} in the range $(-1.0, -0.2)$ V (Fig. 3.14) show "bean-shaped" bright spots with "herring-bone" distribution along the stacking sequence (here $U_{th} = 0$ corresponds to the surface HO energy). Since states localized at

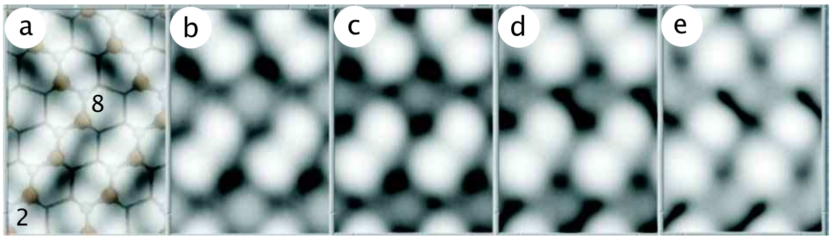

Figure 3.14: STM simulated images at constant current changing U_{th} from (a) $\simeq -1.0$ V to (e) -0.2 V with steps of 0.2 V ($U_{th} = 0$ is the surface HO state).

the inversion lie deeper in energy, the spot localized at the C-atom at inversion (atoms 2, 8) is appearing only when decreasing sample bias U_{th} from zero to negative values, *i.e.* including much deeper, bulk-like filled states. The empty states originate from Si-dangling bonds and they show a much smaller localization (Fig. 3.15(b)), in agreement with their empty state character. The filled and empty state images are thus fully complementary, as one can see from inspection of Fig. 3.15(c).

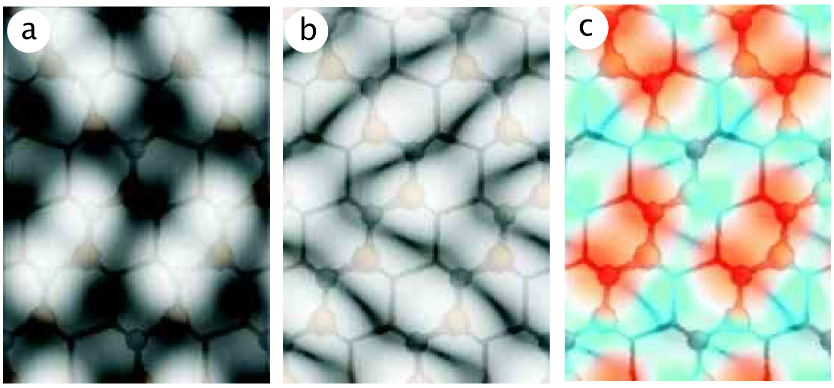

Figure 3.15: Representative simulated STM images for (a) filled and (b) empty states. Since they are localized on C- and Si-atoms, respectively, they show complementary localization in space, as can be clearly visualized in the sum-image (c). The filled states STM image is calculated at $U_{th} = -0.6$ V from the HO, the empty states image at $U_{th} = +0.2$ V from the *Lowest Unoccupied* (LU) electronic state.

3.4 Discussion

The experimental results show an unreconstructed surface, as obtained from DFT calculations. According to simulations, the filled states are concentrated on the C-atoms at the 6H-SiC(11$\bar{2}$0) surface. At the inversion point the intensity in the topographies almost vanishes decreasing the bias U_{th} from -0.2 V to -0.6 V (Fig. 3.14). At higher negative bias the tunneling process from the deep-energy lying states at the C-atom at inversion point sets on ($U_{th} < -0.6$ V). The experimental filled states topographies (Fig. 3.7) with $U \leq -2.0$ V show well defined "bean-shaped" bright spots which are localized at the *cubic* C-sites of the zig-zag chain accordingly with theory, while the minimum in the intensity corresponds to the C-atom of the *hexagonal* Si-C bond.
The simulations show that the empty states originate from Si dangling bonds and they are quite delocalized on the zig-zag chain at the (11$\bar{2}$0) surface. The experimental topographies show similar results for low positive voltages (Fig. 3.8(a)). In the multi-bias STM topographies filled and empty states are complementary both in experiment (Fig. 3.9) and theory (Fig. 3.15). This agreement confirms that the tunneling current with negative and positive bias is originating from dangling bonds located at different atoms *i.e.* anions (C) and cations (Si), respectively.

Due to n-doping ($N_d = 2 \times 10^{18}$ cm^{-3}) the Fermi energy in the bulk samples lies at $\sim$ 92 meV below the CBM. We assume that at equilibrium ($U = 0$) electrons have been transferred from the bulk to the Si-like empty surface band and *we expect immediately after the cleavage a surface Fermi level pinning at the bottom of this conduction-like band* (Fig. 3.16(c)) as for other semiconductor surfaces like Si(111)-(2×1) [Gar05], Si(100)-(2×1) [MHCH93] and GaAs(001)-(2×4) [BHWP$^+$92]. According to this interpretation, the tunneling process at small bias involves the Si-like dangling-bond states near the $\bar{\mathrm{X}}$-point at the border of the BZ of the surface band structure.
For the sake of completeness some experimental details are worth mentioning. The STS measurement was done by varying the bias U from -3.0 V to $+3.0$ V in a time window of 3 hours. Directly after the cleavage the STM topographies show a surface defects density of $\sim 10^{12}$ cm^{-2}. In the first hour of the STS measurement the spectra show reproducible features: we observe no spectral shifts, *e. g.* the tunneling current I is smaller than 500 fA for -0.1 V $< U < +0.7$ V (Fig. 3.10(b)). After 1 hour the spectra start to change and large-scale STM topographies taken after 3 hours of the STS experiment show a surface defect density of $\sim 10^{13}$ cm^{-2}. Therefore we

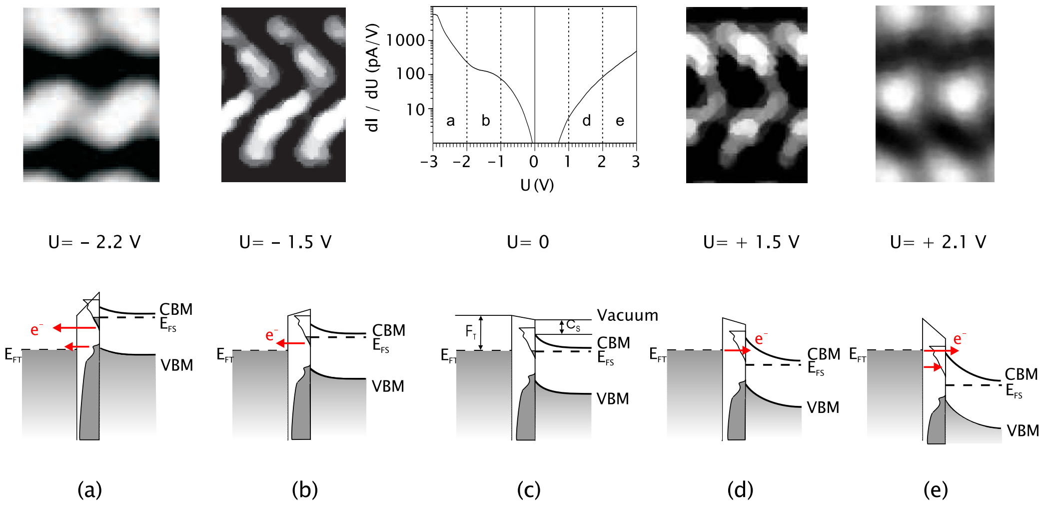

Figure 3.16: Bias dependent scheme of tunneling experiment on the fresh cleaved 6H-SiC(11$\bar{2}$0) surface. The STM topographies have been measured at I = 0.1 nA. The position of the vacuum level at equilibrium (c) is fixed according to the workfunction of tungsten tip $\phi_T \approx 4.5$ eV and the calculated electron affinity of 6H-SiC(11$\bar{2}$0) $\chi_S = I_S - E_S^{gap} \approx 2.6$ eV (with calculated ionization energy $I_S \approx$ 5.6 eV). The Fermi energy level of the tip and the sample are denoted with E_{FT} and E_{FS} respectively; the conduction band minimum of the sample is indicated with CBM and the valence band maximum with VBM.

restrict the discussion in this paper to the freshly cleaved surface with a surface defect density in the range of $\sim 10^{12}$ cm^{-2} and discuss only the STS results which were reproducible.

Typically the tunneling process is dominated by states at the $\bar{\Gamma}$-point but in our case the electrons tunneling from the Fermi energy of the sample to the tip lie close to the $\bar{\text{X}}$-point, at the bottom of the Si-like empty states band (Fig. 3.12). Therefore their crystal momentum $\vec{k}$ has a non-zero component $\vec{k}_{||}$ parallel to the surface and their transmission probability is quite low compared to the one of states at the centre of the BZ [FSF87]. Only with $U < -0.1$ V we measure a significant tunneling current ($I > 500$ fA) and the STM topography at $U = -1.5$ V shows the typical symmetry of the Si-like states (Fig. 3.16(b)). At more negative bias more electrons move upwards in the empty surface state band and moreover the transmission probability becomes high enough to strengthen the contribution to the tunneling current of states not located at the center of the BZ. At $U \cong -2.0$ V

the filled states of the C-like surface band at $\bar{\Gamma}$ come into play, as seen from the sudden increase of the tunneling current I in the STS data. Correspondingly the STM topographies show well defined "bean-shaped" distributions with maxima localized on the C-atoms (Fig. 3.16(a)). We would like to mention that a defect density of $\sim 10^{12}$ cm^{-2} at the surface could lead to Fermi level pinning slightly below the Si-like surface band. In this case the STM topographies showing Si-like character in region *b* of Fig. 3.16 can be explained by the effect of *Tip Induced Band Bending*[2] (TIBB) moving the Fermi energy at the surface from the defect related states at U =0 V into the Si-like band at $U = -0.1$ V.
As for the empty states, we see that with 0 V $< U_{exp} < +0.7$ V the tunneling current is negligible again due to the small contribution of the Si-like empty states localized around the $\bar{\mathrm{X}}$-point of the band-structure. Increasing the applied bias, electrons are totally removed from the Si-like surface states and the energy bands of the sample bend upwards at the surface due to the TIBB effect (Fig. 3.16(d)). The STM topography shows the typical Si-like contours as observed at $U = -1.5$ V (Fig. 3.16(b)). This result strongly supports the hypothesis of Fermi level pinning at the bottom of the Si-like surface band. At higher positive bias the tunneling process is dominated by empty states localized at the $\bar{\Gamma}$-point with increasing bulk-like character (Fig. 3.16(e)).

3.5 Summary and outlook

We have investigated the cleaved non-polar (11$\bar{2}$0) surface of 6H-SiC by means of X-STM/STS measurements which have been compared with *ab initio* simulations within a DFT scheme. The experimental STM images show an unreconstructed surface which reveals the peculiar atomic stacking sequence of the 6H polytype. The theoretical simulations confirm that the cleaved surface undergoes a simple relaxation. Furthermore the calculations show that the Si-atoms of the outermost layer move inwards perpendicularly to the surface of ≈ 0.2 Å with respect to the ideal truncated plane. The structural and electronic details of the relaxation process have been provided. The simulated STM topographies show that the filled states are mostly concentrated on C-atoms and the empty states on Si-atoms. This prediction is consistent with the localization of the maxima in experimen-

---

[2] The *Tip Induced Band Bending* effect denotes in STM/STS measurements on semiconductors the penetration of the electric field between sample and tip in the sample itself. The spreading of the electric field inside the sample causes a bending of the energy bands of the semiconductor close to the sample surface [FS87].

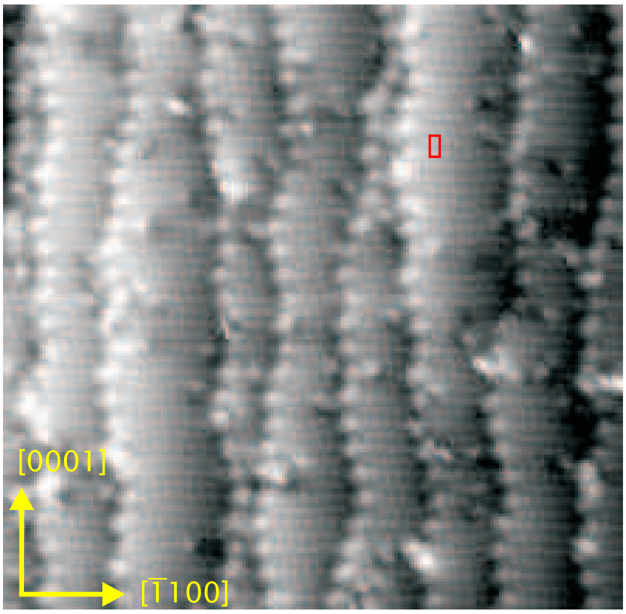

Figure 3.17: Experimental filled states STM topography (I = 0.1 nA) on the 6H-SiC(11$\bar{2}$0) surface at $U = -3.0$ V. The z-range varies between -2 and 2 Å. The surface unit cell is highlighted in red.

tal STM single-bias and multi-bias topograhies. We remind here that the calculations have been performed by M. C. Righi *et al.* and A. Catellani from the Modena University and IMEM-CNR in Parma (Italy), respectively. The results of the simulations are included for sake of completeness in this work, with the agreement of the authors.

The experimental STS data can consistently be explained assuming a Fermi level pinning at the 6H-SiC(11$\bar{2}$0) surface inside the bandgap of the semiconductor for n-doped samples. The corresponding STM topographies and the calculated surface band structure support a Fermi level pinning at the bottom of the Si-like surface band at $\bar{\mathrm{X}}$. The tunneling process at low bias $|U|$ depends on the surface states at the border of the Brillouin zone, while at higher bias the states at the $\bar{\Gamma}$-point dominate the contours of the STM topographies.

The cleaved non-polar 6H-SiC(11$\bar{2}$0) surface can be further investigated by X-STM/STS experiments. One interesting topic would be the characterization of defects, for example donors (like N) or surface steps. We note in Fig. 3.17 that the cleavage of the SiC samples generates terraces parallel to the [0001] direction and the maxima in the filled states topographies appear to be localized at the border between two terraces. Further

STM measurements are necessary to get a deeper insight into the electronic properties of the defects in the material. This experimental result has not been further investigated within this work.

Chapter 4

Atomic and electronic structure of the cleaved GaN($1\bar{1}00$) surface

One of the tasks of this work is to investigate the electronic properties of the cleaved non-polar GaN($1\bar{1}00$) surface by X-STM/STS. When in 2004 free-standing GaN HVPE *quasi*-substrates were introduced on the market, we decided to use them for our project. These substrates are more promising for cleavage than heteroepitaxial GaN films because the formers are stress-free. The probability of achieving a smooth cleavage on a large surface area suited for STM measurements is much higher than for thin GaN epilayers grown on other materials. The experience gained from the cleavage of the 6H-SiC substrates could be transferred straightforwardly to the free-standing HVPE GaN ones.

In the last five years a great interest has arised on non-polar GaN surfaces and has been motivated by the development of GaN-based devices like LEDs and LDs emitting in the violet-green range with high QE (Sec. 2.4). In view of these applications an experimental characterization of non-polar GaN surfaces is necessary and only few publications on this topic are found in literature.
In this chapter we compare the results of experimental room-temperature X-STM/STS measurements on the cleaved non-polar GaN($1\bar{1}00$) surface with *ab initio* simulations performed in the framework of first-principles DFT. The chapter is structured as follows: Sec. 4.1 reports the experimental details of the work. In Sec. 4.2 the experimental X-STM/STS results are displayed and in Sec. 4.3 the theoretical analysis concerning the atomic and electronic structure of the cleaved GaN($1\bar{1}00$) surface is presented. Finally Sec. 4.4 deals with the comparison between experimental and theoretical results: we propose an interpretation of the X-STM/STS measurements on

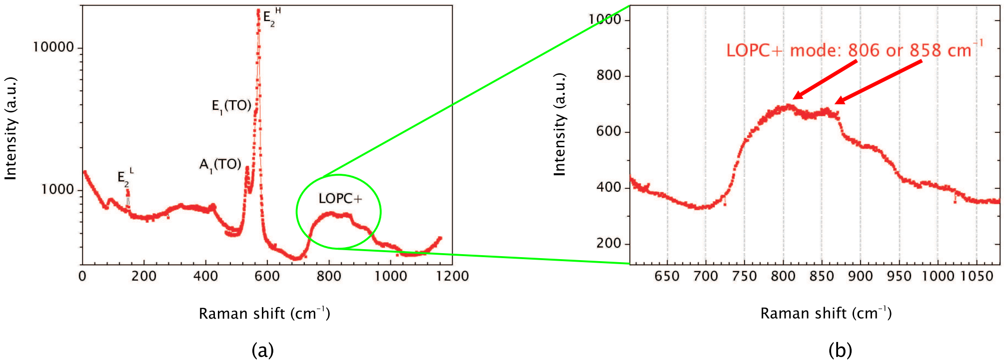

Figure 4.1: Raman spectra at room temperature of the unintentionally n-doped free-standing HVPE GaN samples: (a) overview and (b) zoom on the LOPC+ mode [Zen].

the clean cleaved GaN(1$\bar{1}$00) surface of unintentionally n-doped samples assuming that the Fermi Energy is not pinned at the surface and that the TIBB effect rules the tunneling experiment.

4.1 Experimental details

Two-inch unintentionally n-doped free-standing HVPE GaN(0001) *quasi*-substrates (thickness t=300 μm) grown on sapphire (Al_2O_3) (LUMILOG) were cleaved in order to study the clean cleaved non-polar GaN(1$\bar{1}$00) (m-plane) surface by STM. The resistivity of the wafers was specified by the producer as $\rho \approx 0.03\ \Omega$ cm, which corresponds to a free carrier concentration $n = 1 - 3 \times 10^{18}$ cm^{-3}. Raman spectroscopy and Hall-effect measurements were performed in order to determine the free carrier concentration in the GaN samples.

The Raman spectra of the free-standing GaN samples were measured at room temperature with a He-Cd laser (wavelength λ =515.4 nm) [Zen]. In polar semiconductors like GaN we can observe coupled modes of electronic and lattice excitations, *e. g.* the LOPC mode, which consists of upper- and lower-frequency branches (denoted as L^+ and L^-, respectively, see Sec. 3.1). In n-type GaN the free carrier concentration n can be estimated from the Raman shift of the LOPC+ peak, which shifts to higher frequency with increasing n [Har02]. The value of n in the free-standing GaN samples was determined to be bewteen $n = 2.8 \times 10^{18}\ \mathrm{cm}^{-3}$ and $n = 4.5 \times 10^{18}\ \mathrm{cm}^{-3}$ according to the position of the LOPC+ peak (Raman shift=806 cm^{-1} and Raman shift=858 cm^{-1}, respectively) (Fig. 4.1). It is difficult to determine

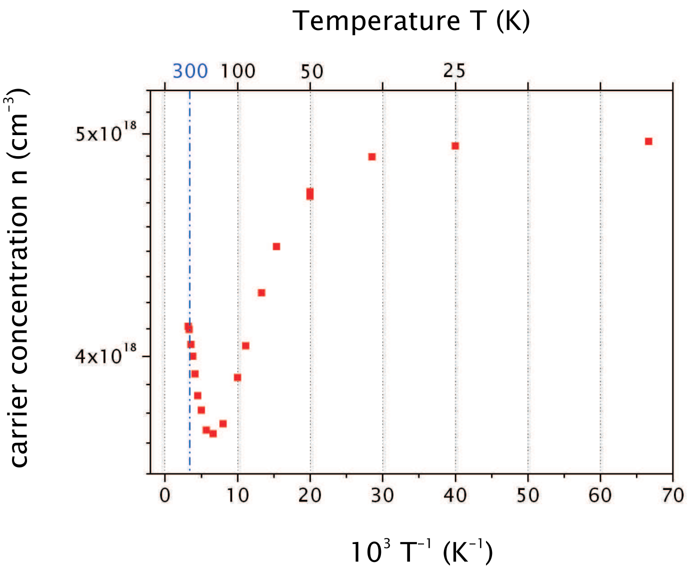

Figure 4.2: DC Hall-effect data for HVPE GaN samples (3×3 mm^2) in Van der Pauw geometry over the temperature range 10-300 K [Pin].

the precise value of the Raman shift matching the LOPC+ peak maximum because in the case of n-type GaN the peak is quite broad at high n.

Direct current (DC) Hall-effect measurements were performed on HVPE GaN samples (3×3 mm^2) in Van der Pauw geometry over the temperature range 10-300 K (Fig. 4.2) [Pin]. The Hall data can be explained by means of a two-layers model which assumes the presence of a thin ($t_1 \approx 200$ nm), highly degenerate n-type region at the backside of the HVPE GaN samples and a thick ($t_2 \approx 300\ \mu$m), high crystal quality bulk GaN layer [LM97]. The thin degenerate region is characterized by a high density of stacking faults and has already been observed in HVPE GaN layers grown on sapphire. In order to extract the bulk GaN layer parameters, a correction should be applied to the raw Hall data. However the highly degenerate region influences mainly the GaN layers electrical properties at low temperature and we can use the carrier concentration n=4.1×10^{18} cm^{-3} determined from the raw data at room temperature as a first good approximation.

The carrier concentrations measured with Raman spectroscopy and Hall-effect agree very well with each other and we hold the value measured by Hall-effect ($n = 4.1 \times 10^{18}\ \mathrm{cm}^{-3}$) for subsequent analysis. The n-type conductance of the material in the mid $10^{18}\ \mathrm{cm}^{-3}$ range denotes a Fermi energy level close to the CBM in the bulk material.

It is well known that Ga vacancies are present as dominant intrinsic ac-

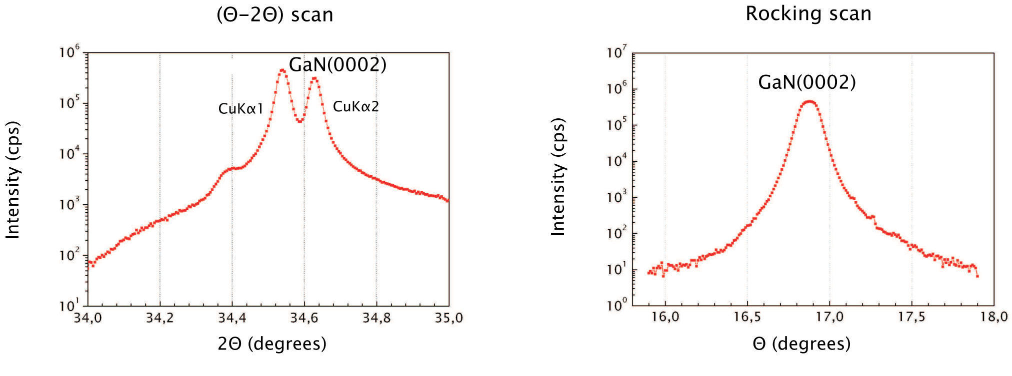

(a)

(b)

Figure 4.3: XRD (a) ($\theta - 2\theta$) scan and (b) rocking scan of the GaN(0002) peak of the unintentionally n-doped free-standing HVPE GaN substrates (LUMILOG) [Zen].

ceptors in HVPE GaN thick layers grown on sapphire substrate. The concentration N_a of Ga vacancies in the GaN layer is particularly high in the region close to the interface with the substrate and decreases from more than 10^{19} cm^{-3} to below 10^{16} cm^{-3} as the distance from the interface increases from 1 to 300 μm [LMP$^+$03]. The depth profile of Ga vacancies is very similar to the one reported for O impurities, which behave as donors in GaN films. However, beginning at about 300 nm from the interface, Si takes over as dominant donor: at a distance ≥ 30 μm from the interface with the substrate, *Second Ion Mass Spectroscopy* (SIMS) measurements detect only Si at about $N_d = 1 \times 10^{17}$ cm^{-3} within the GaN layers [LSM$^+$01]. O and Si impurities spread from the sapphire substrate into the GaN layer during the HVPE growth.

The measured carrier concentration n could therefore reasonably be explained with Si impurities or other n-type donor defects present in the HVPE GaN samples. Here it is enough to notice that the measured n-type conductance is coherent with existing literature data about HVPE free-standing GaN layers.

XRD measurements were performed to get information about the crystal quality of the free-standing GaN *quasi*-substrates [Zen]. The experiment was done with a commercial Siemens D5000 diffractometer with a copper anode (X-ray wavelength λ =1.54056 Å, Cu-$K_{\alpha 1}$ line). The measured FWHM of the GaN(0002) peak was 97 arcsec ($\theta = 17.269°$) and 353 arcsec ($\theta = 16.876°$) for the ($\theta - 2\theta$) and ω scan, respectively. Both values mark a good crystal quality of the material (Fig. 4.3).

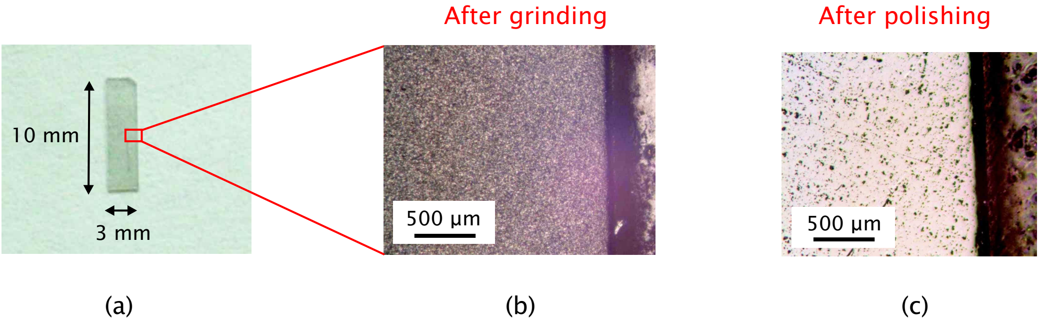

(a) (b) (c)

Figure 4.4: Optical images of a free-standing HVPE GaN(0001) sample during the thinning process: (a) (3×10 mm^2) sample before grinding, (b) N-side after grinding and (c) N-side after polishing.

The free-standing GaN *quasi*-substrates were cut in rectangular samples (Fig. 4.4(a)) and thinned from 300 down to $\sim$100 μm. The back side (N-side) of the samples was grinded and polished to get a mirror-like surface. We thinned the GaN samples by manually pushing them against a spinning plate on which different abrasive media with grain sizes gs (from gs=20 μm down to gs=1 μm) were applied. The grinding stage was done with a SiC pad attached to the spinning plate (gs=20 μm, t=2 h). At the end of the grinding process the N-side of the samples looked dim and rough (Fig. 4.4(b)). The surface quality can be improved by depositing diamond pastes with decreasing grain size (gs=15$\rightarrow$7$\rightarrow$3$\rightarrow$1 μm, t=2−3 h) on the spinning plate. The final appearance of the N-side surface is almost mirror-like even though several scratches and macroscopic voids are still visible (Fig. 4.4(c)). The goal of the polishing stage is to get a smooth and defect-free surface in order to induce the sample cleavage at the height of a scratch which is traced with a diamond needle parallel to the $[1\bar{1}00]$ direction on the front side (Ga-side) of the samples.

We optimized the cleavage in air and found that a thickness $t\leq$100 μm is needed to get cleaved surfaces which could be smooth enough for inspection by X-STM. In Fig. 4.5(a) we see an optical image of a cleaved GaN$(1\bar{1}00)$ surface: several macroscopic steps are visible on the whole surface. Nevertheless AFM measurements reveal the existence of flat terraces with a width of some hundreds nm (Fig. 4.5(b) and (c)). These terraces are smooth enough to allow X-STM measurements.

In order to make an evaluation of the density of dislocations in the bulk GaN material a thin lamella was extracted by *Focused Ion Beam* (FIB) etch-

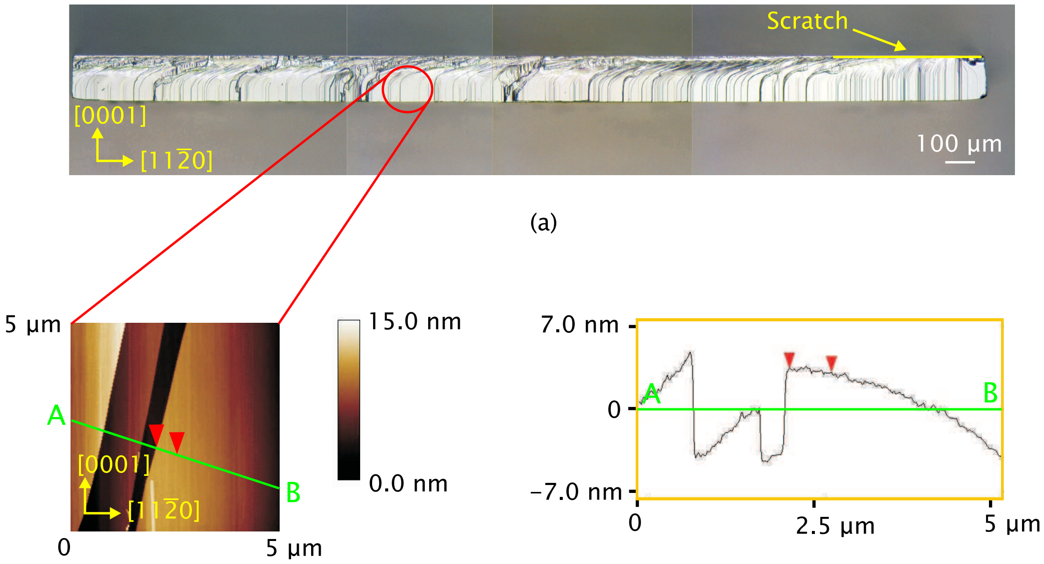

(a)

(b)

(c)

Figure 4.5: (a) Optical image of the cleaved GaN($1\bar{1}00$) surface: the cleavage started at the scratch on the top right corner. (b) AFM image of the cleaved GaN($1\bar{1}00$) surface: large terraces (some hundreds nm) are visible. (c) Cross-section profile along line AB.

ing close to the N-side of a cleaved GaN sample (Fig. 4.6(a)) and was afterwards investigated by TEM using a Philips CM 200 UT-FEG operated at 200 keV [Urb]. In (Fig. 4.6(b)) we can distinguish between a thin highly-defective region close to the N-side of the sample ($t_1 \approx$ few hundreds nm) and a high-crystalline quality region in the rest of the material ($t_2 \approx 7\,\mu$m). The bend contours observed in the bottom half of the image are due to bending of the GaN lamella [Rei97]. Several defects induced by the grinding process are identified close to the N-side of the sample (Fig. 4.6(c)) while the bulk material shows only few dislocations parallel to the c-axis ($\sigma_d = 5 \times 10^7$ cm^{-2}) (Fig. 4.6 (d)).

To perform the STM measurement we evaporated low resistance ohmic contacts on the front-side of the GaN samples. The ohmic contacts were achieved by the deposition of a metallic Ti/Al/Ti/Au layer and subsequent rapid thermal annealing [Pin]. The contact resistance is $\mathrm{R_c} = 4\ \Omega\ \mathrm{mm}$. Then a small amount of indium was dropped on one of the two ohmic

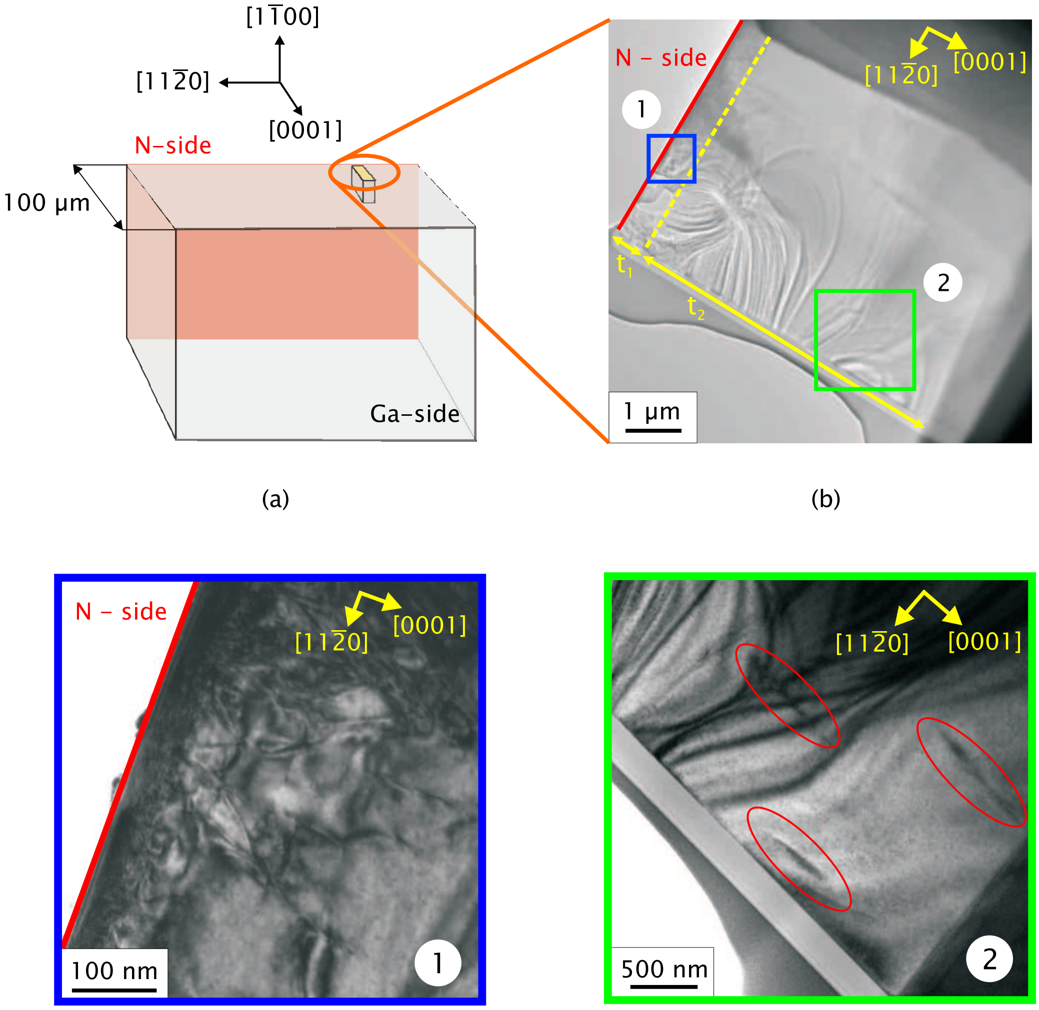

(a) (b)

(c) (d)

Figure 4.6: Bright field TEM images of a cleaved HVPE GaN sample (thickness ≈ 100 μm): (a) scheme showing the GaN sample and the position of the lamella extracted by FIB for subsequent TEM investigation. (b) Plain view of the cleaved GaN(1$\bar{1}$00) surface with highly defective region close to the N-side [1] and high crystalline quality bulk material [2]. (c) Plain view of the highly defective region close to the N-side of the GaN sample. (d) Plain view of the bulk region with dislocations parallel to the c-axis highlighted in red [Urb].

contacts and the GaN samples were inserted between two steel chunks in the STM sample-holder. The In droplet helps to get a good ohmic contact between the GaN sample and the STM sample-holder.

The thinned GaN samples were then inserted in a load-chamber together with the tungsten tips for X-STM experiments. Further processing of the tungsten tips was done in UHV ($p_0 \leq 5 \times 10^{-10}$ mbar) by glowing and sputtering. The tips were characterized with field emission before transferring them into the STM (see Sec. 1.2). Finally clean GaN($1\bar{1}00$) surfaces were obtained by cleavage at room temperature in UHV and the measurements were done in the Besocke-type scanning tunneling microscope which has been previously described (Sec. 1.2).

4.2 STM results

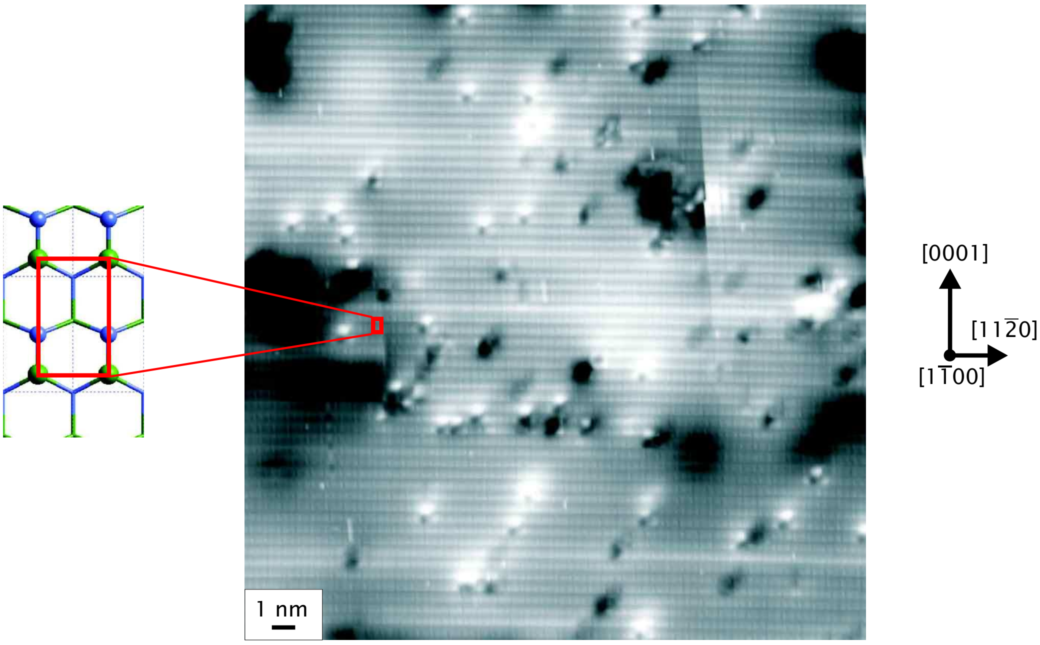

Figure 4.7: Experimental empty states STM topography ($U = +3.2$ V and $I = 0.1$ nA) of a (26.5 nm × 26.5 nm) area of the cleaved GaN(1$\bar{1}$00) surface. The z-range varies between -0.6 Å and $+0.6$ Å. The surface unit cell is highlighted in red and its stick-ball model is magnified on the left: the different planes sketched are the first surface layer and the second layer in the slab. Outermost N (Ga) atoms are indicated with blue (green) spheres, while atoms in the underlayer are represented with sticks of the same colors.

The cleavage of GaN on the (1$\bar{1}$00) plane generates surfaces characterized by terraces (mainly a few hundreds nm large) separated by steps parallel to the [0001] direction, as seen in the STM topographies (not shown). Each atom on the terrace has two bonds to second layer atoms, one bond within the surface layer and one dangling bond (ref. Fig. 4.14). Fig. 4.7 shows an empty states STM topography of the cleaved GaN(1$\bar{1}$00) surface: the surface unit cell is still consistent with the (1×1) periodicity, as if no reconstruction occurred. The choice of the unit cell position is justified by comparison of experimental data and DFT calculations presented later in this chapter (ref. Sec. 4.4). On the surface we can clearly distinguish local and extended defects which have not been further analyzed within this work and will be shortly discussed for the outlook at the end of this

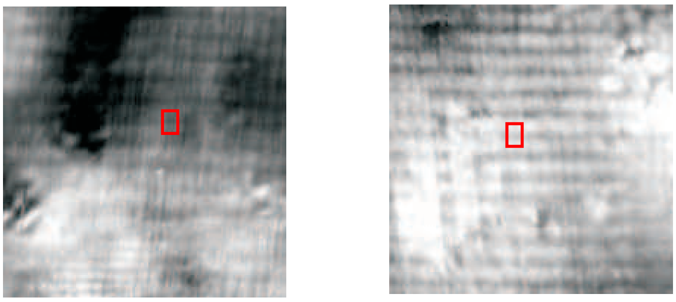

(a) U = - 1.3 V (b) U = - 1.5 V

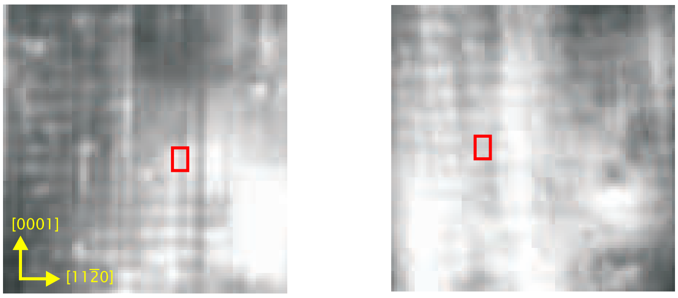

(c) U = - 2.2 V (d) U = - 2.5 V

Figure 4.8: Experimental filled states STM topographies at $I = 0.1$ nA: (a) $U = -1.3$ V, (b) $U = -1.5$ V, (c) $U = -2.2$ V and (d) $U = -2.5$ V. Gray scaled with black denoting minimal and white denoting maxima tip height (the z-range is different in the images) with the [11$\bar{2}$0] direction along x and the [0001] along y. The surface unit cell is highlighted in red.

chapter. A similar surface relaxation has been already observed in STM topographies of cleaved planes of wurzitic II-VI compound semiconductors [SDEU97].

Fig. 4.8 shows filled states STM topographies from $U = -1.3$ V down to $U = -2.5$ V. The filled states are somewhat delocalized forming a one-dimensional chain along the [11$\bar{2}$0] direction. It is quite difficult to measure filled states STM topographies even though it is possible to measure a tunneling current I. Even changing both the tip and the sample did not allow us to get a more stable and defined resolution of the topographies.

Fig. 4.9 shows empty states STM topographies from $U = +4.0$ V down to $U = +1.5$ V. The atomic resolution is much higher in the empty than in the filled states topographies and in the former case it is possible to distinguish the surface states localized on single atoms. Local surface defects are clearly observed and the atomic corrugation vanishes for bias approaching

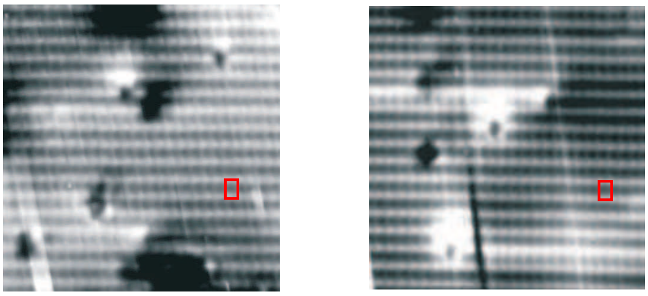

(a) U = + 4.0 V (b) U = + 3.6 V

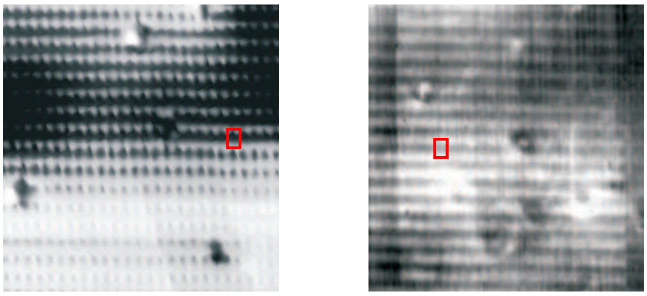

(c) U = + 3.0 V (d) U = + 2.5 V

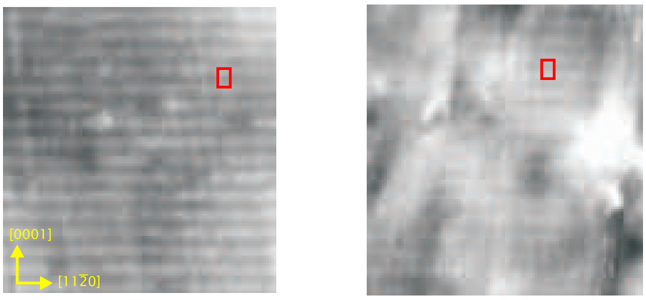

(e) U = + 2.0 V (f) U = + 1.5 V

Figure 4.9: Experimental empty states STM topographies at $I = 0.1$ nA: (a) $U = +4.0$ V, (b) $U = +3.6$ V, (c) $U = +3.0$ V, (d) $U = +2.5$ V, (e) $U = +2.0$ V and (f) $U = +1.5$ V. Gray scaled with black denoting minimal and white denoting maxima tip height (the z-range is different in the images) with the [11$\bar{2}$0] direction along x and the [0001] along y. The surface unit cell is highlighted in red.

$U = +1.5$ V where the STM topography seems to be dominated by tunneling through surface defects.

In multi-bias (*mb*) STM topographies each line of the image is scanned at alternating bias in order to compare the spatial localization of the maxima of filled ($U < 0$) and empty ($U > 0$) states. Fig. 4.10 shows two sets of

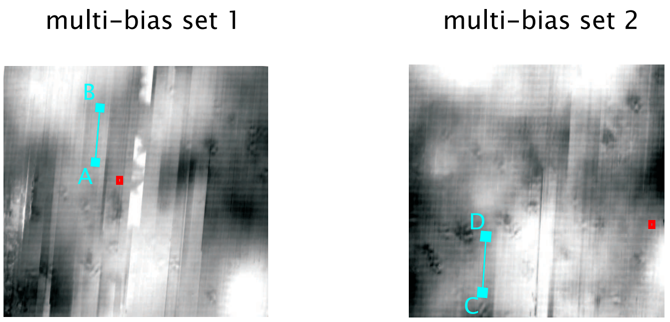

(a) U = – 1.3 V (b) U = – 1.3 V

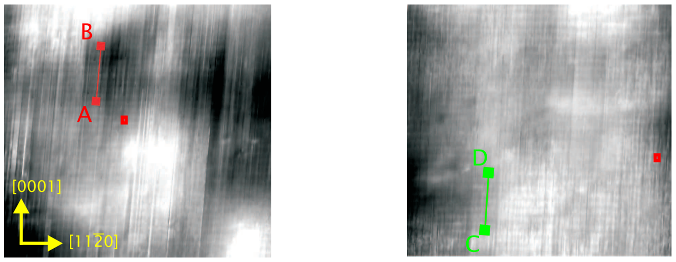

(c) U = + 2.2 V (d) U = + 3.0 V

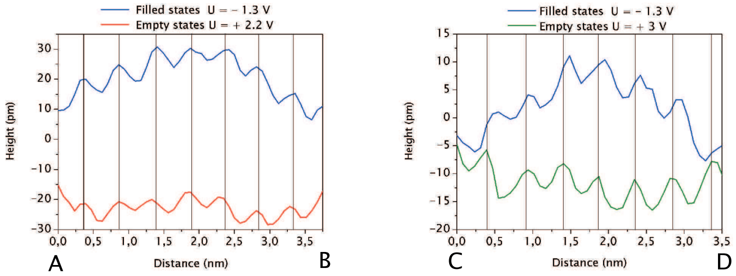

(e) (f)

Figure 4.10: Experimental STM topographies ($I = 0.1$ nA) in multi-bias (*mb*) mode (sample 2007-066). *Mb* set 1: (a) filled ($U = -1.3$ V) and (c) empty ($U = +2.2$ V) states topography. *Mb* set 2: (b) filled ($U = -1.3$ V) and (d) empty ($U = +3.0$ V) states topography. (e) Cross section profile along line AB of filled (blue) and empty (red) states for *mb* set 1. (f) Cross section profile along line CD of filled (blue) and empty (green) states for *mb* set 2. Gray scaled with black denoting minimal and white denoting maxima tip height (the z-range is different in the images) with the [11$\bar{2}$0] direction along x and the [0001] along y. The surface unit cell is highlighted in red.

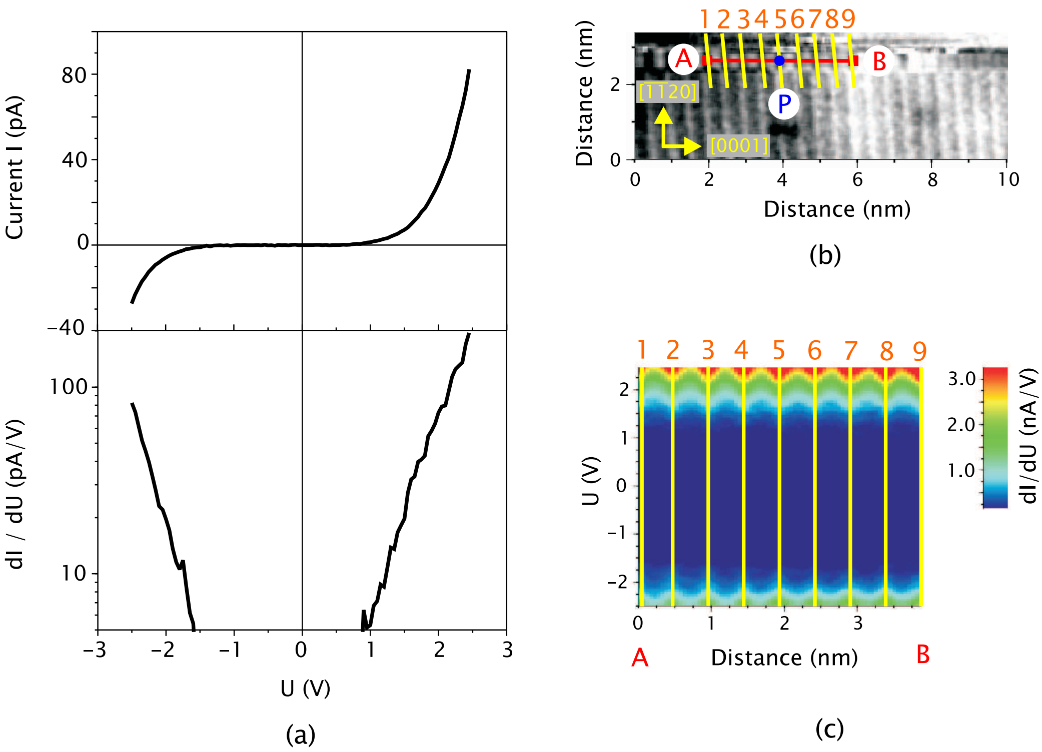

(a)

(b)

(c)

Figure 4.11: Experimental normalized STS spectra on the cleaved GaN($1\bar{1}00$) surface (sample 2008-004): (a) characteristic $I = I(U)$ and associated differential conductivity dI/dU measured on a (5 Å × 1 Å) area centered on position P of the cleaved surface; (b) empty states STM topography of a (10 nm × 3.3 nm) area of the cleaved surface ($U = +2.4$ V and $I = 0.05$ nA); (c) differential conductivity dI/dU spectrum-section along line AB [Loe].

mb topographies measured on sample 2007-066 (set 1: Figs. 4.10(a, c), set 2: Figs. 4.10(b, d)). The line scans reported at the bottom of the figure show that the maxima of the filled states at $U = -1.3$ V overlap with the maxima of the empty states at $U = +2.2$ V (Fig. 4.10(e)). On the other hand, the maxima of the filled states at $U = -1.3$ V are slightly shifted along the [0001] direction as compared to the maxima of the empty states at $U = +3.0$ V (Fig. 4.10(f)).

In Fig. 4.11 we show the normalized STS data measured on the cleaved GaN($1\bar{1}00$) surface of sample 2008-004 [Loe]. Fig. 4.11(a) shows the current versus voltage characteristic and the associated differential conductivity measured on a (5 Å × 1 Å) area centered on position P of the cleaved surface (Fig. 4.11(b)). The tunneling current vanishes within the bias range $-1.6\ V < U < +0.9\ V$. Fig. 4.11(c) shows the differential con-

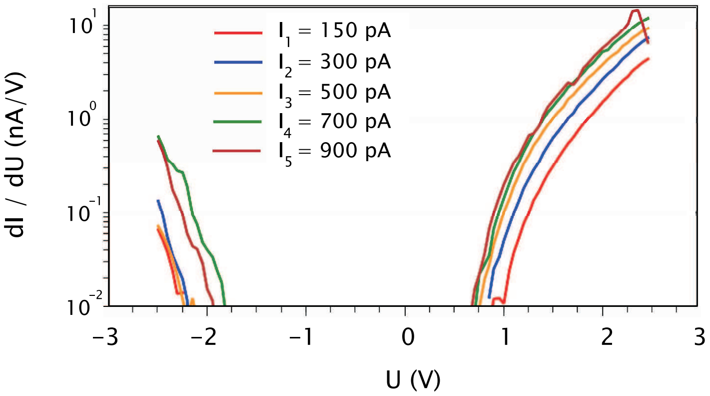

Figure 4.12: Differential conductivity spectra dI_i/dU (i=1, 2, 3, 4, 5) measured on the GaN(1$\bar{1}$00) cleaved surface (sample 2008-004) at constant bias (U_0 = +1.7 V) and various current setpoints I_i: I_1 =150 pA (red), I_2 =300 pA (blue), I_3 =500 pA (orange), I_4 =700 pA (green) and I_5 =900 pA (brown) [Loe].

ductivity spectrum-section along line AB of Fig. 4.11(b): the differential conductivity is represented in color scale as a function of the position along the line AB (horizontal axis) and the applied bias (vertical axis). In the empty states topography of Fig. 4.11(b) we can distinguish nine tip-height minima between point A and B. If we denote the nine minima with yellow lines in Fig. 4.11(c), we observe that the maxima of the differential conductivity are located at the same positions for filled and empty states along the [0001] direction on line AB.

Fig. 4.12 shows differential conductivity spectra dI_i/dU (i=1, 2, 3, 4, 5) measured on sample 2008-004 at constant bias (U_0 =+1.7 V) and various current set-points I_i: each dI_i/dU spectrum is measured at different tip-sample distance d_i [Loe]. The tip-sample distance decreases with increasing current set-point I_i at constant bias U_0. The measured dI_i/dU spectra show that a decrease of the tip-sample distance induces a contraction of the bias range where no tunneling current flows between the two electrodes. The different dI_i/dU characteristics tend to overlap each other when the tip approaches the contact with the sample.

In Fig. 4.13 the normalized STS data measured on the cleaved surface of sample 2007-066 are shown. Fig. 4.13(a) shows the current versus bias characteristic and the associated differential conductivity measured on a (5 Å × 2 Å) area centered on position P of the cleaved surface (Fig. 4.13(b)). The current vanishes within the bias range $-0.9\,V < U < +1.3\,V$. The differential conductivity spectrum-section along line AB of Fig. 4.13(b) is shown in Fig. 4.13(c). In the empty states topography of Fig. 4.13(b) we

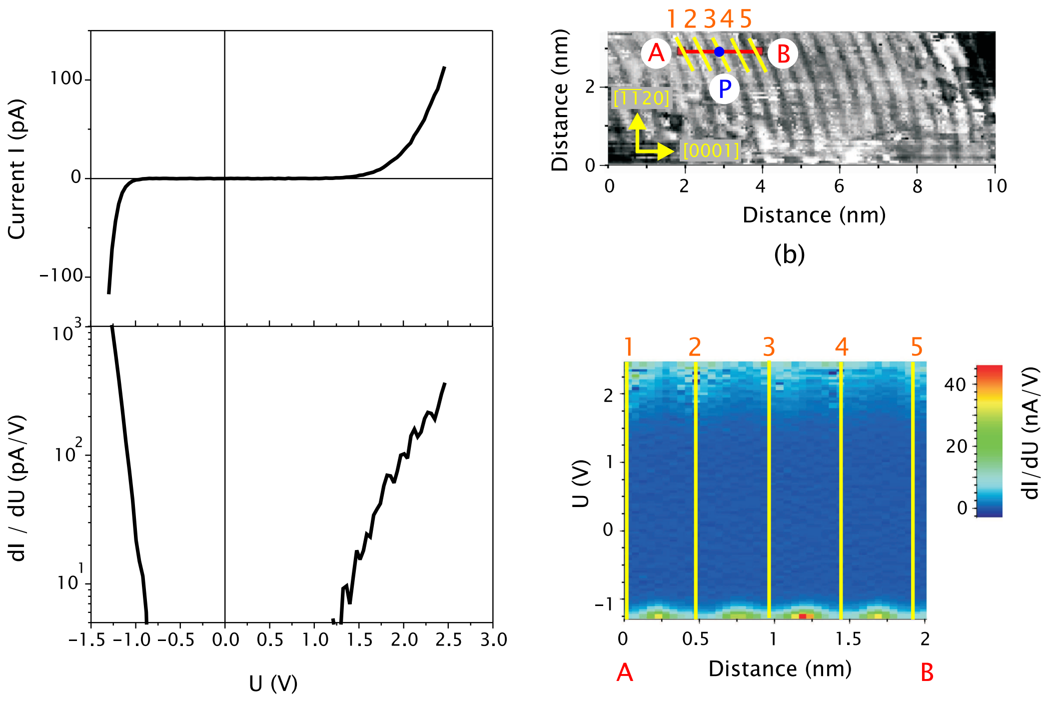

(b)

(a)

(c)

Figure 4.13: Experimental normalized STS spectra on the cleaved GaN($1\bar{1}00$) surface (sample 2007-066): (a) characteristic $I = I(U)$ and associated differential conductivity dI/dU measured on a (5 Å × 2 Å) area centered on position P of the cleaved surface; (b) empty states STM topography of a (10 nm × 3.3 nm) area of the cleaved surface (U =+2.5 V and I = 0.1 nA); (c) differential conductivity dI/dU spectrum-section along line AB.

can distinguish five tip-height maxima between the points A and B. If we denote the five maxima with yellow lines in Fig. 4.13(c), we observe in the differential conductivity spectrum that the maxima of the empty states on line AB are shifted along the [0001] direction as compared to the maxima of the filled states.

4.3 Theoretical analysis

In order to choose the best technical ingredients for studying the surfaces, the accuracy of different exchange-correlation (*xc*) functionals was evaluated: the LDA [PZ81] and the PW91 [PCV$^+$92] approximations, including in both cases the Ga-$3d$ states as valence states were considered. In Table 4.1 the ground state lattice parameters and energy-gap of the 2H-GaN polytype are listed in comparison with experimental data:

	LDA	PW91	Exp[1]
a(Å)	3.181	3.248	3.189
c(Å)	5.198	5.304	5.178
c/a	1.634	1.633	1.626
E_{gap} (eV)	1.77	1.39	3.39

Table 4.1: Calculated ground state lattice parameters and energy-gap for the 2H-GaN polytype. The values calculated in this work within the LDA and PW91 approximations are compared with the experimental data (1) taken from [Iof].

The theoretical results obtained with the two approximations agree quite well with each other and with previous calculations [SdW99]. The LDA-DFT method was applied to calculate the GaN(1$\bar{1}$00) surface properties.
The GaN(1$\bar{1}$00) surface undergoes a simple relaxation mechanism, as observed in most non-polar compound semiconductor surfaces [Duk96]. In a Cartesian coordinate system the surface plane is referred to as (xy) plane where x and y correspond to the [11$\bar{2}$0] and [0001] directions, respectively (Fig. 4.14). With respect to the ideal truncated surface, the length (l) of the Ga-N bond at the surface is reduced and a bond buckling is observed with an inward displacement (b) of the Ga-atom with respect to the N-atom. Within the LDA approximation $l =$ 1.813 Å is obtained - 6.5% reduction in bond length - and $b =$ 0.239 Å. The buckling angle between the Ga-N surface bond and the surface plane is $\omega_b =$ 7.6 degrees. In the (xy) surface plane, an in-plane displacement is observed along the y direction: N-atoms move of ≈ -0.02 Å and Ga-atoms move in the opposite direction of ≈ 0.14 Å. In agreement with previous calculations ([NN96], [SW06]),

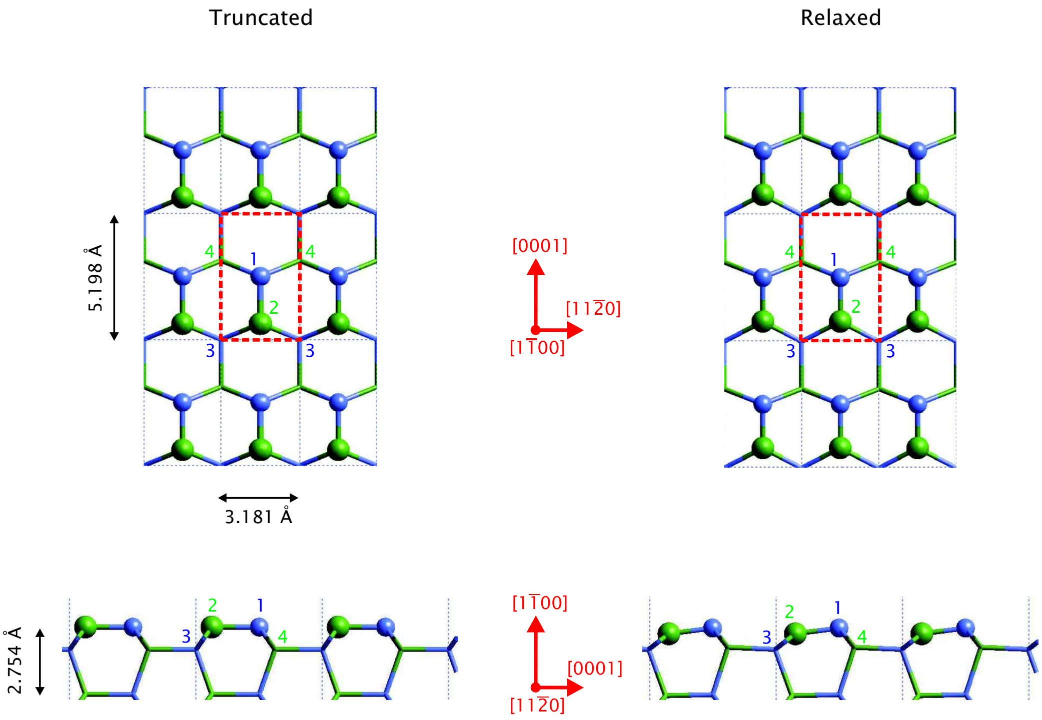

Figure 4.14: (Top image) Top view of the truncated (left) and relaxed (right) GaN(1$\bar{1}$00) surface. The surface unit cell is highlighted in red. (Bottom image) Side view of the truncated (left) and relaxed (right) GaN(1$\bar{1}$00) surface. The different planes sketched are the first surface layer, the second and third layer in the slab. Outermost N (Ga) atoms are indicated with blue (green) spheres, while atoms in the underlayer are represented with sticks of the same colors.

the LDA-DFT calculations indicate that the Ga-atom moves towards an sp^2 configuration, while the N-atom almost maintains its original position. The calculated surface bond-angles are shown in Fig. 4.15(a) and the atomic displacements of the relaxation are summarized in Table 4.2.

The surface atomic structure that was obtained is in agreement with the calculated band structure and simulated STM images, as discussed below: upon truncation, a depletion of the Ga-dangling bond with a formation of a p^* orbital and a filling of the N-dangling bond occur. The surface band structure along high symmetry lines in the 2D BZ is shown in Fig. 4.16: these bands represent the eigenvalues as calculated for a 12 layers GaN slab, at the LDA lattice parameter. In the figure, both the projected bulk band structure, and the slab calculations are reported on the same scale: alignment has been performed taking as reference the double average of

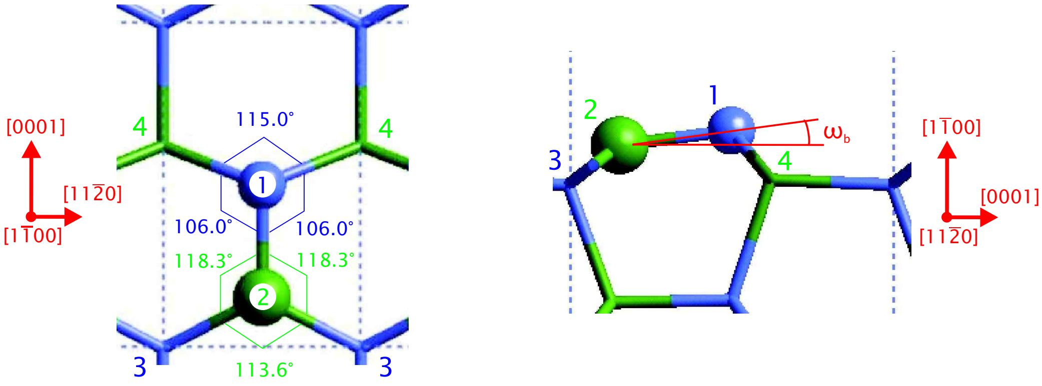

(a) (b)

Figure 4.15: Top (a) and side (b) view of the unit cell of the relaxed GaN(1$\bar{1}$00) surface. The different planes sketched are the first surface layer, the second and third layer in the slab. Outermost N (Ga) atoms are indicated with blue (green) spheres, while atoms in the underlayer are represented with sticks of the same colors.

Atom	Δ x (Å)	Δ y (Å)	Δ z (Å)
N(1)	0	-0.02	-0.03
Ga(2)	0	0.14	-0.266
N(3)	0	-0.04	-0.02
Ga(4)	0	-0.03	0.096

Table 4.2: Structural details of the relaxation for the cleaved GaN(1$\bar{1}$00) surface, as obtained from first principles calculations: the first column labels the surface atoms, in agreement with Fig. 4.14, and in the remaining columns the displacements (Δx, Δy, Δz) of each surface atom from the ideal position are indicated. The coordinate system is oriented as for Fig. 4.14 and as specified in the text.

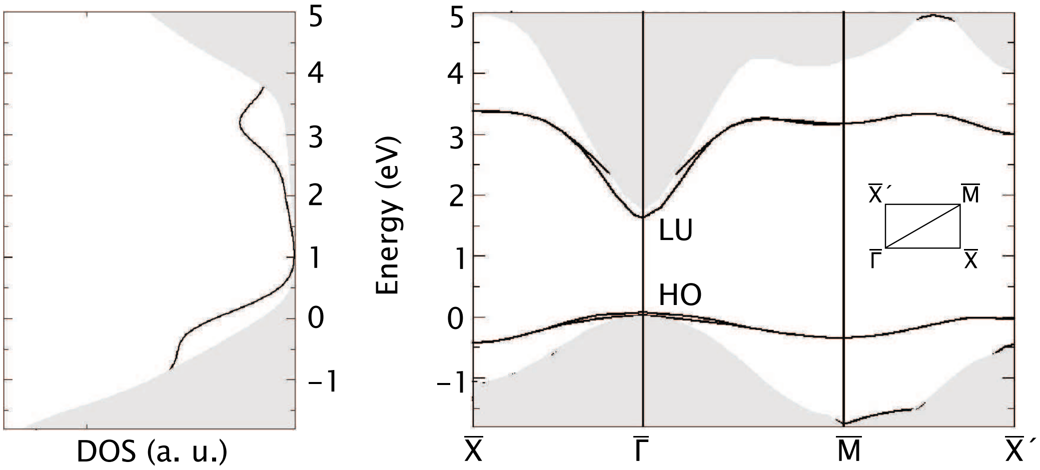

Figure 4.16: Surface DOS (left) and band structure (right) of the relaxed GaN(1$\bar{1}$00) surface. The shaded areas show the projected bulk band structure. In the inset of the surface band structure the projected 2D Brillouin zone is shown.

the total potential in the two calculations, and provides exactly the same picture as if we had taken the lowest valence states as reference for alignment. Apart from the $\bar{\Gamma}$-point, doubly degenerate N-derived HO and Ga-derived LU bands appear throughout the full BZ, as induced by the two equivalent slab surfaces. At $\bar{\Gamma}$, the bands are almost degenerate to the corresponding bulk band edges.

Another indication that both HO and LU are resonances at $\bar{\Gamma}$, rather than true surface states, comes from inspection of the charge densities of these two states. The profiles of the HO and LU charge densities along the [1$\bar{1}$00]-direction, obtained by in-plane integral on the (1$\bar{1}$00) plane, show a charge distribution within the bulk region quite homogeneously distributed with small peaks at the surface (Fig. 4.17).

The various degrees of approximations adopted allow us to confirm that the present picture is not dependent on the description that we choose for including d states in the calculation and on the chosen exchange-correlation functional. This result is consistent with the calculation of Northrup and Neugebauer [NN96], but it contradicts the picture presented by Segev and Van de Walle by use of suitably adapted pseudopotentials [SW06] (ref. Sec.2.4).

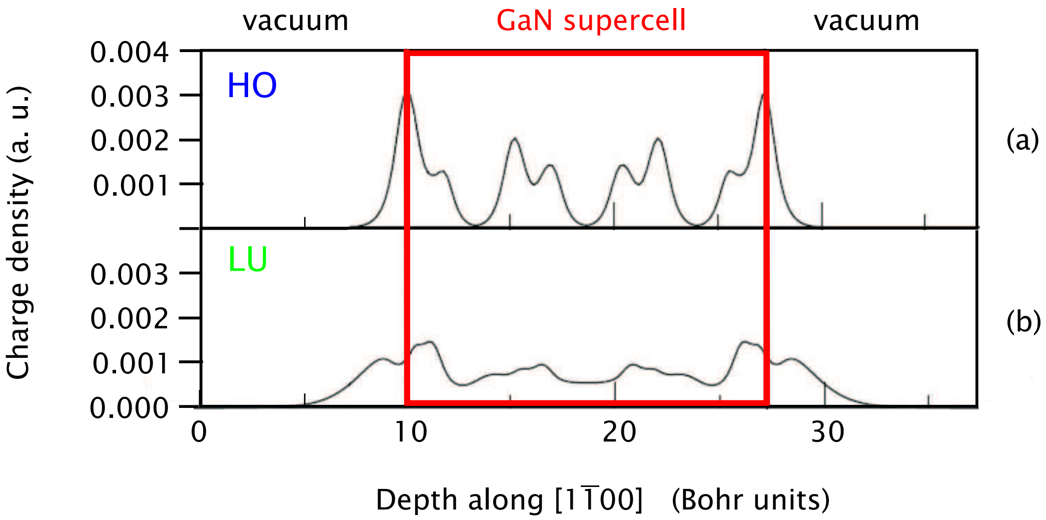

Figure 4.17: Calculated profiles of the (a) HO and (b) LU charge densities along the [1$\bar{1}$00]-direction and ortogonal to the GaN(1$\bar{1}$00) surface, as obtained by in-plane integral for a 12 layers GaN supercell.

To pursue on the comparison with the experimental STM measurements, we have computed STM images for filled and empty states in the Tersoff-Hamann approximation [TH85]. The maxima in the STM simulated filled (Fig. 4.18(a)) and empty (Fig. 4.18(b)) states topographies are localized on the N- and Ga-atoms, respectively. The filled and empty states topographies are thus fully complementary, as one can see from inspection of (Fig. 4.18(c)).

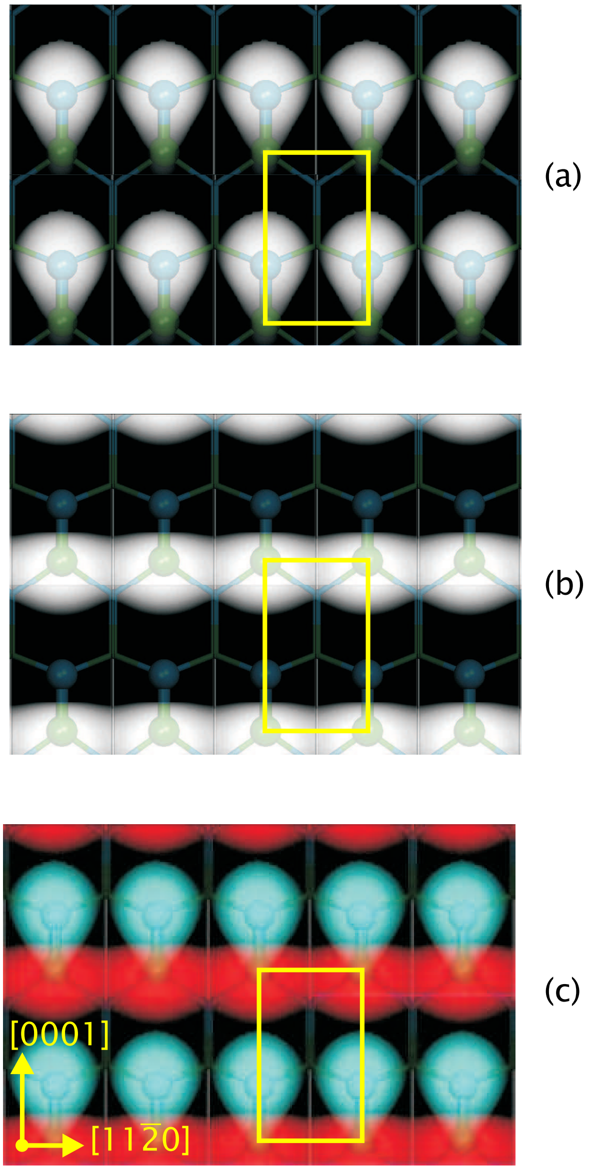

Figure 4.18: Representative simulated STM topographies for (a) filled and (b) empty states present complementary localization in space, since they are localized, respectively, on N- and Ga-atoms, as can be clearly visualized in the sum image (c). The filled (empty) states STM topography is calculated at $U_{th} = -2.5$ V ($U_{th} = +1.2$ V) from the intrinsic Fermi energy at the $\bar{\Gamma}$-point of the Brillouin zone. Outermost N (Ga) atoms are indicated with blue (green) spheres, while atoms in the first underlayer are represented with sticks of the same colors. The surface unit cell is highlighted in yellow.

4.4 Discussion

The experimental X-STM/STS data show that the cleaved GaN($1\bar{1}00$) surface does not reconstruct but simply relax, in agreement with the general trend of non-polar compound semiconductor surfaces and with the DFT calculations here discussed. Furthermore a prediction out of the theoretical results is that surface states are not present inside the energy bandgap at the center of the Brillouin zone. This result is in agreement with similar calculations by Northrup and Neugebauer [NN96] but contradicts recent theoretical findings by Segev and Van de Walle [SW06].

The model that we propose to explain the experimental data on the clean cleaved GaN($1\bar{1}00$) surface is shown in Fig. 4.19 and shows the role of the TIBB effect in the tunneling measurements. This model has already been applied for other non-polar semiconductor surfaces of n-doped bulk material, *e. g.* the GaAs(110) surface, where no surface states fall inside the energy bandgap at the center of the BZ [dRBKW02].

Due to unintentional n-doping the Fermi energy in bulk free-standing HVPE GaN samples lies close to the CBM. The work function of the tungsten tip ($\phi_T \approx 4.5$ eV) is larger than the electron affinity of the GaN sample ($\chi_S \approx \phi_S \approx 4.1$ eV), therefore at equilibrium electrons are transferred from the semiconductor GaN sample to the tip and a depletion region arises in the semiconductor close to the cleaved surface (Fig. 4.19(a)). At small positive bias no tunneling current flows between sample and tip because there are no empty states in the sample which can contribute to the tunneling process (Fig. 4.19(b)). Increasing the bias, electrons can tunnel from the Fermi energy of the tip into the Ga-like empty states of the sample (Fig. 4.19(c)). At high positive bias, the Fermi level of the sample is expected to cut the VBM (inversion) and electrons can tunnel from the tip into the N-like empty states of the sample (Fig. 4.19(d)), even though their transmission probability T (Eq. 1.6) is much lower than for electrons tunneling ouf of the Fermi energy of the tip into the Ga-like empty states of the sample.

At small negative bias no state is available for tunneling from the sample into the tip and the tunneling current is zero (Fig. 4.19(e)). At higher negative bias, an accumulation layer is formed at the sample surface and electrons tunnel from the Ga-like filled states of the sample into the empty states of the tip (Fig. 4.19(f)). At high negative bias, electrons can tunnel from the filled Ga-like and N-like surface states of the sample into the empty states of the tip (Fig. 4.19(g)).

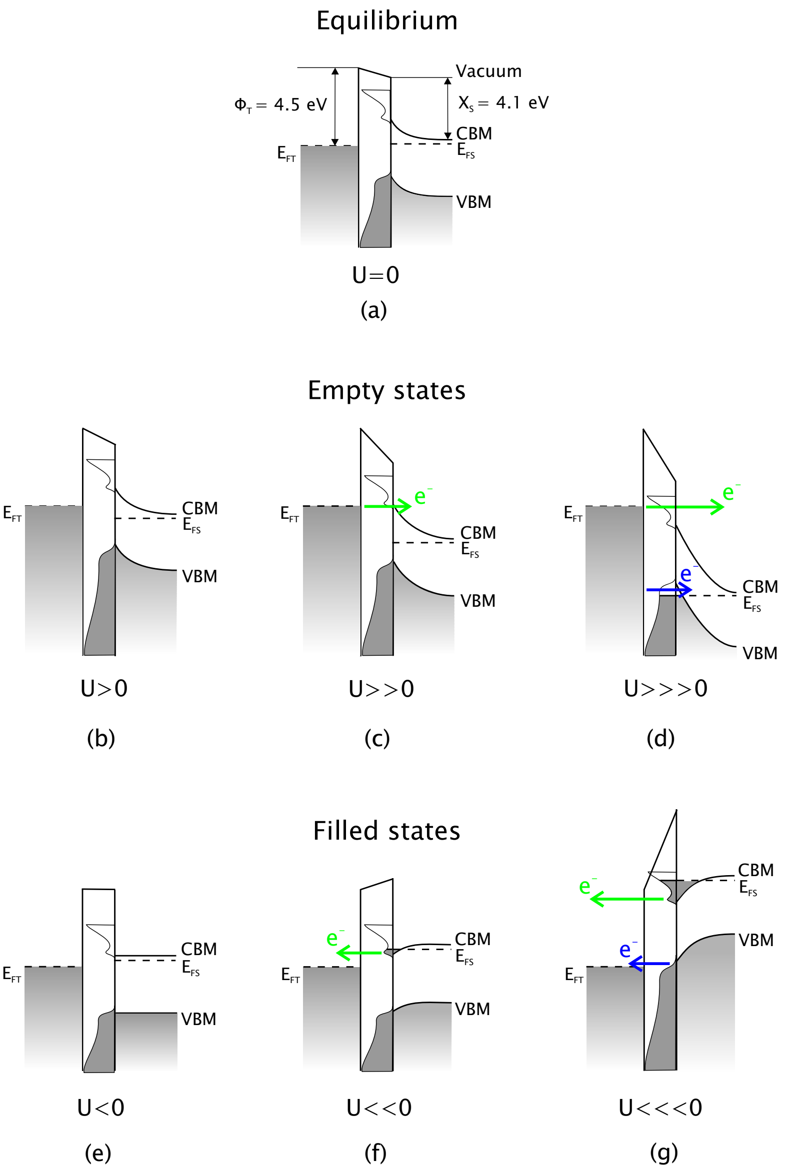

Figure 4.19: Bias dependent scheme of tunneling experiment on the clean cleaved GaN($1\bar{1}00$) surface. The position of the vacuum level at equilibrium (a) is fixed according to the workfunction of tungsten tip $\phi_T \approx 4.5$ eV and the electron affinity of GaN $\chi_S \approx \phi_S \approx 4.1$ eV (for highly unintentionally n-doped samples). The Fermi energy level of the tip and the sample are denoted with E_{FT} and E_{FS} respectively; the conduction band minimum of the sample is indicated with CBM and the valence band maximum with VBM.

According to our model, no intrinsic surface states exist inside the bandgap of the clean cleaved GaN($1\bar{1}00$) surface at the center of the BZ and the Fermi energy is not pinned. The model is supported by the experimental results shown in Figs. 4.10, 4.11 and 4.12.
The STM *multi-bias* topographies of Fig. 4.10(a)-(d) show a region of the cleaved surface of sample 2007-066 where only few surface defects are visible. Fig. 4.10(e) shows that the maxima of the filled states at $U = -1.3$ V and empty states at $U = +2.2$ V are localized at the same position along the [0001] direction. According to our model, the filled states at $U = -1.3$ V (Fig. 4.10(a)) and the empty states at $U = +2.2$ V (Fig. 4.10(c)) are Ga-like filled (Fig. 4.19(f)) and empty (Fig. 4.19(c)) surface states, respectively.
The STM *multi-bias* topographies measured on sample 2007-066 (Fig. 4.10) are consistent with the differential conductivity spectrum measured on sample 2008-004 (Fig. 4.11 (c)) which shows that the maxima of the differential conductivity are located at the same positions for filled and empty states along the [0001] direction on line AB. The maxima in the dI/dU spectrum reveal tunneling through filled ($U < 0$) and empty ($U > 0$) Ga-like surface states. The bias interval where no current flows between sample and tip (-1.6 V $\leq U \leq +0.9$V) is the region where no Ga-like states are available on the sample surface for tunneling.

The absence of intrinsic surface states inside the bandgap of the clean cleaved GaN($1\bar{1}00$) surface is furthermore supported by local $I = I(U)$ measurements on sample 2008-004 (Fig. 4.12 [Loe]). The differential conductivity spectra show that a decrease of the tip-sample distance at constant bias induces a contraction of the width of the region where no tunneling current flows between sample and tip. A similar dependence of the $I = I(U)$ spectra on tip-sample distance at constant bias has already been observed on non-polar semiconductor surfaces where no surface states fall inside the energy bandgap at the $\bar{\Gamma}$-point, like GaAs(110) [FS87] and InP(110) [ECPU92]. If an empty Ga-like surface state band would exist inside the energy bandgap at the center of the BZ as suggested by Segev and Van de Walle (Fig. 2.20), in n-doped samples at equilibrium electrons would be transferred from the bulk into this empty Ga-like band. Therefore at the clean GaN($1\bar{1}00$) surface the Fermi level should be pinned and the onset of the tunneling current for the filled states would be independent on the tip-sample distance at constant bias U_0.

The differential conductivity spectrum dI/dU measured on the cleaved GaN($1\bar{1}00$) surface of sample 2007-066 in a region with a higher concentration of surface defects than the one previously considered in Fig. 4.10

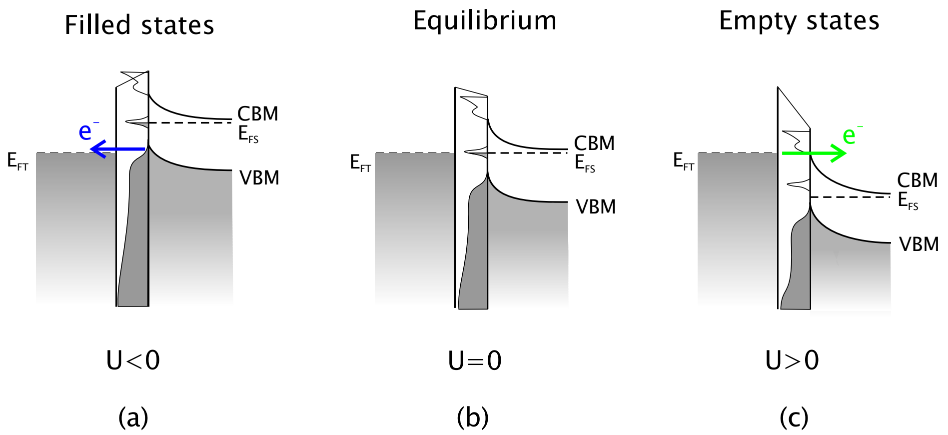

Figure 4.20: Bias dependent scheme of tunneling experiment on the cleaved GaN(1$\bar{1}$00) surface with high concentration of surface defects. The Fermi level is pinned at the surface by defect-derived surface states. The Fermi energy level of the tip and the sample are denoted with E_{FT} and E_{FS}, respectively; the conduction band minimum of the sample is indicated with CBM and the valence band maximum with VBM.

shows that the maxima of the differential conductivity are located at different positions for filled and empty states along the [0001] direction on line AB (Fig.4.13(c)). The high density of defects might be the cause of Fermi level pinning at the surface of n-doped samples by defect-derived surface states localized inside the energy bandgap (Fig. 4.20(b)) and the shift observed in the dI/dU spectrum between the maxima of filled and empty states could be assigned to tunneling of electrons out of N-like filled surface states (Fig. 4.20(a)) and into Ga-like empty surface states (Fig. 4.20(c)), respectively. However further experiments are necessary to characterize the nature and electrical properties of the observed surface defects and to check the full consistency of the model based on Fermi level pinning at the surface.

4.5 Summary and outlook

The cleaved non-polar GaN($1\bar{1}00$) surface has been studied by means of X-STM/STS measurements and *ab initio* simulations within a DFT scheme. The experimental STM topographies show an unreconstructed surface, in agreement with the theoretical calculations. The simulations show that, with respect to the ideal truncated surface, the length of the Ga-N bond at the surface is reduced and a bond buckling is observed with an inward displacement of the Ga-atom with respect to the N-atom. According to simulated STM topographies, filled and empty states are concentrated on N- and Ga-atoms, respectively.
We remind here that the calculations have been performed by M. C. Righi *et al.* and A. Catellani at the Physics Department of the Modena University and the *CNR-IMEM* in Parma (Italy), respectively. The close collaboration with many fruitful discussions between the theory and the experimental groups have added value at the STM work. The results of the simulations are included for sake of completeness in this work, with the agreement of the authors.

To explain the X-STM/STS data on the clean cleaved GaN($1\bar{1}00$) surface of unintentionally n-doped HVPE GaN samples we propose a model based on the TIBB effect: the Fermi level is not pinned at the surface and we observe in STM topographies filled and empty Ga-like surface states at bias $U = -1.3$ V and $U = +2.2$ V, respectively. This result is consistent with the theoretical calculations included in this work which predict that no surface states are found within the energy bandgap at the $\bar{\Gamma}$ point of the BZ. According to this explanation of the experimental results, STS measurements at high negative bias $U \approx -4$ V should reveal the contribution to the tunneling current of deep-lying filled N-like surface states (Fig. 4.19(g)). The challenge of this measurement depends on the possibility of collecting reliable STM/STS data at high applied bias and particularly in measuring the filled states.
With a high density of surface defects on the cleaved GaN($1\bar{1}00$) surface we observe in the differential conductivity spectrum a shift between the maxima of filled and empty states along the [0001] direction. This shift could be qualitatively explained by Fermi level pinning at the surface of n-doped samples due to the presence of defect-derived surface states, but further experiments are necessary to characterize the surface defects.
To this aim the free standing GaN HVPE *quasi*-substrates studied in this work seem to be a very good research platform, with a variety of point de-

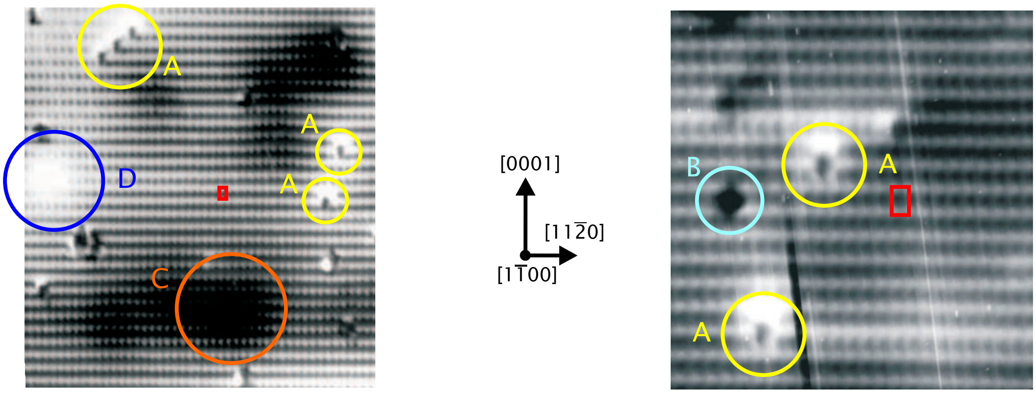

(a)

(b)

Figure 4.21: Experimental empty states STM topographies (I = 0.1 nA) of the non-polar GaN(1$\bar{1}$00) surface at applied bias (a) $U = +2.9$ V and (b) and $U = +3.6$ V. Local (A and B) and extended (C and D) defects are observed. The unit cell is highlighted in red.

fects. Fig. 4.21 shows some local and extended defetcs observed in empty states STM topographies. Localized surface defects like the ones labeled with letters A and B are clearly imagined with STM but we could still not identify the origin of them. The type A defect shows an asymmetric charge distribution along the [0001] direction, which makes a connection with the polarity of wurzitic GaN along the c-axis plausible. A detailed comparison of these first experimental data with first-principle total-energy calculations on atomic and electronic structure of bulk native defects in GaN [NdW94] should be aimed, but more experimental and theoretical work needs to be done in order to state beyond doubt the nature of these localized defects.
Fig. 4.21(a) shows also extended defects which affects the empty states STM topographies on the nm scale: the type C and D defects look like a depression and an elevation, respectively, which modulates the density of charge of the empty states topographies on some atomic raws. Similar defects have already been observed in STM topographies of the non-polar CdS(1$\bar{1}$00) surface and have been assigned to buried positively charged In dopant atoms [SDEU97].
New X-STM/STS measurements are presently performed (november 2008) in our institute by P. Loeptien in the framework of his master thesis to get further confirmation about the model that we developed to explain the experimental data on the clean cleaved GaN(1$\bar{1}$00) surface and to characterize the surface defects.

Conclusions

Non-polar SiC and GaN surfaces appear to be a really promising tool to overcome the problems that have hampered until now the full potential of SiC- and GaN-based electronic devices. 6H-SiC-based *Metal Oxide Semiconductor Field Effect Transistors* (MOSFETs) and GaN-based *Light Emitting Diodes* (LEDs) and *Laser Diodes* (LDs) are conventionally grown parallel to the c-axis and the strong internal electric fields present in these heterostructures restrain the efficiency of the device by reducing the probability of electron-hole recombination. However, it has been shown in 2000 that the problem of low bulk mobility along the c-axis in 6H-SiC MOSFETs fabricated on the (0001) Si-face can be overcome employing the $(11\bar{2}0)$ surface (a-plane) [YHKM00]. Even the problem of the so-called "green-gap" of nitride based LDs could be finally solved. The longest reported wavelength for conventional c-axis LDs is around 485 nm. Blue-green and green LDs, which would be suitable for laser color displays, portable projectors, and as replacements for solid state and gas lasers, have not yet been realized. But recently, in september 2008, Stimulated Emission (SE) in the blue-green (480 nm) and green (514 nm) regime has been observed, at room temperature under optical pumping, from non-polar m-plane $(1\bar{1}00)$ and semipolar $(11\bar{2}2)$ InGaN *Multi Quantum Wells* MQWs LD structures, respectively, grown on bulk GaN substrates [TLC$^+$08].
The availability of two inch non-polar and semipolar bulk GaN substrates is nowadays the biggest obstacle that still prevents the full development of non-polar and semi-polar nitride-based devices. But the huge potential of this new class of materials has been already demonstrated.
In view of these novel applications, the detailed description of the atomic and electronic structure of the non-polar 6H-SiC and GaN surfaces plays a key role and only few experimental results are found in literature. In this work we compare the results of experimental room-temperature *Cross-section Scanning Tunneling Microscopy and Spectroscopy* (X-STM/STS) measurements on the cleaved non-polar 6H-SiC$(11\bar{2}0)$ and GaN$(1\bar{1}00)$ surfaces with *ab initio* simulations performed in the frame of first-principles *Density*

Functional Theory (DFT). The experimental part of the work has been done in the groups of Prof. A. Rizzi and Prof. R. G. Ulbrich at the *IV. Physikalisches Institute* of the Goettingen University (Germany), while the theoretical calculations have been performed by M. C. Righi *et al.* and A. Catellani at the *Dipartimento di fisica* of the Modena University and *Centro Nazionale delle Ricerche - Istituto dei Materiali per l'Elettronica ed il Magnetismo* (CNR-IMEM) in Parma (Italy), respectively. Altough this work is mostly devoted to the X-STM/STS experiments, the theoretical simualtions have been included for the sake of comparison with the agreement of the authors.
The experimental data show that the cleaved 6H-SiC($11\bar{2}0$) and GaN($1\bar{1}00$) surfaces do not reconstruct, but simply relax. According to DFT simulations, the surface atoms move mainly along the direction ortogonal to the cleaved surface, while a depletion of the cation-dangling bonds with formation of an empty $p*$ orbital and filling of the anion-dangling bonds takes place. The empty and the filled states appear to be concetrated in the simulated STM images on cations and anions, respectively.
The X-STM/STS measurements on the freshly cleaved 6H-SiC($11\bar{2}0$) surface can consistently be explained assuming a Fermi level pinning at the surface inside the bandgap of the semiconductor for n-doped samples. The experimental STM topographies and the calculated surface band structure support a Fermi level pinning at the bottom of the Si-like surface band at the $\bar{\mathrm{X}}$-point of the *Brillouin Zone* (BZ). The tunneling process at low bias $|U|$ depends on the surface states at the border of the BZ, while at higher bias the states at the $\bar{\Gamma}$-point dominate the contours of the STM topographies.
The X-STM/STS measurements on the freshly cleaved GaN($1\bar{1}00$) surface depend strongly on the density of defects at the surface. For the clean cleaved GaN m-plane of unintentionally n-doped HVPE samples, the STS spectra show the absence of surface state bands inside the energy bandgap at the center of the BZ (as predicted by the DFT calculations) and the tunnel process is ruled by the *Tip Induced Band Bending* (TIBB) effect. On the other hand, when the cleavage results in a highly defective GaN($1\bar{1}00$) surface, Fermi level pinning at the surface takes presumably place due to defect-derived surface states which fall inside the energy bandgap. Further experimental measurements are necessary to characterize the nature and the electrical properties of these surface defects. The data presented in this work are the result of the first X-STM/STS experiments on the non-polar GaN m-plane and we hope that they can give a significant contribution to the development of non-polar nitride-based devices.

Appendix - Computational details

.1 6H-SiC(11$\bar{2}$0) surface

First principles DFT calculations were performed by using the parallel version of the ESPRESSO package [BCdGG01] and the generalized gradient approximation PW91 [PCV^{+}92] for the exchange and correlation potential. The single-particle wave functions were expanded in a plane wave basis set up to a cutoff energy of 50 Ry, and all atoms were described with norm-conserving pseudopotentials [TM91]; Brillouin-zone sums were performed by including 4 irreducible Monkhorst-Pack special k points [MP76] in the surface Brillouin Zone, which represents a converged bulk sampling [RPB^{+}02]. A periodically repeated symmetric supercell with twelve silicon carbide layers, 12 atoms per layer (6 C-atoms and 6 Si-atoms) and a 12 Å vacuum region was used to avoid interactions between replicas. This rather thick supercell was adopted to account for possible long tail reconstructions and built-in fictitious electric-fields [BCB^{+}07]. All the atoms in the slab were allowed to relax until forces were less than 10^{-3} a.u. (0.05 eV/Å) and the energy varied by less than 1 meV.

.2 GaN(1$\bar{1}$00) surface

First principles DFT calculations were performed by using the parallel version of the ESPRESSO package [BCdGG01] and testing different exchange-correlation functionals, from LDA to PW91 approximations; tests on including Hubbard [JSdW06] and GW ([ORR02],[St]) schemes were also considered. The different levels of approximation have been included to evaluate the effect of the poor description of strongly correlated, localized d-states that must be included to present a reasonable description of Ga compounds [RKP98]. This is a well-known controversial problem in DFT calculations ([JSdW06],[RKP98],[RQN^{+}05]). Wannier functions were employed to evaluate the spontaneous polarization and describe its effects at the surface [FBCN05].

The single particle wave functions were expanded in a plane wave basis set up to a cutoff energy of 70 Ry, and all atoms were described with norm-conserving pseudopotentials; Brillouin-zone sums were performed by including 16 inequivalent Monkhorst-Pack special k points in the surface Brillouin Zone. A periodically repeated symmetric supercell with twelve gallium nitride layers, 2 atoms per layer (1 Ga-atom and 1 N-atom) and a 19 Å vacuum region was used, to avoid interactions between replicas. This treatment is perfectly consistent to the one adopted in the description of SiC(1$\bar{1}$00) surfaces [BCB+07], thus comparisons can be drawn. This rather thick supercell was adopted to account for possible long tail reconstructions and built-in fictitious electric-fields [BCB+07]. All the atoms in the slab were allowed to relax until forces were less than 10-3 a.u. (0.05 eV/Å) and the energy varied by less than 1 meV.

A rigorous estimate of the errors and approximations must be performed concerning the degeneracy of the filled and empty surface state bands with the corresponding bulk band edges at the $\bar{\Gamma}$-point (ref. Fig. 4.16). First of all the alignment procedure used to compare the two different sets of calculations, the one for bulk and those for the slab. Alignment has been performed taking as reference the double average of the total potential in the two calculations: this corresponds to an error of about (less than) 10 meV in the eigenvalue position, because of accuracy in the averaging procedure. Furthermore, the observed breaking in degeneracy at $\bar{\Gamma}$, as is induced by long eigenvector tails at this point in the Brillouin zone: we have considered slabs of different thickness, to estimate the decaying behaviour of the related error, which again gives us something like 10 meV. Thus we may say that the position of the HO and LU states with respect to the projected bulk band structure is affected by 20 meV maximum error. In the present situation, the plot reported in Fig. 4.16 shows LU laying 14 meV below the conduction band bottom, that is degenerate within our accuracy.

List of abbreviations

AFM	Atomic Force Microscopy
BZ	Brillouin Zone
CBM	Conduction Band Minimum
DFT	Density Functional Theory
DOS	Density Of States
DVD	Digital Video Disc
FWHM	Full Width at Half Maximum
GaN	Gallium nitride
HO	Highest Occupied
HVPE	Hydride Vapor Phase Epitaxy
LD	Laser Diode
LDA	Local Density Approximation
LDOS	Local Density Of States
LED	Light Emitting Diode
LU	Lowest Unoccupied
MBE	Molecular Beam Epitaxy
MOCVD	Metal Oganic Chemical Vapor Deposition
MOSFET	Metal Oxide Field Effect Transistor
PL	Photoluminescence
QE	Quantum Efficiency
QW	Quantum Well
SiC	Silicon Carbide
STM	Scanning Tunneling Microscopy
STS	Scanning Tunneling Spectroscopy
TEM	Transmission Electron Microscopy
TH	Tersoff and Hamann
TIBB	Tip Induced Band Bending
UHV	Ultra High Vacuum
VBM	Valence Band Maximum
XRD	X-Ray Diffraction
X-STM	Cross Section Scanning Tunneling Microscopy
X-STS	Cross Section Scanning Tunneling Spectroscopy

117

Bibliography

[ACY$^+$03] V. Adivarahan, C. Chen, J. Yang, M. Gaevski, M. Shatalov, G. Simin, and M. A. Khan. Planar Schottky Diodes on High Quality a-plane GaN. *Jpn. J. Appl. Phys.*, 42:L1136, 2003.

[Amb98] O. Ambacher. Growth and applications of Group III-nitrides. *J. of Physics D: Applied Physics*, 31:2653, 1998.

[Bar61] J. Bardeen. Tunneling from a many-particle point of view. *Appl. Phys. Lett.*, 6:57, 1961.

[BCB$^+$07] G. P. Brandino, G. Cicero, B. Bonferroni, A. Ferretti, A. Calzolari, C. M. Bertoni, and A. Catellani. Polarization properties of $(1\bar{1}00)$ and $(11\bar{2}0)$ SiC surfaces from first principles. *Phys. Rev. B*, 76:085322, 2007.

[BCdGG01] S. Baroni, A. Dal Corso, S. de Gironcoli, and P. Giannozzi. http://www.pwscf.org, 2001.

[Bes87] K. Besocke. An easily operable Scanning Tunneling Microscope. *Surface Science*, 181:145, 1987.

[BFV97] F. Bernardini, V. Fiorentini, and D. Vanderbilt. Spontaneous polarization and piezoelectric constants of III-V nitrides. *Phys. Rew. B*, 56:R10024, 1997.

[BHW$^+$07] M. Bertelli, J. Homoth, M. Wenderoth, A. Rizzi, R. G. Ulbrich, M. C. Righi, C. M. Bertoni, and A. Catellani. Atomic and electronic structure of the cleaved 6H-SiC$(11\bar{2}0)$ surface. *Phys. Rev. B*, 75:165312, 2007.

[BHWP$^+$92] V. Bressler-Hill, M. Wassermeier, K. Pond, G. A. D. Briggs R. Maboudian, P. M. Petroff, and W. H. Weinberg. Atom-resolved imaging and spectroscopy on the GaAs(001) surface using tunneling microscopy. *J. Vac. Sci. Technol. B*, 10:1881, 1992.

[Bic] M. Bickermann. http://servww6.ww.uni-erlangen.de/∼bicki/e-index.html. Erlangen University, Germany.

[BRGW82] G. Binnig, H. Rohrer, Ch. Gerber, and E. Weibel. Tunneling through a controllable vacuum gap. *Appl. Phys. Lett.*, 40:178, 1982.

[CCG06] A. Catellani, G. Cicero, and G. Galli. Wetting behavior of low-index cubic SiC surfaces. *J. Chem. Phys.*, 124:024707, 2006.

[Cen] The Cambridge Crystallographic Data Centre. http://www.ccdc.cam.ac.uk/index.php.

[CGGP98] A. Catellani, G. Galli, F. Gygi, and F. Pellacini. Influence of stress and defects on the silicon-terminated SiC(001) surface structure. *Phys. Rev. B*, 57:12255, 1998.

[Cha89] D. J. Chadi. Atomic Structure of Reconstructed Group IV and III-V Semiconductor Surfaces. *Ultramicroscopy*, 31:1, 1989.

[Che88] C. Julian Chen. Theory of scanning tunneling microscopy. *J. Vac. Sci. Technol. A*, 6:319, 1988.

[Che91] C. Julian Chen. Microscopic view of scanning tunneling spectroscopy. *J. Vac. Sci. Technol. A*, 9:44, 1991.

[Che93] C. Julian Chen. *Introduction to Scanning Tunneling Microscopy*. Oxford University Press, 1993.

[CLW$^+$02] M. D. Craven, S. H. Lim, F. Wu, J. S. Speck, and S. P. DenBaars. Threading dislocation reduction via laterally overgrown nonpolar $(11\bar{2}0)$ a-plane GaN. *Appl. Phys. Lett.*, 81:1200, 2002.

[CM07] R. Calarco and M. Marso. GaN and InN nanowires grown by MBE: A comparison. *Appl. Phys. A*, 87:499, 2007.

[DKE$^+$02] V. Yu. Davydov, A. A. Klochikhin, V. V. Emtsev, D. A. Kurdyukov, S. V. Ivanov, V. A. Vekshin, J. Furthmueller F. Bechstedt, J. Aderhold, J. Graul, A. V. Mudryi, H. Harima, A. Hashimoto, A. Yamamoto, and E. E. Haller. Band Gap of Hexagonal InN and InGaN alloys. *Phys. Stat. Sol. (b)*, 234:787, 2002.

[dPHM+98] A. L. Vázquez de Parga, O. S. Hernán, R. Miranda, A. Levy Yeyati, N. Mingo, A. Martín-Rodero, and F. Flores. Electron Resonances in Sharp Tips and Their Role in Tunneling Spectroscopy. *Phys. Rev. Lett.*, 80:357, 1998.

[dR01] G. J. de Raad. *Voltage-dependent Scanning Tunneling Microscopy on the (110)-surfaces of GaAs, AlGaAs, and their heterostructures*. PhD thesis, Technical University of Eindhoven, 2001.

[dRBKW02] G. J. de Raad, D. M. Bruls, P. M. Koenraad, and J. H. Wolter. Interplay between tip-induced band bending and voltage-dependent surface corrugation on GaAs(110) surfaces. *Phys. Rev. B*, 66:195306, 2002.

[Duk93] C. B. Duke. Surface structures of tetrahedrally coordinated semiconductors: principles, practice, and universality. *Appl. Surf. Sc.*, 65/66:543, 1993.

[Duk96] C. B. Duke. *Handbook of Surface Science, Physical Structure*, page 229. Elsevier Science, 1996.

[ECPU92] Ph. Ebert, G. Coc, U. Poppe, and K. Urban. The electronic structure of the InP(110) surface studied by scanning tunneling microscopy and spectroscopy. *Surface Science*, 271:587, 1992.

[Edg94] J. H. Edgar. *Group III Nitrides*. London: INSPEC, 1994.

[End97] R. Enderlein. *Fundamentals of semiconductor physics and devices*, page 334. World Scientific, 1997.

[FBCN05] A. Ferretti, B. Bonferroni, A. Calzolari, and M. Buongiorno Nardelli. WanT code. *http://www.wannier-transport.org*, 2005.

[FKM+08] K. Fujito, K. Kiyomi, T. Mochizuki, H. Oota, H. Namita, S. Nagao, and I. Fujimura. High-quality nonpolar m-plane GaN substrates grown by HVPE. *Phys. Stat. Sol. (a)*, 205:1056, 2008.

[FMS93] V. Fiorentini, M. Methfessel, and M. Scheffler. Electronic and structural properties of GaN by the full-potential linear muffin-tin orbitals method: The role of the d electrons. *Phys. Rev. B*, 47:13353, 1993.

[fO] Institut für Optoelektronik. Universität Ulm, Germany.

[FRBA$^+$05] S. Founta, F. Rol, E. Bellet-Amalric, J. Bleuse, B. Daudin, B. Gayral, and H. Mariette. Optical properties of GaN quantum dots grown on nonpolar $(11\bar{2}0)$ SiC by molecular-beam epitaxy. *Appl. Phys. Lett.*, 86:171901, 2005.

[FS87] R. M. Feenstra and J. A. Stroscio. Tunneling Spectroscopy of the GaAs(110) surface. *J. Vac. Sci. Technol. B*, 5:923, 1987.

[FSF87] R. M. Feenstra, J. A. Stroscio, and A. P. Fein. Tunneling Spectroscopy of the Si(111) 2x1 Surface. *Surface Science*, 181:295, 1987.

[Gar05] J. Garleff. *Quasi-eindimensionale elektronische Zustände auf der Si(111)-2x1-Oberfläche*. PhD thesis, Göttingen University, Germany, 2005.

[GC93] A. Garcia and M. L. Cohen. First-principles ionicity scale. Charge asymmetry in the solid state. *Phys. Rev. B*, 47:13367, 1993.

[GK90] J. E. Griffith and G. P. Kochanski. Scanning tunneling microscopy. *Annual Reviews Materials Science*, 20:219, 1990.

[GL04] A. Ghatak and S. Lokanathan. *Quantum mechanics: Theory and Applications*, page 423. Kluwer Academic Publishers, 2004.

[Ham89] R. J. Hamers. Atomic-resolution surface spectroscopy with the scanning tunneling microscope. *Annu. Rev. Phys. Chem.*, 40:531, 1989.

[Har02] H. Harima. Properties of GaN and related compounds studied by means of Raman scattering. *J. Phys.: Condens. Matter*, 14:R967, 2002.

[HCW$^+$05] B. A. Haskell, A. Chakraborty, F. Wu, H. Sasano, P. T. Fini, S. P. Denbaars, J. S. Speck, and S. Nakamura. Microstructure and Enhanced Morphology of Planar Nonpolar m-Plane GaN Grown by Hydride Vapor Phase Epitaxy. *J. of ELECTRONIC MATERIALS*, 34:4, 2005.

[Hei98] A. J. Heinrich. *Ordering in Ternary Compound Semiconductors on the Atomic Scale*. PhD thesis, Göttingen University, Germany, 1998.

[HNU95] H. Harima, S. Nakashima, and T. Uemura. Raman scattering from anisotropic LO-phonon–plasmon–coupled mode in n-type 4H– and 6H–SiC. *J. Appl. Phys.*, 78:1996, 1995.

[Iof] Ioffe Institute. www.ioffe.ru.

[JPZ96] J. E. Jaffe, R. Pandey, and P. Zapol. *Ab initio* predictions of GaN($10\bar{1}0$) and (110) anomalous surface relaxation. *Phys. Rev. B*, 53:R4209, 1996.

[JSdW06] A. Janotti, D. Segev, and C. G. Van de Walle. Effects of cation d states on the structural and electronic properties of III-nitride and II-oxide wide-band-gap semiconductors. *Phys. Rev. B*, 74:045202, 2006.

[KD02] A. Krost and A. Dadgar. GaN-Based Devices on Si. *Phys. Stat. Sol. (a)*, 194:361, 2002.

[KFK$^+$08] K. Kojima, M. Funato, Y. Kawakami, H. Braun, U. Schwarz, S. Nagahama, and T. Mukai. Inhomogeneously broadened optical gain spectra of InGaN quantum well laser diodes. *Phys. Stat. Sol. (c)*, 5:2126, 2008.

[KSS$^+$07] K.-C. Kim, M. C. Schmidt, H. Sato, F. Wu, N. Fellows, M. Saito, K. Fujito, J. S. Speck, S. Nakamura, and S. P. DenBaars. Improved electroluminescence on nonpolar m-plane InGaN/GaN quantum wells LEDs. *Phys. Stat. Sol. (RRL)*, 1:125, 2007.

[LÖ1] H. Lüth. *Solid Surfaces, Interfaces and Thin Films*, page 265. Springer, 2001.

[LE02] L. Liu and J. H. Edgar. Substrates for gallium nitride epitaxy. *Materials Science and Engineering R*, 37:61, 2002.

[Lel55] J. A. Lely. Darstellung von Einkristallen von Silicium Carbid und Beherrschung von Art und Menge der eingebauten Verunreinigungen. *Ber. Dt. Keram. Ges.*, 8:229, 1955.

[LM97] D. C. Look and R. J. Molnar. Degenerate layer at GaN/sapphire interface: Influence on Hall-effect measurements. *Appl. Phys. Lett.*, 70:3377, 1997.

[LMP$^+$03] D. C. Look, R. J. Molnar, S. S. Park, S. K. Lee, and J. Y. Han. Ga vacancies as dominant intrinsic acceptors in GaN grown by hydride vapor phase epitaxy. *Appl. Phys. Lett*, 82:3433, 2003.

[Loe] P. Loeptien. Private communication.

[Lot04] S. Loth. Rastertunnelspektroskopie in einzelnen Akzeptoren in GaAs. Diplomarbeit, Göttingen University, Germany, 2004.

[Lot07] S. Loth. *Atomic scale images of acceptors in III-V semiconductors: band bending, tunneling paths and wave functions*. PhD thesis, Göttingen University, Germany, 2007.

[LSM$^+$01] D. C. Look, C. E. Stutz, R. J. Molnar, K. Saarinen, and Z. Liliental-Weber. Dislocation-independent mobility in lattice-mismatched epitaxy: application to GaN. *Solid State Comm.*, 117:571, 2001.

[Luc04] A. Lucier. Preparation and Characterization of Tungsten Tips Suitable for Molecular Electronic Studies. Master's thesis, McGill University of Montreal, Quebec, Canada, 2004.

[MHCH93] M. McEllistrem, G. Haase, D. Chen, and R. J. Hamers. Electrostatic Sample-Tip interactions in the Scanning Tunneling Microscope. *Phys. Rev. Lett.*, 70:2471, 1993.

[MKAS99] C. R. Miskys, M. K. Kelly, O. Ambacher, and M. Stutzmann. MOCVD-Epitaxy on Free-Standing HVPE-GaN Substrates. *Phys. Stat. Sol. (a)*, 176:443, 1999.

[MKAS03] C. R. Miskys, M. K. Kelly, O. Ambacher, and M. Stutzmann. Freestanding GaN-substrates and devices. *Phys. Stat. Sol. (c)*, 6:1627, 2003.

[MP76] H. J. Monkhorst and J. D. Pack. Special points for Brillouin-zone integrations. *Phys. Rev. B*, 13:5188, 1976.

[MSG$^+$94] H. Morkoç, S. Strite, G. B. Gao, M. E. Lin, B. Sverdlov, and M. Burns. Large-band-gap SiC, III-V nitride, and II-VI Zn-Se-based semiconductor device technologies. *J. of Appl. Phys.*, 76:1363, 1994.

[MT69] H. P. Maruska and J. J. Titjen. The preparation and properties of vapor-deposited single-crystalline GaN. *Appl. Phys. Lett.*, 15:327, 1969.

[NdW94] J. Neugebauer and C. G. Van de Walle. Atomic geometry and electronic structure of native defects in GaN. *Phys. Rev. B*, 50:8067, 1994.

[NH97] S. Nakashima and H. Harima. Raman Investigation of SiC Polytypes. *Phys. Stat. Sol. (a)*, 162:39, 1997.

[NN96] J. E. Northrup and J. Neugebauer. Theory of GaN($10\bar{1}0$) and ($11\bar{2}0$) surfaces. *Phys. Rev. B*, 53:R10477, 1996.

[Nog00] C. Noguez. Origin of optical anisotropies of nonpolar GaN surfaces. *Phys. Rev. B*, 62:2681, 2000.

[NSC$^+$08] P. G. Neudeck, D. J. Spry, L. Y. Chen, G. M. Beheim, R. S. Okojie, C. W. Chang, R. D. Meredith, T. L. Ferrier, L. J. Evans, M. J. Krasowski, and N. F. Prokop. Stable electrical operation of 6H-SiC JFETs and ICs for thousands of hours at 500 degrees C. *IEEE ELECTRON DEVICE LETTERS*, 29:456, 2008.

[Nye57] J. F. Nye. *Physical Properties of Crystals*. Oxford University Press, 1957.

[OFS$^+$98a] S. K. O'Leary, B. E. Foutz, M. S. Shur, U. V. Bhapkar, and L. F. Eastman. Electron transport in wurtzite indium nitride. *J. Appl. Phys.*, 83:826, 1998.

[OFS$^+$98b] S. K. O'Leary, B. E. Foutz, M. S. Shur, U. V. Bhapkar, and L. F. Eastman. Monte Carlo simulation of electron transport in wurtzit aluminium nitride. *Solid State Comm.*, 105:621, 1998.

[ORR02] G. Onida, L. Reining, and A. Rubio. Electronic excitations: density-functional versus many-body Green's-function approaches. *Rev. Mod. Phys.*, 74:601, 2002.

[OT90] S. Ohnishi and M. Tsukada. Effect of the microscopic electronic states of the tip on the scanning tunneling microscopy image. *J. Vac. Sci. Technol. A*, 8:174, 1990.

[OTK08] K. Okamoto, T. Tanaka, and M. Kubota. High-Efficiency Continuous-Wave Operation of Blue-Green Laser Diodes Based on Nonpolar m-Plane Gallium Nitride. *Appl. Phys. Exp.*, 1:072201, 2008.

[Pau32] L. Pauling. The Nature of the Chemical Bond. The Energy of Single Bonds and the Relative Electronegativity of Atoms. *J. Am. Chem. Soc.*, 54:3570, 1932.

[PCV$^+$92] J. P. Perdew, J. A. Chevary, S. H. Vosko, K. A. Jackson, M. R. Pederson, D. J. Singh, and C. Fiolhais. Atoms, molecules, solids, and surfaces: Applications of the generalized gradient approximation for exchange and correlation. *Phys. Rev. B*, 46:6671, 1992.

[Pin] A. B. Pinto. Private communication.

[PKR$^+$96] J. Pollmann, P. Krüger, M. Rohlfing, M. Sabisch, and D. Vogel. *Ab initio* calculations of structural and electronic properties of prototype surfaces of group IV, III-V and II-VI semiconductors. *Appl. Surf. Sci.*, 104:1, 1996.

[PKS97] J. Pollmann, P. Krüger, and M. Sabisch. Atomic and Electronic Structure of SiC Surfaces from ab-initio calculations. *Phys. Stat. Sol. (b)*, 202, 1997.

[Por96] S. Porowski. High pressure growth of GaN - new prospects for blue lasers. *J. of Crys. Growth*, 166:583, 1996.

[PZ81] J. P. Perdew and A. Zunger. Self-interaction correction to density-functional approximations for many-electrons systems. *Phys. Rev. B*, 23:5048, 1981.

[Qua95] T. Quast. Topographie von Goldschichten auf Glimmersubstrat. Diplomarbeit, Göttingen University, Germany, 1995.

[RDH01] E. Rauls, P. Deák, and Z. Hajnal. Theoretical study of the nonpolar surfaces and their oxygen passivation in 4H- and 6H-SiC. *Phys. Rew. B*, 64:245323, 2001.

[Rei97] L. Reimer. *Transmission Electron Microscopy*, page 364. Springer, 1997.

[rF89] P. Mårtensson and R. M. Feenstra. Geometric and electronic structure of antimony on the GaAs(110) surface studied by scanning tunneling microscopy. *Phys. Rev. B*, 39:7744, 1989.

[Rig03] M. C. Righi. *First-principles studies on the homoepitaxial growth of SiC*. PhD thesis, Universitá degli studi di Modena e Reggio Emilia, Italy, 2003.

[RKP98] M. Rohlfing, P. Krüger, and J. Pollmann. Role of semicore d electrons in quasiparticle band-structure calculations. *Phys. Rev. B*, 57:6485, 1998.

[RPB$^+$02] M. C. Righi, C. A. Pignedoli, G. Borghi, R. Di Felice, and C. M. Bertoni. Surface-induced stacking transition at SiC(0001). *Phys. Rev. B*, 66:045320, 2002.

[RQN$^+$05] P. Rinke, A. Qteish, J. Neugebauer, C. Freysoldt, and M. Scheffler. Combining GW calculations with exact-exchange density-functional theory: an analysis of valence-band photoemission for compound semiconductors. *New J. Phys.*, 7:126, 2005.

[Sch06] H. Schleiermacher. Charakterisierung von Spitzen für die Rastertunnelmikroskopie. Bericht über das Praxissemester, Göttingen University, Germany, 2006.

[SDEU97] B. Siemens, C. Domke, Ph. Ebert, and K. Urban. Electronic structure of wurtzite II-VI compound semiconductor cleavage surfaces studied by scannig tunneling microscopy. *Phys. Rev. B*, 56:12321, 1997.

[SdW99] C. Stampfl and C. G. Van de Walle. Density-functional calculations for III-V nitrides using the local-density approximation and the generalized gradient approximation. *Phys. Rev. B*, 59:5521, 1999.

[SFF86] J. A. Stroscio, R. M. Feenstra, and A. P. Fein. Electronic structure of the Si(111)2×1 Surface by Scanning Tunneling Microscope. *Phys. Rew. Lett.*, 57:2579, 1986.

[SGS$^+$05] T. Seyller, R. Graupner, N. Sieber, K. V. Emtsev, A. Tadich L. Ley, J. D. Riley, and R. C. G. Leckey. Hydrogen terminated

4H-SiC{$1\bar{1}00$} and {$11\bar{2}0$} surfaces studied by synchrotron x-ray photoelectron spectroscopy. *Phys. Rev. B*, 71:245333, 2005.

[SK07] U. T. Schwarz and M. Kneissl. Nitride emitters go nonpolar. *Phys. Stat. Sol. (RRL)*, 1:A44, 2007.

[SKP95] M. Sabisch, P. Krüger, and J. Pollmann. *Ab initio* calculations of SiC(110) and GaAs(110) surfaces: A comparative study and the role of ionicity. *Phys. Rev. B*, 51:13367, 1995.

[Smi78] R. A. Smith. *Semiconductors*, pages 86–92. Cambridge University Press, 1978.

[SPC92] W. Suttrop, G. Pensl, and W. J. Choyke. Hall effect and infrared absorption measurements on nitrogen donors in 6H-silicon carbide. *J. Appl. Phys.*, 72, 1992.

[St] L. Martin Samos and A. Ferretti *et al.* SAX code. www.sax.org.

[Sta14] J. Stark. Beobachtungen über den Effekt des elektrischen Feldes auf Spektrallinien I. Quereffekt. *Annalen der Physik*, 43:965, 1914.

[SW06] D. Segev and C. G. Van De Walle. Origins of Fermi-level pinning on GaN and InN polar and nonpolar surfaces. *Europhys. Lett.*, 76:305, 2006.

[SYJ00] M. Syväjärvi, R. Yakimova, and E. Janzen. Cross-sectional cleavages of SiC for evaluation of epitaxial layers. *J. of Crys. Growth*, 208:409, 2000.

[Tei07] K. Teichmann. Rastertunnelspektroskopie an Silizium-Donatoren in Galliumarsenid. Diplomarbeit, Göttingen University, Germany, 2007.

[TH83] J. Tersoff and D. R. Hamann. Theory and applications for the scanning tunneling microscopy. *Phys. Rev. Lett.*, 50(25):1998, 1983.

[TH85] J. Tersoff and D. R. Hamann. Theory of the scanning tunneling microscope. *Phys. Rev. B*, 31:805, 1985.

[The] The Solid State Lighting & Display Center, College of Engineering, University of California, Santa Barbara. $http://ssldc.ucsb.edu/index.php$.

[TLC+08] A. Tyagi, Y. D. Lin, D. A. Cohen, M. Saito, K. Fujito, J. S. Speck, S. P. DenBaars, and S. Nakamura. Stimulated Emission at Blue-Green (480 nm) and Green (514 nm) Wavelengths from Nonpolar m-plane ($1\bar{1}00$) and Semipolar ($11\bar{2}2$) InGaN Multiple Quantum Well Laser Diode Structures. *Appl. Phys. Exp.*, 1:091103, 2008.

[TM91] N. Troullier and J. L. Martins. Efficient pseudopotentials for plane-wave calculations. *Phys. Rev. B*, 43:1993, 1991.

[TT78] Y. M. Tairov and V. F. Tsvetkov. Investigation of growth processe of ingots of silicon carbide single crystals. *J. of Crys. Growth*, 43:209, 1978.

[Ukr96] V. A. Ukraintsev. Data evaluation technique for electron-tunneling spectroscopy. *Phys. Rev. B*, 53:11176, 1996.

[Une96] W. N. Unertl. *Handbook of Surface Science, Physical Structure*, page 3. Elsevier Science, 1996.

[Urb] A. Urban. Private communication.

[VJ03] C. Virojanadara and L. I. Johansson. Photoemission study of clean and oxidized nonpolar 4H-SiC surfaces. *Phys. Rev. B*, 68:125314, 2003.

[VV] AA. VV. $http://en.wikipedia.org/wiki/blu-ray_disc$.

[WBT+00] P. Waltereit, O. Brandt, A. Trampert, H. T. Grahn, J. Menniger, M. Ramsteiner, M. Reiche, and K. H. Ploog. Nitride semiconductors free of electrostatic fields for efficient white light-emitting diodes. *Nature*, 406:865, 2000.

[Wie94] R. Wiesendanger. *Scanning Probe Microscopy and Spectroscopy*. Cambridge University Press, 1994.

[WWB+89] J. Wintterlin, J. Wiechers, H. Brune, T. Gritsch, H. Hofer, and R. J. Behm. Atomic-Resolution Imaging of Close-Packed Metal Surfaces by Scanning Tunneling Microscopy. *Phys. Rev. Lett.*, 62:59, 1989.

[YHKM00] H. Yano, T. Hirao, T. Kimoto, and H. Matsunami. High Channel Mobility in Inversion Layer of SiC MOSFETs for Power Switching Transistors. *Jpn. J. Appl. Phys. Part 1*, 39:2008, 2000.

[YLFZ92] C. Y. Yeh, Z.W. Lu, S. Froyen, and A. Zunger. Zincblende–wurtzite polytypism in semiconductors. *Phys. Rev. B*, 46:10086, 1992.

[Zen] J. Zenneck. Private communication.

Acknowledgements

I would like to thank all the people who supported me during this work:

- Prof. Dr. Angela Rizzi for the opportunity to make a Ph. D. work at the Göttingen University and the fruitful discussions on the experimental data. Her new ideas for developing the project and constant motivation during the work gave a remarkable contribution to reach the aims of this study.
- Prof. Dr. Rainer G. Ulbrich for the cooperation with his group and the opportunity to speak together about scientific topics.
- Prof. Dr. Friedhelm Bechstedt for kindly accepting to be reviewer of this work.
- Dr. Martin Wenderoth for the useful discussions about the evaluation and interpreation of the experimental data.
- Dr. Alessandra Catellani, Dr. Maria C. Righi, Prof. Dr. Carlo M. Bertoni, Dr. Andrea Ferretti and Dr. Laila Martin Samos for the DFT calculations which are included in this thesis and which gave a significant contribution to enrich the interpretation of the experimental results.
- Dr. Jörg Malindretos for the conversations on physics topics and the notable help in learning how to use new software programs.
- Dr. Martin Kočan for fruitful discussions on nitride science and didactic material for the students of the *Anfängerpraktikum*.
- Dr. Jan Zenneck for the Raman and XRD measurements. With Jan I shared all my time from the beginning in 2003. He survived my pasta and I thank him for this.
- all the people of the MBE group of the fourth physical institute of the faculty of physics in Goettingen University, for the nice time we

spent together in the work and out of it. I am grateful to Amilcar B. Pinto for the Hall-effect measurements and to Arne Urban for the TEM images which are presented in this work. Thanks to Dong-Du Mai and Martin Röver fot the help with the LaTeX code, to Christian Denker, Boris Landgraf and Michael Carsten for useful suggestions in improving the text of the Ph. D. thesis. I am grateful to Peter Löptien for some of the STS spectra which are discussed in this work. I wish him all the best in carrying on the project on GaN and for his master thesis.

- all the students and doctoral candidates of the STM group who helped me during these years in learning how to use the experimental set-up and the software to evaluate the data. They shared with me their experience on cleavage and STM investigation of semiconductor materials and this knowledge helped me to develop the project on GaN.
- the people of the technical workshops of the fourth physical institute and Dipl. Ing. Bernhard Spicher for his great help in solving problems with the experimental set-up and for teaching me many new things about vacuum technology.
- Dr. Karl Ahlborn, Natascha Schneider and Antje Spliethoff-Laiser, who always helped me to face administrative tasks making them easier and simple.
- the *Virtuelle Institut für SpinELektronik* (VISEL) and *Land Niedersachsen* for financial support.

Curriculum vitae

Name	Marco Bertelli
Date of birth	17.04.1971
Place of birth	Modena (Italy)
Citizenship	Italian

Education

1985-1990	“Liceo Scientifico A. Tassoni” (Modena, Italy), “Diploma di maturitá scientifica” 1990
1990-2002	“Universitá degli studi di Modena e Reggio Emilia” (Italy), Faculty of Engineering, master degree in Material Engineering 2002
1999-2000	Civil service at cooperative “Porta Aperta” (Modena, Italy)
2001-2002	“Forschungszentrum Jülich (Germany), Institut für Schichten und Grenzflächen”, master thesis “MBE growth of AlGaN/GaN Heterostructures on Si(111)”
from 2003	Ph. D. student at the “IV. Physikalisches Institut, Georg-August-Universität Göttingen” (Germany)

Lebenslauf

Name	Marco Bertelli
Geburtstag	17.04.1971
Geburtsort	Modena (Italien)
Staatsangehörigkeit	Italienisch

Ausbildung

1985-1990	“Liceo Scientifico A. Tassoni” (Modena, Italien), “Diploma di maturitá scientifica” 1990
1990-2002	“Universitá degli studi di Modena e Reggio Emilia” (Italien), Fakultät für Ingegneurwissenschaften, Diplom in Material-Ingegneurwissenschaften 2002
1999-2000	Zivildienst bei der Genossenschaft “Porta Aperta” (Modena, Italien)
2001-2002	Forschungszentrum Jülich (Deutschland), Institut für Schichten und Grenzflächen, Diplomarbeit “MBE growth of AlGaN/GaN Heterostructures on Si(111)”
seit 2003	Doktorand am IV. Physikalischen Institut, Georg-August-Universität Göttingen (Deutschland)